# Stochastic Analysis and Control of EGR-Diluted Combustion in Spark Ignition Engines at Nominal and Misfire-Limited Conditions

by

Bryan P. Maldonado Puente

A dissertation submitted in partial fulfillment
of the requirements for the degree of
Doctor of Philosophy
(Mechanical Engineering)
in The University of Michigan
2019

Doctoral Committee:

Professor Anna Stefanopoulou, Chair
Professor Andre Boehman
Professor James Freudenberg
Professor Ilya Kolmanovsky

Bryan P. Maldonado Puente
bryanpm@umich.edu
ORCID iD: 0000-0003-3880-0065

*To my parents Telmo and Rocío, whose love and support are always present in my mind.*

*To my loving wife Emily, who is and has been my exemplary model.*

# ACKNOWLEDGEMENTS

I would like to start by expressing my gratitude towards my Ph.D. advisor, Professor Anna Stefanopoulou, for allowing me to embark on the Ph.D. program. Thanks for believing in me and guiding me through graduate school. Thanks for allowing me to find my own research and teaching philosophy and for the trust and confidence in my work.

Thanks to the committee members, Prof. Andre Boehman, Prof. James Freudenberg, and Prof. Ilya Kolmanovsky, for taking the time and interest in evaluating my work and for providing your comments, guidance, and feedback.

Thanks to the different funding sources that contributed at different stages to this work, including Toyota Motor North America, Rackham Graduate School through the Rackham Summer Award and multiple Travel Grants, the Advanced Research Projects Agency-Energy (ARPA-E) U.S. Department of Energy under Award Number DE-AR0000659, Argonne National Laboratory, and the Army Research Laboratory via the Journeyman Fellowship.

Thanks to all the members of the Powertrain Control Laboratory, from whom I learned something new every day. Thanks to the colleagues and technicians at the Walter E. Lay Automotive Engineering Laboratory who were always supportive and eager to know more about each other's work. Thanks to my friends in Ann Arbor and around the world who made my Ph.D. full of good times.

I would also like to thank my former Professors at the Universidad San Francisco de Quito, who showed me the path to becoming a scientist, *Dragones por siempre!* In particular, Dr. Eduardo Alba from the Department of Mathematics who believed in my potential since my participation in Math Olympiads in high-school. Thanks to his influence, I was able to have the best education and now I have fulfilled this step of my dream to become a researcher and a mathematician.

Thanks to my parents Telmo and Rocío, my sisters Sandra and Karina, my wife Emily, and all the rest of my immediate family to whom I owe more than I can give back. Thanks for the love and support, and for believing in my dreams.

# TABLE OF CONTENTS

# LIST OF FIGURES

**Figure**

# LIST OF TABLES

**Table**

# LIST OF ABBREVIATIONS

| | |
|---|---|
| **AKI** | Anti-Knock Index |
| **AFR** | Air-to-Fuel Ratio |
| **bTDC** | before Top Dead Center |
| **BDC** | Bottom Dead Center |
| **BSFC** | Brake Specific Fuel Consumption |
| **B2DS** | Beyond 2°C scenario |
| **CA** | Crank Angle |
| **CL** | Closed-Loop |
| **CPS** | in-Cylinder Pressure Sensor |
| **CKP** | CranKshaft Position |
| **CCV** | Cycle-to-Cycle Variability |
| **CV** | Combustion Variability |
| **DAQ** | Data Acquisition |
| **CoV** | Coefficient of Variation |
| **ECU** | Engine Control Unit |
| **EGR** | Exhaust Gas Recirculation |
| **EPA** | Environmental Protection Agency |
| **EV** | Electric Vehicle |
| **EKF** | Extended Kalman Filter |
| **FE** | Fuel Economy |
| **FIR** | Finite Impulse Response |
| **FPGA** | Field-Programmable Gate Array |
| **GHG** | GreenHouse Gas |
| **GTDI** | Gasoline Turbocharged Direct Injection |
| **GWN** | Gaussian White Noise |
| **HCCI** | Homogeneous-Charge Compression-Ignition |
| **HEV** | Hybrid Electric Vehicle |
| **HFCV** | Hydrogen Fuel cell Vehicle |
| **HP** | High Pressure |
| **ICE** | Internal Combustion Engine |
| **ICS** | Ionization Current Signal |
| **IIR** | Infinite Impulse Response |
| **IMEP** | Indicated Mean Effective Pressure |
| **IRA** | Input Redundancy Angle |
| **ISFC** | Indicated Specific Fuel Consumption |

| | |
|---|---|
| **LDV** | Light-Duty Vehicle |
| **LPP** | Location of Peak Pressure |
| **LQE** | Linear Quadratic Estimator |
| **LQG** | Linear Quadratic Gaussian |
| **LQR** | Linear Quadratic Regulator |
| **LTI** | Linear Time Invariant |
| **MBT** | Maximum Brake Torque |
| **MFB** | Mass Fraction Burned |
| **MIL** | Malfunction Indicator Light |
| **MLE** | Maximum Likelihood Estimator |
| **MPC** | Model Predictive Control |
| **MSRA** | Maximum Scaled input Redundancy Angle |
| **NMEP** | Net Mean Effective Pressure |
| **NMP** | Non-Minimum Phase |
| **$NO_x$** | mono-Nitrogen Oxides |
| **OBD** | On-Board Diagnostics |
| **OL** | Open-Loop |
| **PDF** | Probability Density Function |
| **PHEV** | Plug-in Hybrid Electric Vehicle |
| **PI** | Proportional-Integral |
| **PMEP** | Pumping Mean Effective Pressure |
| **PMF** | Probability Mass Function |
| **PSD** | Power Spectral Density |
| **P-V** | Pressure-Volume |
| **RG** | Reference Governor |
| **RGA** | Relative Gain Array |
| **RMSE** | Root Mean Square Error |
| **RPECS** | Rapid Prototyping Electronic Control System |
| **RTS** | Reference Technology Scenario |
| **RV** | Random Variable |
| **SA** | Spark Advance |
| **SE** | Standard Error |
| **SI** | Spark Ignition |
| **SISO** | Single-Input Single-Output |
| **STDv** | STandard Deviation |
| **SVD** | Singular Value Decomposition |
| **SwRI** | Southwest Research Institute |
| **TDC** | Top Dead Center |
| **TITO** | Two-Input Two-Output |
| **V2I** | Vehicle-to-Vehicle |
| **V2V** | Vehicle-to-Infrastructure |
| **2DS** | 2°C scenario |

# ABSTRACT

Worldwide regulations on greenhouse gas emissions demand a reduction in fuel consumption from the transportation sector. This reduction requires incremental improvements in engine and powertrain efficiency. Feedback combustion control under diluted conditions with exhaust gas recirculation (EGR) has the potential to improve the overall efficiency of spark-ignition engines by optimizing combustion efficiency, reducing heat transfer losses, and reducing pumping losses at medium loads. This control problem requires the coordinated action of the EGR valve and the spark advance. However, cycle-to-cycle variability in the combustion process limits the closed-loop system performance. Moreover, the input-to-output coupling between the actuators and measured combustion features need to be addressed in the control design to avoid undesired combustion events such as knock, partially burned cycles, and misfires. Therefore, the combustion control problem at high EGR-diluted conditions is a constrained multivariable stochastic control problem. This dissertation focuses on the control of the spark advance and the EGR valve in order to maximize the EGR benefits while maintaining stable combustion during steady state and load transients.

For a fixed engine speed/load condition, a two-input two-output discrete-time dynamic system was derived from system identification in order to use model-based control techniques. In particular, a linear quadratic Gaussian (LQG) controller was designed and experimentally tested for controlling spark and EGR valve. Such a controller was able to achieve an optimal combustion shape that maximizes EGR benefits and proved to be superior compared to traditional proportional-integral (PI) control strategies. An analytic solution for the amount of variability that the LQG controller contributes during closed-loop operation was derived, which can be used to modify the combustion targets to avoid misfire events. Given that sporadic misfires can occur when the control targets high levels of EGR, a stochastic controller based on the likelihood ratio test has been proposed to adjust the likelihood of misfires.

When the engine speed is fixed and the load demand is controlled by the driver, the feedback combustion controller needs to react to such disturbance and maintain

an optimal phasing. A physics-based model derived from manifold filling dynamics was coupled with a simple combustion model to formulate a three-input two-output dynamic system that considers not only the impact of the EGR valve and spark advance on the combustion, but also considers throttle tip-in and tip-out commands. The retuned LQG controller was experimentally tested and successfully maintained optimal phasing and maximized EGR levels during tip-in commands. However, during throttle tip-outs the system transitions through conditions where misfires occur. An explicit reference governor was designed to slow down the tip-out commands in order to avoid fast transitions that drive the system over the misfire limit. Given the inability to model misfires accurately, the reference governor was enhanced with model-free learning which enabled it to avoid misfires over time. Experimental results showed that successful misfire avoidance can be achieved in exchange for a slower tip-out response. It is suggested that such combustion control strategies can be paired with modern mild or full hybrid powertrain architectures to fully utilize the advantages of combustion control at high dilution levels.

# CHAPTER I

# Introduction

## 1.1 The Future Role of Internal Combustion Engines

Worldwide regulations on greenhouse gas (GHG) emissions demand a reduction in fuel consumption from the transportation sector. In 2019, the U.S. Environmental Protection Agency (EPA) published a report showing that 30% of the total of U.S. GHG emissions in 2017 corresponded to the transportation sector [1]. Moreover, as depicted in Figure 1.1, over half of this share is due to light-duty passenger cars. This shows the impact that high efficiency powertrains in light-duty vehicles can have for mitigating global warming.

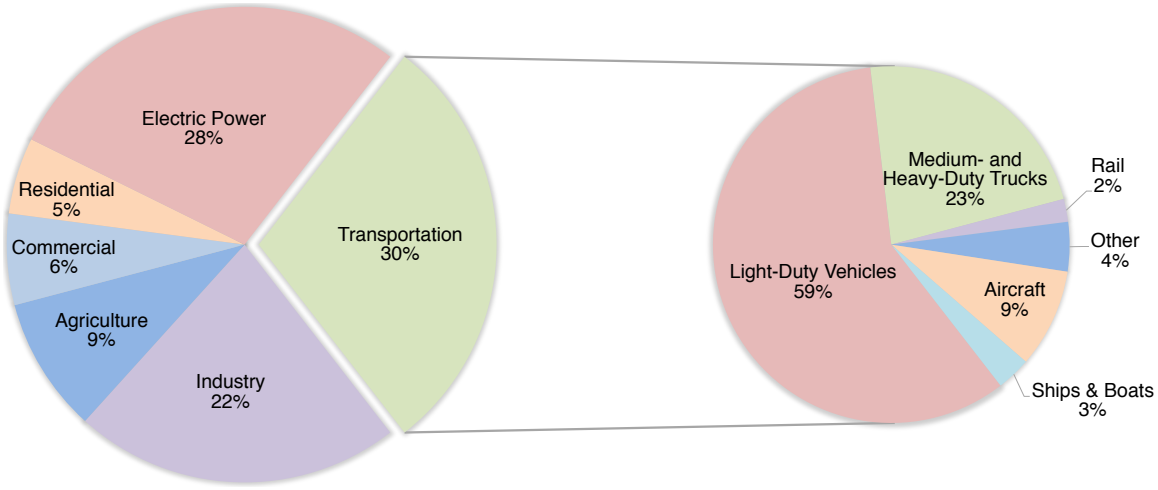


Figure 1.1: Share of U.S. transportation sector GHG emissions by source in 2017 (Adapted from *U.S.Transportation Sector Greenhouse Gas Emissions 1990-2017* [1])

In 2017 the International Energy Agency, which promotes sustainable energy policies for environmental protection in a global context, issued its annual report *Energy Technology Perspectives 2017, Catalysing Energy Technology Transformations* [2].

Such report provides information about technological trends and energy development paths to 2060 while presenting various scenarios for technology deployment. The objective of these scenarios is to show what types of measures and what level of commitment would be required to attain specific policy goals. The scenarios are described as follows:

- **Reference Technology Scenario (RTS):** It takes into account today's commitments by countries to limit emissions and improve energy efficiency, including the Paris Agreement. These efforts would result in an average temperature increase of 2.7°C by 2100.
- **2°C Scenario (2DS):** It lays out an energy system pathway and a $CO_2$ emissions trajectory consistent with at least a 50% chance of limiting the average global temperature increase to 2°C by 2100. Annual energy-related $CO_2$ emissions are reduced by 70% from today's levels by 2060, and carbon neutrality in the energy system must be reached before 2100.
- **Beyond 2°C Scenario (B2DS):** It explores how far deployment of technologies that are already available or in the innovation pipeline could take us beyond the 2DS. Technology improvements and deployment are pushed to their maximum practicable limits across the energy system in order to achieve net-zero emissions by 2060 and to stay net zero or below thereafter, without requiring unforeseen technology breakthroughs or limiting economic growth. This scenario is equivalent to a 50% chance of limiting average future temperature increases to 1.75°C by 2100.

Figure 1.2 shows the current and predicted vehicle technology penetration in the light-duty vehicle (LDV) sector for all three scenarios. The LDV market share has been divided into five categories: traditional internal combustion engine vehicles (ICEVs), hybrid electric vehicles (HEV), plug-in hybrid electric vehicles (PHEV), fully electric vehicles (EV), and hydrogen fuel cell vehicles (HFCV). Given that internal combustion engines are an integral part of the HEV and PHEV powertrains, the percentage of vehicles on the road with IC engines by 2060 are 92%, 73%, and 37% for the RTS, 2DS, and B2DS respectively. Therefore, a large part of the LDV decarbonization requires improvement in ICEs (gasoline and diesel), especially in the short- to medium-term. Such improvements also include hybridization technologies since HEVs are instrumental to enable the transition from traditional internal combustion engines to electric cars.

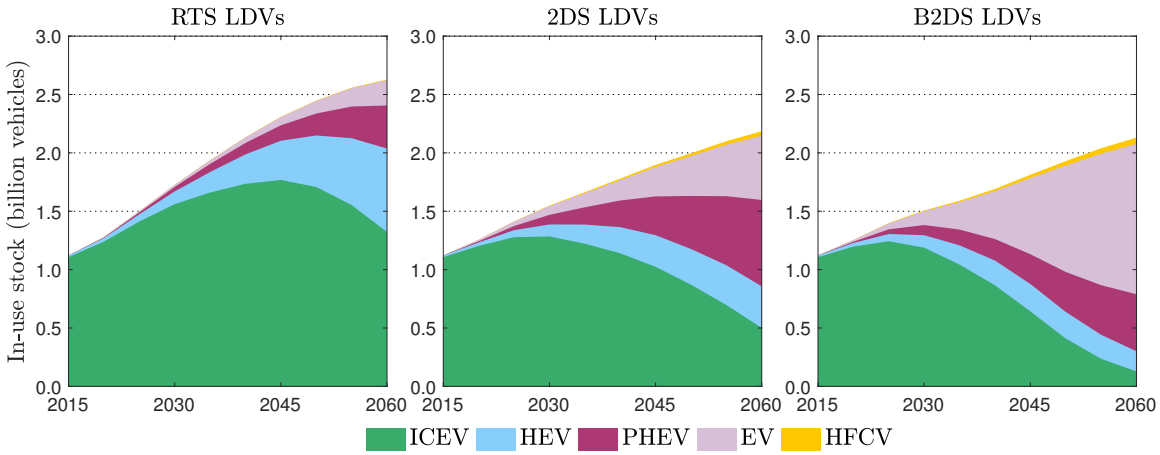


Figure 1.2: Technology penetrations in light-duty vehicle (LDV) market share, projection until 2060. (Data extracted from *Energy Technology Perspectives 2017* [2])

Fundamental research on engine design, combustion, and electrification has been continuously advancing towards higher fuel efficiencies. The following modern ICE powertrain technologies have shown to be better than the baseline ICE in power, efficiency, emissions, cost of ownership, reliability and utility:

- Downsizing and boosting
- Dilution with exhaust gas recirculation (EGR)
- Variable compression ratio
- Gasoline/Diesel cycle convergence
- Dual fuel or reactivity controlled combustion
- Hybridization
- Variable displacement

Out of all these new technologies, this dissertation explores the advantages of external cooled EGR and attempts to design control algorithms to maximize engine efficiency.

To sum things up, the reduction on greenhouse gas emissions requires incremental vehicle improvements (including engines), specially in the short- to medium-term. Improving the efficiency of the internal combustion engine, however, requires not only the use of optimized component design but also the use of control algorithms to maximize hardware benefits.

## 1.2 Background

### 1.2.1 Exhaust Gas Recirculation in Spark Ignition Engines

External cooled exhaust gas recirculation (EGR) has been widely used in modern spark-ignition (SI) internal combustion engine technologies due to its benefits associated with fuel economy and emissions [4]. Recirculation of the cooled exhaust gases offers thermodynamic benefits by 1) increasing the heat capacity ratio ($\gamma$) of the air-fuel mixture, and 2) lowering the peak cylinder temperature to effectively eliminate the likelihood of knock. By increasing the autoignition tolerance of the cylinder charge, spark advance (SA) can be adjusted for maximum brake torque (MBT). Additionally, recent research showed that when syngas (synthesis gas) supplementation ratio is increased, knocking is strongly suppressed, and the effect is more beneficial with EGR dilution [5]. Moreover, the lower in-cylinder temperature reduces the production of mono-nitrogen oxides ($NO_x$). In addition to the thermodynamical benefits, the use of external EGR requires a higher intake manifold pressure to maintain a certain load. Hence, at part-load, there is a reduction in pumping losses. Additionally, EGR allows for stoichiometric operation, making standard three-way catalysts effective for emissions control. Therefore, EGR-levels should be maximized and spark advance should be calibrated for MBT in order to increase engine efficiency and reduce fuel consumption. However, EGR affects the combustion kinetics, reducing the flame growth rate [6]. As a consequence, the sensitivity to perturbations during the flame development period increases, intensifying the cycle-to-cycle combustion variability (CV) and limiting the EGR-rate to a maximum for stable combustion [7, 8]. Furthermore, depending on the ignition timing of the charge, sporadic partially burned and/or misfire cycles can occur. In particular, MBT spark can be limited by misfires when ignition occurs too early in the compression stroke where pressure and temperature conditions cannot sustain the flame development. Such extreme events exacerbate the combustion variability and diminish the fuel efficiency benefits of EGR.

The evolution of the combustion process is typically inferred from pressure-volume (P-V) diagrams using in-cylinder pressure sensors (CPS) [9]. Figure 1.3 shows the P-V diagram of two operating conditions (Points A and B) with different EGR and spark timing calibrations. Note how pumping losses are reduced as the EGR valve opens and dilution increases. The P-V diagram corresponding to Point B has a late *combustion phasing* far from top dead center (TDC) consequence of the elongated combustion duration due to EGR. Point A, however, has a combustion phasing closer to TDC even though it operates at higher dilution levels. This results on a

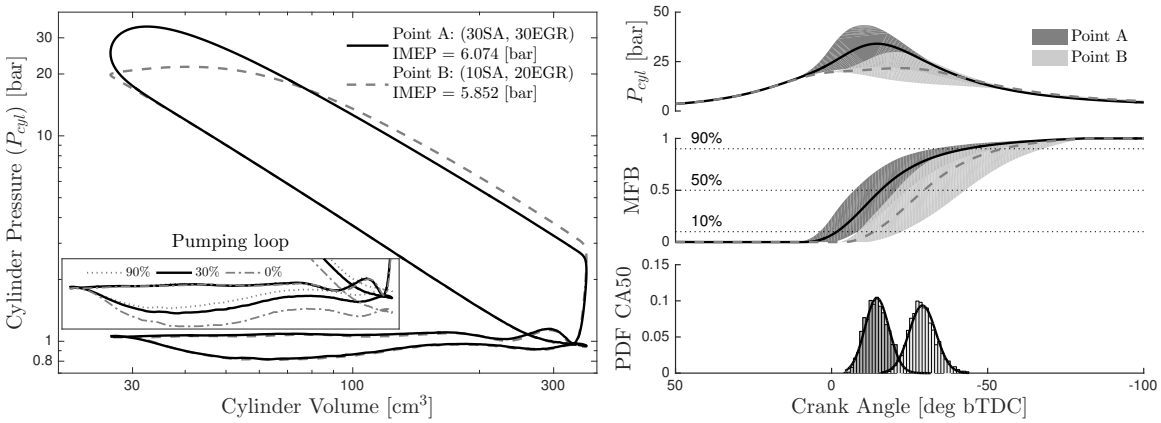


Figure 1.3: P-V diagrams for operating conditions A and B together with pumping loop with different EGR valve openings. Cylinder pressure ($P_{\text{cyl}}$), fuel mass fraction burned (MFB), and probability density function (PDF) of CA50 are plotted as function of CA deg. Grey colored region represents 2000 engine cycles.

higher indicated mean effective pressure (IMEP) for Point A, which corresponds to higher piston work. The difference here is the timing of ignition, which is more advanced for Point A, allowing time for a proper flame initiation (start of combustion) and development (duration of combustion). The control problem then simplifies to a spark control problem at a given level of dilution. Control of EGR valve and spark timing, however, cannot be based solely on mean-value models since it is important to keep combustion variability within certain levels.

### 1.2.2 Combustion Variability

The random fluctuation of the overall combustion process, manifested as variations of the in-cylinder pressure trace, is known as *combustion variability*. This uncertainty is often quantified by the coefficient of variation of the indicated mean effective pressure ($\text{CoV}_{\text{IMEP}}$). The combustion variability is tied to the cycle-to-cycle perturbations during the flame development [10]. Moreover, engine features such as intake manifold design, valve design, engine speed, compression ratio, and air-to-fuel ratio (AFR) can contribute to CV by affecting the mixture homogeneity, strength, and flow characteristics inside the cylinder. Table 1.1 describes the main sources of uncertainty during three distinguishable stages of flame evolution [7]. The combination of all these different uncertainties at every stage generates an uncorrelated stochastic combustion process. In other words, the CV does not depend on effects from any other previous cycle but only on the uncertainties during the intake, compression, and power stroke of each individual cycle [11].

Table 1.1: Factors affecting variability in flame development

| Flame Stage | Uncertainty source |
|---|---|
| Spark and flame initiation | • Mixture AFR and velocity near electrode<br>• Spark energy discharge |
| Initial flame development | • Charge AFR and homogeneity<br>• EGR dilution<br>• Turbulence intensity (flame kernel convection) |
| Turbulent flame propagation | • Total cylinder charge<br>• EGR dilution<br>• Turbulence intensity (flame front wrinkling) |

The *initial flame development* period is highly susceptible to factors causing CV and has a profound effect on the subsequent combustion [6, 12]. High EGR levels reduce the laminar flame burning velocity, increasing the combustion duration. If SA is not adjusted accordingly, such slow burn cycles will rapidly increase CV and potentially lead to misfires. The maximum amount of CV the engine can tolerate without affecting drivability or emissions is usually called the *engine stable operating limit* [13]. This constraint is closely related to the *misfire limit*, which can be determined either experimentally [13, 14] or estimated by a physics-based model of the early flame kernel development [15]. We seek to define *combustion features* that correlate well with changes in spark advance, EGR valve, and combustion variability for control.

The apparent heat release analysis is often used to calculate the fuel mass fraction burned (MFB) as a function of crank angle degrees (CA deg) [16]. Based on this calculation, the following combustion features are defined:

- **CA10:** CA degree at 10% MFB (start of combustion).
- **CA50:** CA degree at 50% MFB (combustion phasing).
- **CA1090:** CA duration between 10% and 90% MFB (duration of combustion).

The flame kernel develops at the spark plug and the fuel starts burning at the flame front towards the end of the flame initiation period (between SA and CA10) [17]. The combustion feature CA10 is then related with the *start of combustion* and is of great importance for misfire prevention. If spark timing, and consequently CA10, is too advanced then the pressure and temperature conditions might not be adequate for initiation or sustainment of the flame. On the other hand, if CA10 is too retarded, the downward piston motion increases the air/fuel mixture mean velocity

and turbulence and can halt or even extinguish the flame propagation, causing high cycle-to-cycle combustion variability [13, 15], [18, Chap. 9.4]. The flame propagation period is defined as the CA1090 duration. After a stable flame kernel is established, a turbulent flame consumes most of the fuel. In this rapid-burning period, the increase in cylinder pressure will contribute to the work done by the reciprocating engine. The combination of long *combustion duration* (CA1090) and late combustion initiation will cause the peak pressure to occur later on the expansion stroke, reducing the piston work produced, as demonstrated by Point B in Figure 1.3. Although the optimal CA50 has been correlated with MBT spark and peak pressure location [17], we aim to control the combustion initiation in order to prevent misfires and the combustion duration to prevent slow burning rates. Moreover, the combined control of CA10 and CA1090 will *shape* the MFB trace to the desired phasing.

## 1.3 Problems in Open-loop Combustion Control

The spark advance for MBT is typically determined after a spark sweep for every speed/load condition and coded as a lookup table. Although this procedure is simple, it can be time-consuming. At certain operating conditions the MBT timing could be knock limited and a feedback control algorithm must adjust SA to avoid it [19–22]. Moreover, different fuels, engine coolant temperatures, and ambient conditions have different requirements that increase the complexity of the spark map [23]. When cooled EGR is used, the spark calibration table needs compensation to achieve the desired combustion phasing. Additionally, over-advanced spark timing can cause slow burns and/or misfires. The boundary between healthy flames and misfires is difficult to define due to the cycle-to-cycle combustion variability. In order to comply with on-board diagnostics (OBD) regulations, the *misfire rate limit* must be kept under 2% [24]. However, drivability issues further constrain this limit to less than 0.5% [25], motivating the implementation of a stochastic misfire controller [14].

The EGR valve position controls the EGR-rate into the cylinder. Such flow rate depends on the pressure and temperature of the pulsating flow. This means that the EGR-rate can vary even when the valve remains unchanged. For open-loop control, the EGR valve is mapped from optimized values of cylinder flow and burned gas fraction in the intake manifold. Since the additional gases at the intake become a disturbance for the air-to-fuel ratio controller, an accurate estimation of the EGR-rate is needed to correct the fuel injection amount. Feedforward control based on the orifice flow equation is not robust under parameter variations such as ambient conditions,

intake temperature, and effective flow area [26]. Moreover, engine aging reduces its EGR tolerance [23]. Hence, accurate estimation of the EGR-rate is crucial to avoid the misfire and partial burn regions that can ruin any potential fuel economy gains. Although accurate estimation can be done despite the pulsating flow at different operating conditions, it requires an extra differential pressure sensor for the EGR loop [27, 28].

Altogether, the calibration process for the optimal spark advance and maximum EGR valve opening for minimum fuel consumption involves many engine hours and off-line data analysis. New methods have been developed to reduce the calibration time utilizing self-tuning algorithms for spark and EGR valve [29, 30]. However, targeting a heat release profile (invariant over many speed/load conditions) can reduce the burden in the calibration process dramatically [31]. More importantly, closed-loop feedback combustion control can be inherently robust to uncertainties in fuel properties, atmospheric conditions, system aging, and even engine-to-engine and cylinder-to-cylinder variations.

## 1.4 Closed-loop Combustion Control

Feedback combustion control has been previously developed to find the optimum spark timing by targeting specific combustion features. Powell in [32] summarizes the advantages and challenges of feedback combustion control based on CPS data. Eriksson in [33] introduces the ionization current signal (ICS) as means to replace the CPS and control spark timing based on the location of peak pressure (LPP). The research performed by Zhu includes not only the control of spark for MBT and knock but also considers the statistical properties of the cycle-to-cycle CV, either by using CPS or ICS data [34, 35]. Emiliano in [36] compares PI control strategies using different filtered CPS-based parameters for feedback, such as CA50 and LPP. However, the drawback of such a filtering method is that it slows down the system response. Most recently, Gao et al. in [37] developed a spark controller based on the stochastic properties of the LPP to minimize the overall increase of CV due to the feedback loop. However, these strategies are fundamentally single-input single-output (SISO), taking certain signal for feedback and calculating the spark adjustment required to meet the reference. Sellnau et al. in [38] were the first to achieve multivariable feedback combustion control at diluted conditions by designing a SISO controller for spark advance and a separate controller for EGR valve. Nonetheless, this strategy did not take into consideration the coupling between inputs and outputs of the system.

## 1.5 Dissertation Contributions and Organization

The overall contribution encompasses the design and testing of multivariable stochastic control strategies to achieve an optimal combustion shape, maximizing EGR levels, by adjusting the spark advance and the EGR valve simultaneously. The study of the controllability and feasibility properties of the system is performed at a fixed engine speed/load condition, as well as the study of the properties of the misfire limit. The last chapter, however, shows how the combustion control problem can be addressed during load transients. The specific contributions of this dissertation are:

1. **Combustion shaping controller:**

   At a fixed engine speed/load condition, a multivariable controller was designed to adjust the spark advance and the EGR valve in order to change the combustion shape based on some optimal values for maximum efficiency. The combustion shape is defined as the pair (CA50, CA1090), where CA50 is the combustion phasing (50% MFB) and CA1090 is the combustion duration (from 10% to 90% MFB). In order to perform model-based control design, a two-input two-output discrete-time system was derived from system identification. A linear quadratic Gaussian (LQG) controller was designed since it correctly addresses the feedback control limitations due to input-to-output coupling and cycle-to-cycle combustion variability. A comparison between the centralized LQG controller and a decentralized proportional-integral (PI) controller designed with similar characteristics is presented. Experimental data showed that the LQG controller has better performance and is less sensitive to cycle-to-cycle variability. This result coincides with the sensitivity analysis performed on the linear plant model, which gives an insight into why the LQG controller performs better than the PI controller. This topic is further discussed in Chapter II. The control design and preliminary simulation results were presented at the 2017 American Control Conference [39]:

   - B. P. Maldonado, H. Lian, J. B. Martz, A. G. Stefanopoulou, K. Zaseck, and E. Kitagawa. Combustion shaping using multivariable feedback control. In 2017 American Control Conference (ACC), pages 4760-4765, May 2017.

   The experimental results and the sensitivity analysis were published in the IEEE Transactions on Control Systems Technology [40]:

- B. P. Maldonado, K. Zaseck, E. Kitagawa, and A. G. Stefanopoulou. "Closed-loop control of combustion initiation and combustion duration". *IEEE Transactions on Control Systems Technology*, pages 1-15, 2019.

2. **Cycle-to-cycle combustion variability propagation through feedback:**

   The control-oriented combustion model derived from system identification was extended to a linear stochastic framework. Here, the cycle-to-cycle combustion variability was modeled as an additive Gaussian disturbance. Under such assumptions, the increase in the overall cycle-to-cycle variability can be analytically derived. Additionally, the stochastic properties of the control command signals under closed-loop can be inferred from the open-loop statistics. The experimental results indicated that the combustion model captures the mean, covariance, and cyclic correlation of inputs and outputs of the closed-loop system during steady state and transient operation. The details of this study are described in Chapter III. These results were presented at the 5th IFAC Conference on Engine and Powertrain Control, Simulation and Modeling (E-COSM 2018) [41]:

   - B. P. Maldonado and A. G. Stefanopoulou. "Linear Stochastic Modeling and Control of Diluted Combustion for SI Engines". *IFAC-PapersOnLine*, 51(31):99 - 104, 2018. 5th IFAC Conference on Engine and Powertrain Control, Simulation and Modeling E-COSM 2018.

3. **Analysis of plant directionality for the tracking control problem at the misfire limit:**

   This simulation study used previous data collected to mimic the results of an aggressive combustion control strategy. Here, the LQG controller was retuned to push EGR levels to the theoretical maximum, right before the misfire limit. The combustion shape target is chosen not only to avoid the misfire limit but also considers the closed-loop cycle-to-cycle variability. The linear plant model was used to analyze the fundamental limitations of the feedback combustion control problem at high levels of EGR dilution. Specifically, it was shown that the plant directionally at the target operating point requires large control signals that can 1) cause sporadic misfires, and 2) cause significant changes in brake torque. The results of this study are discussed in Chapter IV, which were presented at the 2018 American Control Conference [42]:

- B. P. Maldonado, J. S. Freudenberg, and A. G. Stefanopoulou, "Stochastic feedback combustion control at high dilution limit," in *2018 American Control Conference (ACC)*, June 2018, pp. 1598-1603.

4. **Likelihood-based control for misfire occurrence rate:**

   This study shows that misfire events can be accurately modeled by a sequence of independent and identically distributed Bernoulli random variables. Similar to knock events, a probabilistic model can be inferred based on the distribution of the total number of misfires and their interarrival times. Under this assumption, a likelihood-based controller was designed based on a desired misfire probability to retard spark timing to a condition less prone to misfire. The closed-loop system performance was evaluated by the probability distribution of the combustion phasing. The results were compared to a more conventional control strategy where spark retards every time a misfire is detected. A comparison of the steady state distribution of the combustion phasing shows that the likelihood-based controller has a more compact distribution closer to the misfire limit. The details of this study are presented in Chapter V and have been published in the Journal of Engineering for Gas Turbines and Power [14]:

   - B. P. Maldonado and A. G. Stefanopoulou, "Cycle-to-cycle feedback for combustion control of spark advance at the misfire limit," *Journal of Engineering for Gas Turbines and Power*, vol. 140, no. 10, pp. 102 812-102 812-8, 07 2018.

5. **Non-equiprobable partitions for statistical analysis of misfire events:**

   A novel methodology is presented for understanding the cycle-to-cycle combustion variability at the tipping point where high EGR levels suddenly trigger sporadic misfires. The indicated mean effective pressure (IMEP) was used as the cyclic parameter for categorizing combustion cycles into 1) high energy, 2) nominal, 3) partial burns, and 4) misfires. Deterministic patterns mainly involved misfires followed by high energy cycles due to the extra oxygen and fuel present at the intake stroke inside the cylinder immediately after a misfire. However, this study suggests that previous cycles do not have a major influence on the occurrence of misfires and partial burns, making them virtually random. A detailed study using conditional probabilities was conducted in order to reduce the number of combustion cycles needed to accurately estimate the misfire occurrence rate. The data showed that information about the occurrence of

partial burns can be used to modify the engine operating condition and thus reducing the probability of misfiring. This results were presented at the 2018 ASME Internal Combustion Engine Division Fall Technical Conference and can be found in Chapter VI [43]:

- B. P. Maldonado and A. G. Stefanopoulou, "Non-Equiprobable Statistical Analysis of Misfires and Partial Burns for Cycle-to-Cycle Control of Combustion Variability," ASME Internal Combustion Engine Division Fall Technical Conference, 2(51999):V002T05A003; 12 pages, 2018.

6. **Feedback combustion control during load transients:**

   When engine speed is fixed and the load demand changes due to throttle tip-in/tip-out commands, the combustion controller needs to keep combustion phasing at its optimum. In this case, throttle commands become a disturbance to the system, which again utilizes spark advance and EGR valve to maintain high levels of EGR with minimum fuel consumption. Additional modeling effort is required to include effects of throttle opening in the combustion process. Chapter VII reformulates the combustion control problem, describes the control-oriented model used for control design, designs an adaptive extended Kalman filter for estimating the changes in EGR rate inside the intake manifold, and designs a state feedback law based on a linear quadratic regulator (LQR). Such a control strategy was experimentally validated and the results show a close agreement with the modeling approach proposed. Although the controller can maintain and optimal phasing at high levels of EGR during throttle tip-in commands, throttle tip-outs drive the system momentarily over the misfire limit. In order to address this challenge, a learning reference governor strategy was proposed to slow down the system and avoid the transient states that causes misfires. The modeling and simulation results were presented at the 2019 Symposium for Combustion Control [44]:

   - B. P. Maldonado, N. Li, I. Kolmanovsky, and A. G. Stefanopoulou. "Satisfying Unstable Combustion Limits in SI Engines at EGR Diluted Conditions: A Learning Reference Governor Approach". In *2019 Symposium for Combustion Control (SCC)*, pages 8796. RWTH Aachen University, June 2019.

7. **Learning reference governor for misfire avoidance:**

The later part of Chapter VII shows the learning algorithm that can achieve misfire avoidance. This methodology was implemented in the experimental engine with successful results. After eight iterations of the learning algorithm, the reference governor was able to adjust the throttle tip-out command such that the problematic transient states are avoided. The experimental results concerning the closed-loop combustion controller and the learning reference governor have been tentatively accepted for a special issue on the topic of combustion control in the International Journal of Engine Research, and the full article will be submitted for publication in the same timeline as this dissertation:

- B. P. Maldonado, N. Li, I. Kolmanovsky, and A. G. Stefanopoulou. "Learning Reference Governor for Cycle-to-Cycle Combustion Control with Misfire Avoidance in SI Engines at High EGR-Diluted Conditions". *International Journal of Engine Research*, under review.

The following table summarized the main contributions by chapter:

Table 1.2: Dissertation contributions by chapter

| **Contributions** | **Ch. II** Combustion Control | **Ch. III** Gaussian LTI | **Ch. IV** Control at the Misfire Limit | **Ch. V** Misfire Control | **Ch. VI** Non-equiprobable Classification | **Ch. VII** Control for Load Transients |
|---|---|---|---|---|---|---|
| Experimental study | ✓ | ✓ | | ✓ | ✓ | ✓ |
| Simulation study | | | ✓ | ✓ | | ✓ |
| Combustion modeling | ✓ | ✓ | ✓ | | | ✓ |
| Misfire modeling | | | | ✓ | ✓ | |
| PI control design | ✓ | | | | | |
| LQG control design | ✓ | | ✓ | | | ✓ |
| Misfire control design | | | | ✓ | | |
| Deterministic analysis | ✓ | | ✓ | | ✓ | ✓ |
| Stochastic analysis | | ✓ | | ✓ | ✓ | ✓ |
| Sensitivity analysis | ✓ | | | | ✓ | |
| Fundamental limitations | | ✓ | ✓ | | | |
| Combustion cycle classification | | | | ✓ | ✓ | |
| Reference governor | | | | | | ✓ |

Finally, conclusions and outlook are presented in Chapter VIII.

# CHAPTER II

# Closed-loop Control of Combustion Initiation and Combustion Duration

## 2.1 Motivation

When high levels of cooled external exhaust gas recirculation (EGR) are used to increase engine efficiency, the laminar flame speed during the flame initiation period is reduced and the combustion duration is elongated. The reduction in flame propagation speed together with the increase in cycle-to-cycle variability makes the combustion process prone to failure of flame initiation (misfire) or slow burning rates. A highly visited operating speed/load point is used to investigate the feedback control of spark advance and EGR-valve. A decentralized Proportional-Integral (PI) controller and a centralized Linear Quadratic Gaussian (LQG) controller are designed to maintain a desired combustion initiation and duration that indirectly ensure a proper flame kernel initiation and flame propagation. A simple control-oriented combustion model is derived from system identification to perform simulation and linear analysis of the closed-loop system. Experimental validation of the controllers shows that the LQG performs better in transients and produces the least amount of cycle-to-cycle variability in closed-loop operation. Analysis of the linearized system in frequency domain shows that a multivariable architecture is required to handle the input-output coupling efficiently. Sensitivity analysis of PI and LQG controllers under gain variability is reported to guide the tuning process, which also influences the cycle-to-cycle variability. The two-input two-output (TITO) controllers designed in this study are compared with a single-input single-output (SISO) controller designed to only adjust spark advance for maximum brake torque. When the EGR-valve is adjusted based on a lookup table, uncertainty in the EGR-rate will affect directly the combustion duration for which the SISO controller alone cannot handle. In conclusion, a coordinated

spark and EGR controller based on the measured combustion features is deemed to be required for combustion control under diluted conditions.

## 2.2 Experimental Conditions

A production gasoline-fueled Toyota 1NR-FKE engine was used for this study. The four-cylinder, SI engine is port fuel injected, naturally aspirated, and uses cooled external EGR with a quick response valve. The EGR actuator is located upstream of the intake runners. This engine is equipped with variable valve timing, which is used to generate Atkinson combustion cycles with high compression for high thermal efficiency. The engine parameters are summarized in Table 2.1.

Table 2.1: Toyota 1NR-FKE engine parameters

| | |
|---|---|
| Compression Ratio: | 13.5 |
| Displacement [cc]: | 1329 |
| Stroke [mm]: | 80.5 |
| Bore [mm]: | 72.5 |
| Engine Speed [RPM]: | 1,600 |
| Engine Load [NM]: | 50 |
| Injection Strategy: | PFI |
| Global Equivalence Ratio: | 1 |
| Intake Charge Composition: | Air |
| Intake Air Volume Flow Rate [cc/s]: | 8 |
| Intake Charge Temperature [K]: | 370 |
| Number of Repetitive Cycles: | 2,000 |

Reference [45] provides more technical information about the hardware development. This production engine was equipped with production combustion pressure sensors (CAS-23A by Citizen Finedevice CO.,LTD.) for this work. In-cylinder pressure data was sampled every 2.5 [CA deg] and combustion features were calculated at the end of every cycle. A dynamometer regulated the engine speed and the throttle was manipulated to maintain a constant load. This work focuses in one speed/load condition, namely 1600 [RPM] and 50 [N-m], which is a frequently visited operating point in many regulated drive cycles world-wide. Tables 2.2, 2.3, and 2.4 show the mean and standard deviation (STDv) of the combustion features CA10, CA1090, and CA50 for 2000 engine cycles at various spark advance and EGR-valve combinations. Points that do not contain data correspond to regions where engine operation is problematic due to knock, misfires, or slow burns. To analyze and develop the feed-

Table 2.2: Statistics of CA10 [deg bTDC]: Mean and (STDv).

| EGR-valve | Spark Advance [deg bTDC] | | | | | | | | |
|---|---|---|---|---|---|---|---|---|---|
| opening | 5 | 10 | 15 | 20 | 25 | 30 | 35 | 40 | 45 |
| 10% | -13.1 (2.1) | -6.8 (1.8) | -1.5 (1.6) | | | | | | |
| 20% | -18.3 (2.6) | **-13.0 (2.4)** | -8.4 (2.3) | -4.3 (2.2) | -0.2 (2.0) | 3.3 (2.0) | | MISFIRE | |
| 30% | | | -10.2 (2.4) | -6.4 (2.3) | -3.7 (2.4) | **-0.4 (2.2)** | 2.2 (2.3) | | |
| 40% | PARTIAL BURN | | | | -5.8 (2.5) | -2.9 (2.4) | -1.2 (2.6) | 0.9 (2.9) | 2.5 (3.7) |

Table 2.3: Statistics of CA1090 [CA deg]: Mean and (STDv).

| EGR-valve | Spark Advance [deg bTDC] | | | | | | | | |
|---|---|---|---|---|---|---|---|---|---|
| opening | 5 | 10 | 15 | 20 | 25 | 30 | 35 | 40 | 45 |
| 10% | 24.7 (2.2) | 21.1 (1.7) | 18.8 (1.6) | | | | | | |
| 20% | 35.7 (4.3) | **32.2 (4.1)** | 29.4 (3.7) | 24.9 (3.3) | 24.5 (3.0) | 23.0 (2.6) | | MISFIRE | |
| 30% | | | 33.4 (4.5) | 31.1 (4.3) | 30.5 (4.2) | **28.2 (3.9)** | 27.1 (3.7) | | |
| 40% | PARTIAL BURN | | | | 33.7 (4.9) | 31.4 (4.4) | 30.7 (4.3) | 29.9 (4.3) | 29.5 (4.6) |

Table 2.4: Statistics of CA50 [deg bTDC]: Mean and (STDv).

| EGR-valve | Spark Advance [deg bTDC] | | | | | | | | |
|---|---|---|---|---|---|---|---|---|---|
| opening | 5 | 10 | 15 | 20 | 25 | 30 | 35 | 40 | 45 |
| 10% | -25.1 (1.9) | -17.5 (1.7) | -10.9 (1.7) | | | | | | |
| 20% | -35.9 (3.3) | **-28.8 (3.3)** | -23.0 (3.2) | -17.7 (3.2) | -12.4 (3.0) | -8.0 (2.7) | | MISFIRE | |
| 30% | | | -26.7 (3.7) | -22.0 (3.8) | -19.0 (3.9) | **-14.4 (3.6)** | -11.3 (3.8) | | |
| 40% | PARTIAL BURN | | | | -22.7 (4.3) | -18.6 (4.1) | -16.6 (4.5) | -14.2 (4.7) | -12.3 (5.2) |

back combustion controller, steps were performed between the conditions described in Tables 2.5 and 2.6.

These two points were chosen due to the similar standard deviation for the com-

Table 2.5: Operating conditions at POINT A

| | | |
|---|---|---|
| IMEP | = 6.07 [bar] | |
| SA | = 30 [deg bTDC] | |
| EGR valve | = 30 [% open] | |
| CA10 | = 0 [deg bTDC] | (STDv = 2.2) |
| CA50 | = -14 [deg bTDC] | (STDv = 3.6) |
| CA1090 | = 28 [CA deg] | (STDv = 3.9) |

Table 2.6: Operating conditions at POINT B

| | | |
|---|---|---|
| IMEP | = 5.85 [bar] | |
| SA | = 10 [deg bTDC] | |
| EGR valve | = 20 [% open] | |
| CA10 | = -13 [deg bTDC] | (STDv = 2.4) |
| CA50 | = -29 [deg bTDC] | (STDv = 3.3) |
| CA1090 | = 32 [CA deg] | (STDv = 4.1) |

bustion features. Note that POINT A has a higher IMEP than POINT B. Hence, this point will be used as the desired target for control. Note also that POINT A has more residuals, which translates to less pumping losses and less $NO_x$ emissions.

## 2.3 Control Design

### 2.3.1 System Identification

In order to develop a control-oriented combustion model, step changes in EGR-valve and spark advance were performed around the operating conditions shown in Tables 2.2-2.4. Figure 2.1 shows how the system behaves locally around POINT B. Given the sharp slope after the step command and the lack of significant overshoot, a first-order dynamical model is deemed appropriate for control analysis and design. The lag identified in response to the spark advance perturbation can be attributed to the change in heat flux through the cylinder walls. According to [46], spark advance strongly affects the cylinder surface heat flux during the combustion process, when both intake and exhaust valves are closed. More interestingly, the response to the step in EGR-valve (related to manifold filling dynamics) is quite fast due to the specialized finger-type cooled EGR system of the engine [45].

Additionally, note the coupling between increasing spark advance and advancing both CA10 and CA50. On the other hand, opening the EGR-valve increases the combustion duration due to its effect on combustion kinetics. Since the main purpose of the controller is to guarantee a correct flame initiation and development, the TITO

system will consist of spark advance and EGR-valve as inputs and CA10 (combustion start) and CA1090 (combustion duration) as outputs. The choice of CA10 over CA50 was made not only due to the desire to control the initial flame development period but also because the STDv of CA10 is lower than the STDv of CA50. Consider the following first order linear dynamical model:

$$\begin{bmatrix} \Delta\text{CA10} \\ \Delta\text{CA1090} \end{bmatrix} = \boldsymbol{K_{DC}} \begin{bmatrix} \dfrac{a_{\text{SA}}}{z-(1-a_{\text{SA}})}\Delta\text{SA} \\ \\ \dfrac{a_{\text{EGR}}}{z-(1-a_{\text{EGR}})}\Delta\text{EGR} \end{bmatrix} \tag{2.1}$$

where $\boldsymbol{K_{DC}}$ is the $2 \times 2$ DC gain matrix, $a_{\{\text{SA,EGR}\}}$ are the first order coefficients, and the frequency-domain variable $z$ has a sample rate $\Delta t = 0.075$ [s] (one engine cycle at

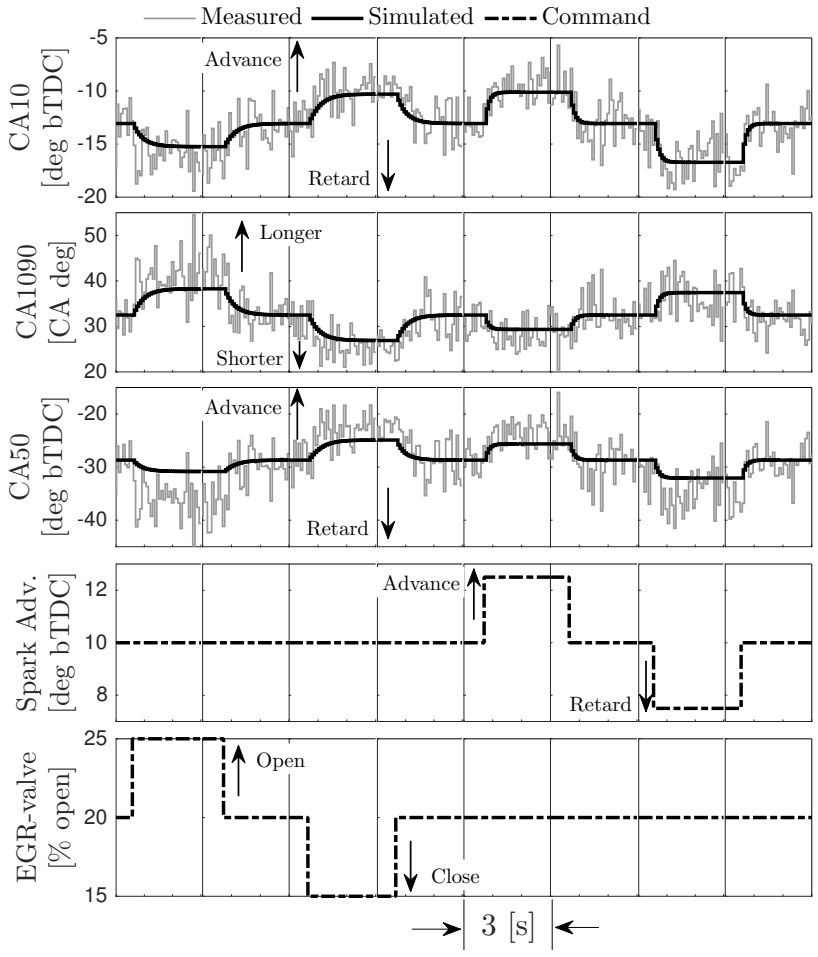


Figure 2.1: CA10, CA1090, and CA50 responses to step commands around the operating Point B: SA = 10 [deg bTDC] and EGR-valve = 20 [% open]. Each individual window is equivalent to a period of 3 [s].

Table 2.7: System Identification: DC gain matrix $\boldsymbol{K_{DC}}$

| EGR | Spark Advance [deg bTDC] | | | | | | |
|---|---|---|---|---|---|---|---|
| [%] | 5 | 10 | 15 | 20 | 25 | 30 | 35 |
| 10 | $\begin{bmatrix} 1.4 & -.6 \\ -.7 & 2. \end{bmatrix}$ $\kappa = 2.5$ | $\begin{bmatrix} 1.1 & -.8 \\ -.5 & 1. \end{bmatrix}$ $\kappa = 3.9$ | $\begin{bmatrix} .9 & -.6 \\ -.4 & .9 \end{bmatrix}$ $\kappa = 4.0$ | | | MISFIRE | |
| 20 | $\begin{bmatrix} 1.5 & -.6 \\ -1.9 & 1.6 \end{bmatrix}$ $\kappa = 6.7$ | $\begin{bmatrix} \mathbf{1.4} & \mathbf{-.6} \\ \mathbf{-1.6} & \mathbf{1.5} \end{bmatrix}$ $\kappa = \mathbf{6.4}$ | $\begin{bmatrix} 1.2 & -.8 \\ -1.1 & 1.6 \end{bmatrix}$ $\kappa = 5.5$ | $\begin{bmatrix} 1. & -.8 \\ -.8 & 1.4 \end{bmatrix}$ $\kappa = 5.5$ | $\begin{bmatrix} .8 & -.7 \\ -.5 & .9 \end{bmatrix}$ $\kappa = 5.1$ | $\begin{bmatrix} .6 & -.7 \\ -.3 & .8 \end{bmatrix}$ $\kappa = 5.0$ | |
| 30 | | | $\begin{bmatrix} 1.2 & -.4 \\ -1.7 & 1.2 \end{bmatrix}$ $\kappa = 9.1$ | $\begin{bmatrix} 1. & -.5 \\ -1.1 & .9 \end{bmatrix}$ $\kappa = 8.9$ | $\begin{bmatrix} .7 & -.5 \\ -.7 & 1. \end{bmatrix}$ $\kappa = 6.5$ | $\begin{bmatrix} \mathbf{.6} & \mathbf{-.5} \\ \mathbf{-.5} & \mathbf{1.} \end{bmatrix}$ $\kappa = \mathbf{5.5}$ | $\begin{bmatrix} .4 & -.6 \\ -.1 & .9 \end{bmatrix}$ $\kappa = 3.9$ |
| 40 | | PARTIAL BURN | | | $\begin{bmatrix} .9 & -.3 \\ -.9 & .6 \end{bmatrix}$ $\kappa = 9.0$ | $\begin{bmatrix} .5 & -.3 \\ -.4 & .6 \end{bmatrix}$ $\kappa = 5.1$ | $\begin{bmatrix} .5 & -.5 \\ -.3 & .6 \end{bmatrix}$ $\kappa = 6.2$ |

Table 2.8: System Identification: Time constants at 1600 [RPM]

| EGR | Spark Advance [deg bTDC] | | | | | | |
|---|---|---|---|---|---|---|---|
| [%] | 5 | 10 | 15 | 20 | 25 | 30 | 35 |
| 10 | $\tau_{\text{SA}} = .15$ $\tau_{\text{EGR}} = .39$ | $\tau_{\text{SA}} = .15$ $\tau_{\text{EGR}} = .29$ | $\tau_{\text{SA}} = .09$ $\tau_{\text{EGR}} = .39$ | | | MISFIRE | |
| 20 | $\tau_{\text{SA}} = .12$ $\tau_{\text{EGR}} = .33$ | $\boldsymbol{\tau}_{\text{SA}} = \mathbf{.15}$ $\boldsymbol{\tau}_{\text{EGR}} = \mathbf{.31}$ | $\tau_{\text{SA}} = .13$ $\tau_{\text{EGR}} = .35$ | $\tau_{\text{SA}} = .11$ $\tau_{\text{EGR}} = .38$ | $\tau_{\text{SA}} = .11$ $\tau_{\text{EGR}} = .29$ | $\tau_{\text{SA}} = .05$ $\tau_{\text{EGR}} = .21$ | |
| 30 | | | $\tau_{\text{SA}} = .13$ $\tau_{\text{EGR}} = .39$ | $\tau_{\text{SA}} = .12$ $\tau_{\text{EGR}} = .40$ | $\tau_{\text{SA}} = .12$ $\tau_{\text{EGR}} = .37$ | $\boldsymbol{\tau}_{\text{SA}} = \mathbf{.12}$ $\boldsymbol{\tau}_{\text{EGR}} = \mathbf{.44}$ | $\tau_{\text{SA}} = .11$ $\tau_{\text{EGR}} = .37$ |
| 40 | | PARTIAL BURN | | | $\tau_{\text{SA}} = .17$ $\tau_{\text{EGR}} = .35$ | $\tau_{\text{SA}} = .14$ $\tau_{\text{EGR}} = .41$ | $\tau_{\text{SA}} = .11$ $\tau_{\text{EGR}} = .42$ |

1600 [RPM]). Table 2.7 shows $\boldsymbol{K_{DC}}$ for each combination of spark advance and EGR-valve, as well as its condition number ($\kappa$). Note that the condition number increases as EGR levels increase, indicating a bad conditioning for matrix inversion. Feasibility of multivariable integral control requires the existence of the inverse of $\boldsymbol{K_{DC}}$ to allow the augmentation of integrator states [47, Chap. 3]. Therefore, moving to high EGR levels will be problematic for control design. Note however that advancing spark improves the feasibility of the tracking problem at high EGR levels. Using a zero-order hold conversion to obtain the equivalent continuous-time transfer functions, the

time constant can be calculated by the formula: $\tau = -\dfrac{\Delta t}{\ln(1-a)}$. The time constants for each input combination are shown in Table 2.8. To simplify the control-oriented model, a unique time constant was considered for all conditions, which equals to the average of the values in Table 2.8:

$$\tau_{\text{SA}} = 0.12[\text{s}] \approx 1.5[\text{cyc}], \quad \tau_{\text{EGR}} = 0.36[\text{s}] \approx 5[\text{cyc}]. \tag{2.2}$$

Note, however, that this dynamic model depends on engine speed and should be recalibrated for different speed/load conditions. Robust control or gain scheduling will be eventually needed for the entire engine map. The steady state values were replaced by a third order polynomial function of SA and EGR-valve that interpolates the mean values reported in Tables 2.2-2.4. The estimated values of the combustion features can be found in Figure 4.2. Figure 2.2 summarizes the combustion model used for control design.

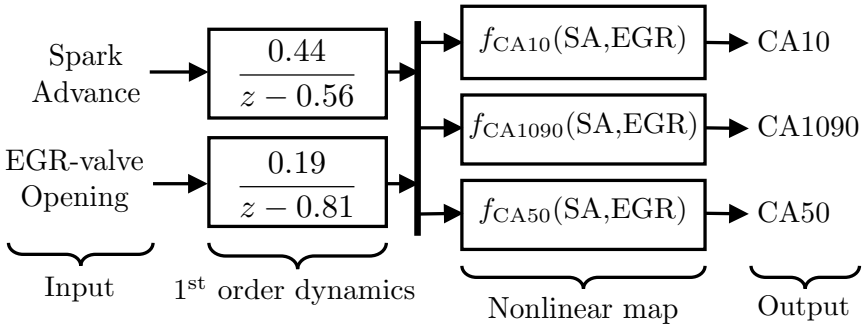


Figure 2.2: Control-oriented combustion model for simulation.

Given the strong coupling between spark advance and start of combustion, intuition suggests using a PI controller to track CA10 set points using the spark timing. Due to the time constant separation, it is also feasible to use the EGR command to reject the effect of spark advance on CA1090, and track CA1090 to its desired value using another PI controller. However, the second PI controller might not be able to completely reject the spark timing perturbations due to the input-output coupling of the system. The following sections will determine if 1) the decentralized architecture can be improved by a multivariable design and 2) if the multivariable controller will sustain its benefits despite the high cycle-to-cycle CV which acts as a disturbance to the performance outputs, namely CA10 and CA1090.

### 2.3.2 Input/Output Coupling Analysis

The DC gain matrix can point to the combinations of combustion start and duration (CA10 and CA1090) that will require high actuator action and hence are less feasible than others [48]. Table 2.9 summarizes the properties of $\boldsymbol{K_{DC}}$ for Points A and B. Note that neither of the two matrices are diagonally dominant, meaning that a *coupled* multivariable controller is necessary to coordinate the two actuators and fully utilize their joint effect on combustion shaping. Nonetheless, we still analyze the decoupled PI controller for comparison.

Table 2.9: DC gain matrix properties

| Point A | Point B |
|---|---|
| $\boldsymbol{K_{DC}} = \begin{bmatrix} 0.55 & -0.51 \\ -0.48 & 1.03 \end{bmatrix}$ | $\boldsymbol{K_{DC}} = \begin{bmatrix} 1.36 & -0.62 \\ -1.61 & 1.46 \end{bmatrix}$ |
| $\det = 0.32$ | $\det = 0.98$ |
| $\kappa = 5.56$ | $\kappa = 6.93$ |
| $\sigma_{\min} = 0.24$ | $\sigma_{\min} = 0.38$ |
| $\sigma_{\max} = 1.34$ | $\sigma_{\max} = 2.61$ |
| $\mathrm{RGA}_{(1,1)} = \mathrm{RGA}_{(2,2)} = 1.76$ | $\mathrm{RGA}_{(1,1)} = \mathrm{RGA}_{(2,2)} = 2.01$ |

$\det$ = determinant  $\sigma$ = singular value

In order to decide an input-to-output pairing for the decentralized control architecture, we will use the relative gain array (RGA) approach [49, 50]. The RGA for both matrices has positive diagonal entries, suggesting the pairing of CA10 with SA and CA1090 with EGR.

### 2.3.3 Proportional-Integral (PI) Controller

Consider the *decoupled* control architecture depicted in Figure 2.3. The closed-loop system uses one single-input single-output PI controller per actuator, paired

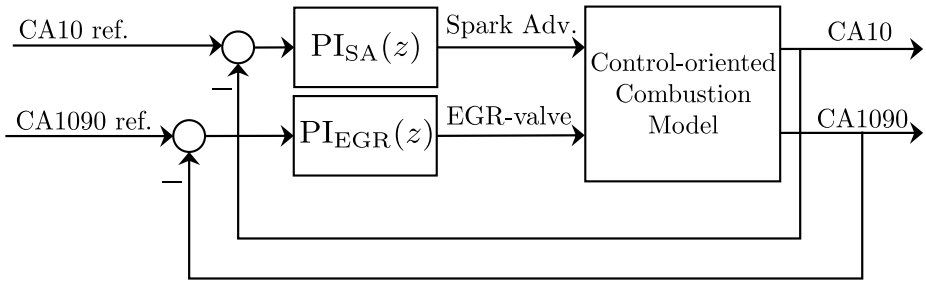


Figure 2.3: Block diagram of decoupled PI controller for feedback control.

to a specific performance output. The integral component guarantees a zero-mean steady state tracking error and filters the cycle-to-cycle CV from the measurements. The proportional component is mainly used to reduce the transient response time. The relative gain array (RGA) analysis performed in [39] suggested the pairing of spark advance with CA10 control and EGR-valve with CA1090 control. The PI gains were tuned using the sequential loop closing technique, closing the spark loop first since its action is faster than the EGR-valve (higher bandwidth) [51]. The spark loop is tuned targeting a fast response without overshoot in CA10 command, while the EGR-valve loop is tuned to reduce CA1090 overshoot without harming the spark loop performance. Table 2.10 shows the gain values selected according to the control-oriented combustion model.

Table 2.10: PI gain values

| **Controller** | Spark Advance | EGR-valve |
|---|---|---|
| $\mathrm{PI}(z) = P + \dfrac{I}{z-1}$ | $P_{\mathrm{SA}} = 0.50$<br>$I_{\mathrm{SA}} = 0.17$ | $P_{\mathrm{EGR}} = 0.10$<br>$I_{\mathrm{EGR}} = 0.20$ |

### 2.3.4 Linear Quadratic Gaussian (LQG) Controller

For multivariable feedback combustion control, let's define the inputs and outputs of the system at cycle $k$ as follows:

$$u_k = \begin{bmatrix} \mathrm{SA}_k \\ \mathrm{EGR}_k \end{bmatrix}, \quad y_k = \begin{bmatrix} \mathrm{CA10}_k \\ \mathrm{CA1090}_k \end{bmatrix}. \tag{2.3}$$

Hence, the control-oriented combustion model described by Eqn (2.1) can be represented in state space form by:

$$\begin{aligned} x_{k+1} &= Ax_k + B(u_k + w_k) \\ y_k &= Cx_k + v_k \end{aligned} \tag{2.4}$$

where $x_k$ is the state at cycle $k$, the random variables $w_k$, $v_k$ are Gaussian white noise with covariance kernels:

$$V = \mathrm{diag}\{V_{\mathrm{CA10}}, V_{\mathrm{CA1090}}\},\ W = \mathrm{diag}\{W_{\mathrm{CA10}}, W_{\mathrm{CA1090}}\}, \tag{2.5}$$

and the matrices $A, B$, and $C$ can be computed as follows:

$$A = \begin{bmatrix} 1 - a_{\mathrm{SA}} & 0 \\ 0 & 1 - a_{\mathrm{EGR}} \end{bmatrix}, \quad B = \begin{bmatrix} a_{\mathrm{SA}} & 0 \\ 0 & a_{\mathrm{EGR}} \end{bmatrix}, \text{ and}$$

$$C = \left[ \begin{array}{cc} \frac{\partial f_{\mathrm{CA10}}}{\partial \mathrm{SA}} & \frac{\partial f_{\mathrm{CA10}}}{\partial \mathrm{EGR}} \\ \frac{\partial f_{\mathrm{CA1090}}}{\partial \mathrm{SA}} & \frac{\partial f_{\mathrm{CA1090}}}{\partial \mathrm{EGR}} \end{array} \right] \Bigg|_{\textsc{Point B}} . \tag{2.6}$$

The linear time-invariant model for control design was based on the DC gain matrix at Point B. The covariance matrix $V$ can be estimated from the measured steady state values shown in Tables 2.2 and 2.3. Using the average standard deviation of all operating conditions, the estimated covariance is:

$$V_{\mathrm{CA10}} = 2.3^2\ [\mathrm{deg}^2], \qquad V_{\mathrm{CA1090}} = 4^2\ [\mathrm{deg}^2]. \tag{2.7}$$

Similar to the PI controller, consider the case of tracking a desired combustion shape $r = \begin{bmatrix} \mathrm{CA10}_{\mathrm{ref}} & \mathrm{CA1090}_{\mathrm{ref}} \end{bmatrix}^T$ using output feedback. Define the following integrator states:

$$z_{k+1} = z_k + (y_k - r). \tag{2.8}$$

Additionally, consider the case where the controller is designed to minimize the expected quadratic cost:

$$J = E\left[ \sum_{k=0}^{\infty} y_k^T Q y_k + z_k^T Q_{\int} z_k + u_k^T R u_k \right] \tag{2.9}$$

subject to the discrete-time dynamics described by Eqns. (2.4) and (2.8). The weighting matrices penalizing the system output, integrator states, and control effort are the following:

$$\begin{aligned} Q &= \mathrm{diag}\{Q_{\mathrm{CA10}},\ Q_{\mathrm{CA1090}}\} \\ Q_{\int} &= \mathrm{diag}\{Q_{\int \mathrm{CA10}},\ Q_{\int \mathrm{CA1090}}\} \\ R &= \mathrm{diag}\{R_{\mathrm{SA}},\ R_{\mathrm{EGR}}\}. \end{aligned} \tag{2.10}$$

A control law linear on the states is sufficient to minimize the cost function $J$. Hence, consider the following state feedback:

$$u_k = -K_x x_k - K_z z_k \tag{2.11}$$

Since the states are not available for feedback, the conditional distribution of $x_k$ given all the information up to cycle $k$, i.e. $\{y_0, \ldots, y_k, u_0, \ldots, u_{k-1}\}$, is required for feedback control. In the linear Gaussian case, the conditional distribution $p(x_k \mid y_0, \ldots, y_k, u_0, \ldots, u_{k-1})$ is given by the Kalman filter and is finite-dimensional [52, Chap. 6]. Consider the steady state Kalman filter for state estimation:

$$\widehat{x}_{k+1} = (A - LC)\widehat{x}_k + Bu_k + Ly_k \tag{2.12}$$

where $L$ is the estimator gain. For feedback control, replace the state in Eqn. (2.11) by the estimated state for Eqn. (2.12). The feedback gains $K_x, K_z$ are the solution of the infinite horizon *Linear Quadratic Regulator* (LQR) control problem and the estimator gain $L$ is the solution of the steady state *Linear Quadratic Estimator* (LQE).

The *coupled* controller depicted in Figure 2.4 uses a linear quadratic estimator to filter the variability in the measured combustion features (CA10 and CA1090) and estimate the control-oriented model states. The estimated states, together with the augmented integrator states, are used by the state feedback gain for step tracking. The random variable $w_k$ corresponds to the uncertainty of the combustion dynamics when spark advance and EGR-valve are adjusted. However, recall that such dynamics are due to manifold filling and heat transfer properties. Since these uncertainties cannot

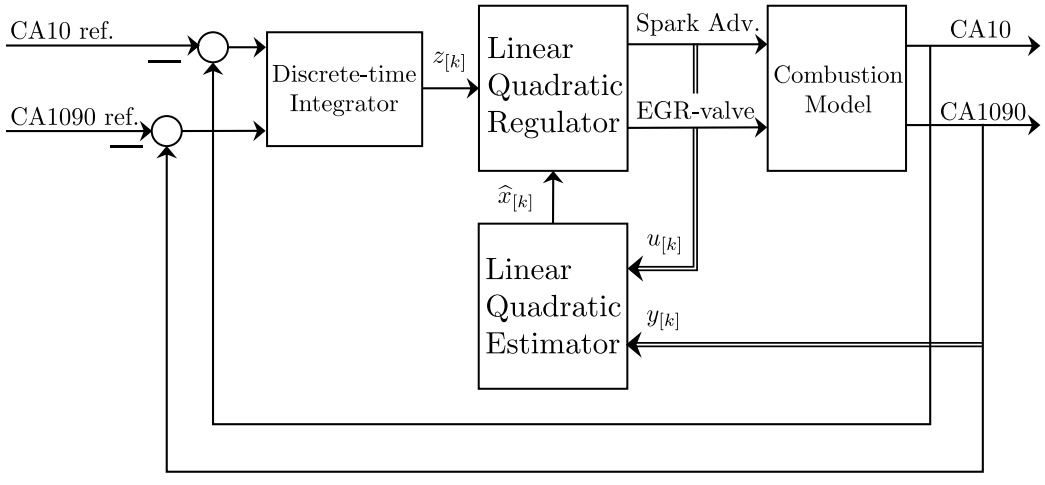


Figure 2.4: Block diagram of coupled LQG controller for feedback control.

be measured, we assume that the cycle-to-cycle variability of the combustion features is mainly due to the cycle-to-cycle perturbations of the turbulent environment inside the cylinder (modeled as output disturbance). Hence, the diagonal elements of the matrix $W$ were kept relatively low. The following values were chosen based on the variability reduction for engine estimated states in simulations:

$$W_{\mathrm{CA10}} = W_{\mathrm{CA1090}} = 0.1. \tag{2.13}$$

The measurements of the combustion features, however, are not filtered before the input to the integrator for tracking and performance purposes. Hence, the control gains product of the LQR algorithm should not be arbitrarily high since the cycle-to-cycle CV will be directly propagated through the integrator states and amplified by the feedback gain. Table 2.11 summarizes the costs used in the weighting matrices for the LQR algorithm. Tuning was performed manually, aiming for a fast rise-time and avoiding overshoot for both CA10 and CA1090. Additionally, simulations presented in [39] showed that such gains will not amplify dramatically the overall closed-loop cycle-to-cycle CV.

Table 2.11: Diagonal values for LQR weighting matrices

| **Cost** | System output: $Q$ | | Integrator state: $Q_\int$ | | Control: $R$ | |
|---|---|---|---|---|---|---|
| | $Q_{\mathrm{CA10}}$ | $Q_{\mathrm{CA1090}}$ | $Q_{\int \mathrm{CA10}}$ | $Q_{\int \mathrm{CA1090}}$ | $R_{\mathrm{SA}}$ | $R_{\mathrm{EGR}}$ |
| LQR | 5 | 5 | 0.6 | 0.4 | 5 | 5 |

## 2.4 Response Comparison

The closed-loop response of the system is analyzed in time domain based on rise-time, settling-time and overshoot performance. The closed-loop transfer function based on the control-oriented combustion model is analyzed in frequency domain via Bode magnitude plots. Additionally, statistics of the open-loop and closed-loop experimental data measured from the engine with each controller in place is also reported.

### 2.4.1 Time Domain

Steps from Point A to Point B and vice versa were performed using both (decentralized and centralized) controllers. Although control of the spark advance

is performed at each cylinder individually, the EGR-valve adjustment is calculated based on the CA10 and CA1090 measurements of cylinder number 1. Therefore, the experimental data presented in this section corresponds only to cylinder 1. In order to analyze the time domain performance of the closed-loop system, the measured data was filtered using a Savitzky-Golay finite impulse response smoothing filter [53]. Figure 2.5 presents the measured, filtered, and simulated responses of the combustion features of interest when a step command is performed. Tables 2.12 and 2.13 summarize the transient performance, cycle-to-cycle variability, and cylinder-to-cylinder difference of the target combustion features. A symbolic qualitative comparison is given for a quick assessment, based on a relative evaluation between controllers. Consider the following performance parameters to be evaluated:

**Rise-time:** Time between 0% to 90% of step magnitude.

**Settling-time:** Time until the signal reaches the error band ±5% of the target value.

**Overshoot:** Maximum peak exceeding the final value, with respect to the step direction. Percentage is given relative to step magnitude.

**STDv:** Standard deviation calculated at steady state for 60 cycles.

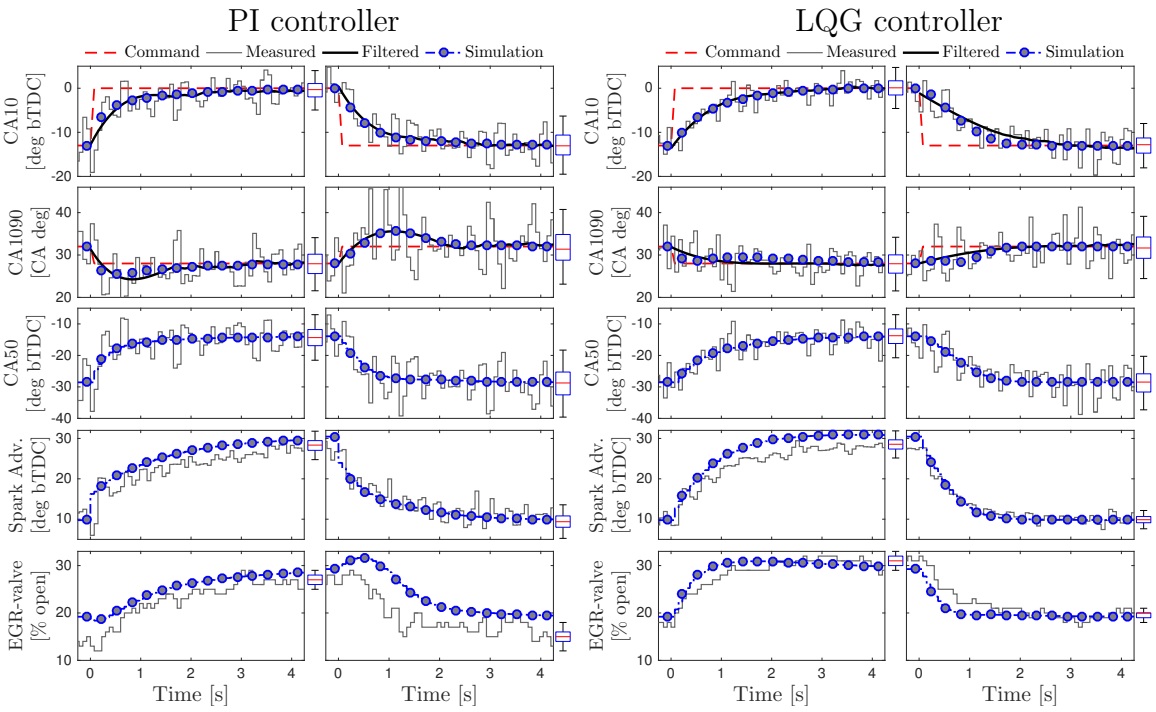


Figure 2.5: Experimental response of closed-loop system for command step Points B → A → B. Boxplot contains data within 1st and 3th quartiles, whiskers depict 2 STDv from mean. (Left: PI, Right: LQG)

**Root Mean Square Error (RMSE):** Used as a measure of the difference between the simulated values ($y$) and the filtered values ($\tilde{y}$), calculated as follows:

$$\text{RMSE} = \sqrt{\frac{\sum (y_i - \tilde{y}_i)^2}{n}} \tag{2.14}$$

**max$\Delta_{\text{cyl}}$:** Maximum cylinder-to-cylinder difference between mean values ($\bar{y}$) at steady state. In other words:

$$\max \Delta_{\text{cyl}} = \max |\bar{y}_{\text{cyl}(i)} - \bar{y}_{\text{cyl}(j)}|, \quad i, j \in \{1, 2, 3, 4\}. \tag{2.15}$$

Table 2.12: Performance comparison between PI and LQG for step: B → A

| **CA10** | Rise-time | | Settling-time | | Overshoot | | STDv | | RMSE | | max $\Delta_{\text{cyl}}$ | |
|---|---|---|---|---|---|---|---|---|---|---|---|---|
| PI | 2.2 [sec]<br>29 [cyc] | △ | 2.6 [sec]<br>34 [cyc] | ○ | 0.4<br>2.8% | ⊙ | 2.3 | ⊙ | 0.5 | ○ | 0.5 | ○ |
| LQG | 2.0 [sec]<br>26 [cyc] | △ | 2.6 [sec]<br>34 [cyc] | ○ | 0.2<br>1.5% | ⊙ | 2.2 | ⊙ | 0.4 | ⊙ | 0.5 | ○ |
| **CA1090** | Rise-time | | Settling-time | | Overshoot | | STDv | | RMSE | | max $\Delta_{\text{cyl}}$ | |
| PI | 0.2 [sec]<br>3 [cyc] | ⊙ | 3.1 [sec]<br>41 [cyc] | ○ | 3.7<br>94% | × | 3.4 | ○ | 0.6 | ○ | 2.3 | × |
| LQG | 1.1 [sec]<br>15 [cyc] | ○ | 1.1 [sec]<br>15 [cyc] | ⊙ | 0.4<br>9.2% | ○ | 3.0 | ⊙ | 0.6 | ○ | 1.7 | △ |

Table 2.13: Performance comparison between PI and LQG for step: A → B

| **CA10** | Rise-time | | Settling-time | | Overshoot | | STDv | | RMSE | | max $\Delta_{\text{cyl}}$ | |
|---|---|---|---|---|---|---|---|---|---|---|---|---|
| PI | 1.7 [sec]<br>22 [cyc] | △ | 2.6 [sec]<br>34 [cyc] | ○ | 0.6<br>4.8% | ⊙ | 3.2 | △ | 0.3 | ⊙ | 0.0 | ⊙ |
| LQG | 2.0 [sec]<br>27 [cyc] | △ | 2.4 [sec]<br>32 [cyc] | ○ | 0.6<br>4.8% | ⊙ | 2.5 | ⊙ | 0.8 | ○ | 0.2 | ⊙ |
| **CA1090** | Rise-time | | Settling-time | | Overshoot | | STDv | | RMSE | | max $\Delta_{\text{cyl}}$ | |
| PI | 0.3 [sec]<br>4 [cyc] | ⊙ | 2.9 [sec]<br>30 [cyc] | ○ | 3.6<br>89% | × | 4.5 | ○ | 0.4 | ⊙ | 1.4 | △ |
| LQG | 1.7 [sec]<br>23 [cyc] | △ | 1.7 [sec]<br>23 [cyc] | ⊙ | 0.6<br>15% | ○ | 3.9 | ⊙ | 0.4 | ⊙ | 0.8 | ○ |

⊙: Very good △: Medium sec: Seconds

○: Good ×: Bad cyc: Cycles @ 1600 [RPM]

Note how similar the CA10 responses are between the two controllers. This is a consequence of the control tuning, since the spark loop of the PI controller and the LQR algorithm aimed for a fast response without overshoot in CA10. In fact, rise-time and settling-time of CA10 for both cases are fairly similar. Nonetheless, the variability of CA10 in the LQG controller is less than the variability in the PI controller. On the other hand, CA1090 response differs significantly. This is related to the control architecture since the LQG controller utilizes a coordinated action of both actuators to minimize overshoot. The EGR loop in the decoupled PI controller does not have enough authority to compensate for overshoot since the tuning process prioritized the spark loop. Although the PI controller has the fastest rise-time for CA1090, it generates excessive overshoot and a longer settling-time. Once again, the LQG controller achieves the desired CA1090 response with the lowest variability. Note that the cycle-to-cycle variability in the commanded spark advance and EGR-valve is significantly reduced when using the LQG controller. This direct consequence of the LQE also contributes to the overall reduction of cycle-to-cycle CV. All the RMSE values are less than 1 [CA deg], indicating a good agreement between the filtered and the simulated responses. This shows that the first-order control-oriented model can be used to design a feedback combustion controller and predict the response of the closed-loop system. In addition to the lower cycle-to-cycle variability achieved with the LQG controller, the cylinder-to-cylinder variability is also significantly reduced when the LQG controller is in place. Finally, note that the only way for the PI controller to match the LQG cycle-to-cycle CV is to reduce the controller gains. By doing so, the rise-time and settling-time of both CA10 and CA1090 are increased, jeopardizing the performance of the controller. Therefore, the PI controller is not able to match the transient performance and the closed-loop variability of the LQG controller simultaneously.

### 2.4.2 Frequency Domain

The frequency response of the closed-loop transfer function $T(z)$ is reported here for completeness. Figure 2.6 shows the Bode magnitude plot of the components of $T(z)$, each of one represents the transfer function from a certain reference command (CAxx*) to a measured combustion feature (CAxx). Note that the bandwidth is similar for both controllers in the diagonal components. They also have an off-diagonal compensation in a similar band. However, the $T_{(2,1)}$ component for the LQG controller has a lower magnitude than its counterpart at all frequencies. This lower off-diagonal compensation avoids overshoot after the step change in the reference for CA1090.

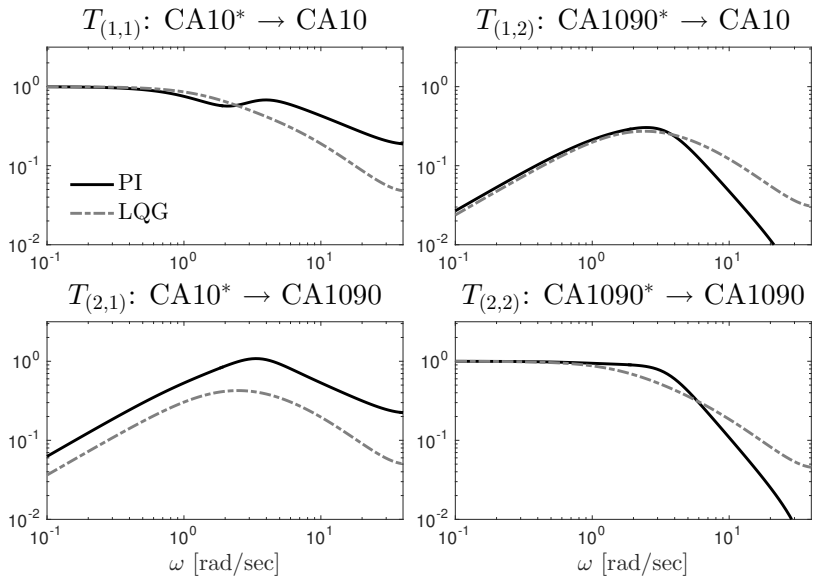


Figure 2.6: Bode magnitude plot for the components of $T(z)$. (* = command)

### 2.4.3 Steady State Distribution

Steady state data of the three combustion features of interest was recorded during 1600 engine cycles. The statistics for the open-loop and closed-loop PI and LQG controllers at Points A and B recorded during the same day, and hence same conditions, are stated in Table 2.14. Since the spark advance and EGR-valve were manually adjusted in open-loop, they are fixed values with zero STDv. Note that the LQG controller has a reduction in the variability of the combustion features compared with the PI controller. Therefore, the centralized LQG controller has a better performance regarding the management of cycle-to-cycle CV in closed-loop during steady state.

Figure 2.7 shows the probability density function (PDF) of each combustion fea-

Table 2.14: Statistics at steady state for open-loop (OL) and closed-loop system with PI and LQG controllers: Mean (STDv).

| | **Point** | SA [deg bTDC] | EGR-valve [% open] | CA10 [deg bTDC] | CA50 [deg bTDC] | CA1090 [CA deg] |
|---|---|---|---|---|---|---|
| OL | **A** | 30 (0) | 30 (0) | -0.4 (2.2) | -14.4 (3.5) | 28.2 (3.3) |
| | **B** | 10 (0) | 20 (0) | -13 (2.0) | -28.8 (3.7) | 32.2 (3.9) |
| PI | **A** | 28.3 (1.3) | 28.3 (1.4) | 0.0 (2.3) | -14.5 (3.7) | 28 (3.4) |
| | **B** | 9.71 (1.7) | 15.1 (1.3) | -13 (3.2) | -29.0 (5.2) | 32 (4.5) |
| LQG | **A** | 28.3 (1.2) | 30.8 (1.5) | 0.0 (2.2) | -14.0 (3.5) | 28 (3.0) |
| | **B** | 9.95 (1.1) | 19.6 (0.9) | -13 (2.5) | -28.9 (4.2) | 32 (3.9) |

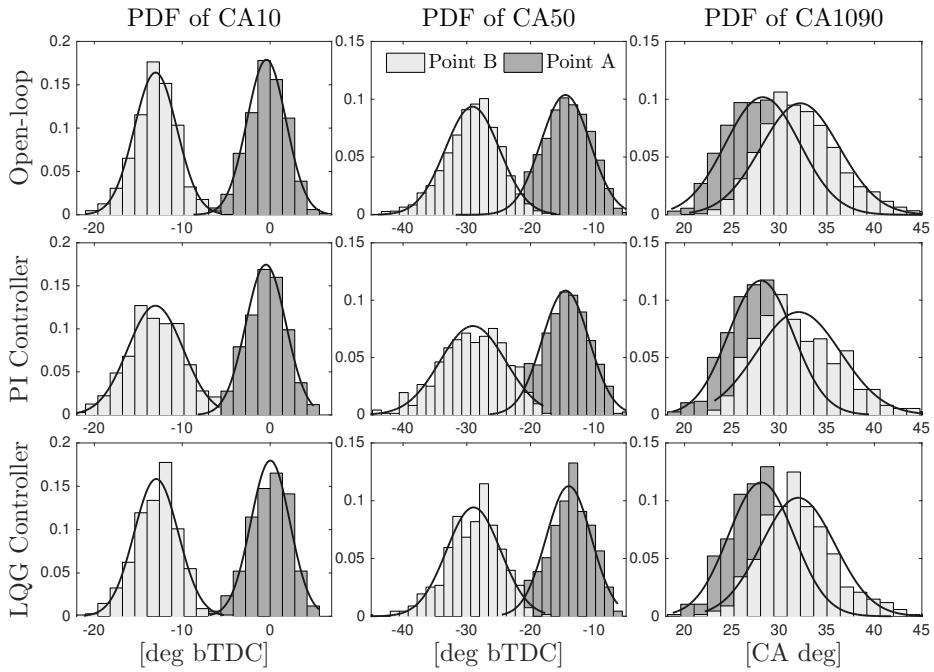


Figure 2.7: Probability density function (PDF) of combustion features at POINTS A and B, along with fitted theoretical normal distribution (solid line).

ture at open-loop and closed-loop operation. A theoretical normal distribution has been fitted using the statistics stated in Table 2.14. Note that all distributions in the open-loop and closed-loop system are fairly symmetrical and unimodal. Moreover, they seem to follow closely the theoretical Gaussian bell. Such plots confirm that the cycle-to-cycle CV in open-loop can be modeled by a Gaussian random process, with the difference that the measured values present slightly heavier or lighter tails. From now on, we will assume that the cycle-to-cycle CV can be modeled as a Gaussian random process.

Based on the previous discussion, the signals measured in open-loop at steady state conditions can be modeled as:

$$\mathrm{CAxx_{OL}}[k] = \mu_{\mathrm{OL}} + w_{\mathrm{OL}}[k], \quad w_{\mathrm{OL}}[k] \sim \mathcal{N}(0, \sigma^2_{\mathrm{OL}}) \tag{2.16}$$

where CAxx = {CA10, CA50, CA1090}, $\mu_{\mathrm{OL}}$ and $\sigma_{\mathrm{OL}}$ are the open-loop mean and standard deviation, and $w_{\mathrm{OL}}[k]$ is a Gaussian random variable. Analogously, the stochastic model for the measured combustion features during closed-loop control can be formulated as follows:

$$\mathrm{CAxx_{CL}}[k] = \mu_{\mathrm{CL}} + w_{\mathrm{CL}}[k], \quad w_{\mathrm{CL}}[k] \sim \mathcal{N}(0, \sigma^2_{\mathrm{CL}}) \tag{2.17}$$

where $\mu_{\text{CL}}$ is the target mean value and $w_{\text{CL}}[k]$ is a zero-mean Gaussian distributed random variable with variance $\sigma^2_{\text{CL}}$. The goal then is to determine which components in the feedback loop affect the variance of $w_{\text{CL}}[k]$, increasing the cycle-to-cycle CV. This model is exploited in the next section to better understand how STDv changes between open and closed-loop operation and how sensitive it is to feedback gains.

## 2.5 Sensitivity Analysis

### 2.5.1 Closed-loop System with Random Output Disturbance

Let $P(z)$ be the linearization of the control-oriented combustion model (plant) and $C(z)$ be the feedback controller (either PI or LQG). To better analyze the sensitivity of the system, the plant and controller signals need to be scaled by their nominal values. In doing so, control signals and output signals will correspond to percentage changes about nominal, making all signals comparable. Let $P_s(z)$ and $C_s(z)$ be the scaled plant and controller respectively. The *output sensitivity function* ($S_O(z)$) relates the plant output disturbances to the closed-loop system output, and is calculated as follows:

$$S_O(z) = (I_2 + P_s(z)C_s(z))^{-1}. \tag{2.18}$$

Given the normality assumption for the distribution of the combustion features in open-loop, the cycle-to-cycle CV can be modeled as an unbiased additive Gaussian process acting as a disturbance to the plant output. In closed-loop operation, each combustion feature will also behave as a random variable due to this random source. Figure 2.8 shows the block diagram of the model proposed for sensitivity analysis.

Neglecting measurement noise and input disturbance effects, the output of the

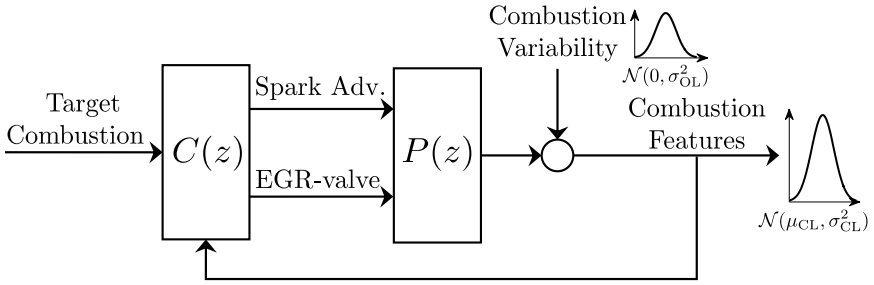


Figure 2.8: Block diagram of closed-loop feedback combustion control with additive Gaussian output disturbance.

closed-loop system can be calculated as:

$$\mathrm{CAxx}(z) = S_O(z)W_{\mathrm{OL}}(z) + T(z)R(z) \tag{2.19}$$

where $W_{\mathrm{OL}}(z)$ is the disturbance, $R(z)$ is the reference signal and $T(z)$ is the closed-loop transfer function. Given the uncertainties in the real plant parameters, the LQE previously designed is unable to completely filter the CV from the estimated states. Moreover, the integrator estate is not estimated (and hence not filtered) since it can be directly measured. As a consequence, the control command does not truly achieve a steady state value, as seen in Figure 2.5. Therefore, the feedback system is in a *perpetual transient state*, reacting to $w_{\mathrm{OL}}[k]$ at each engine cycle. However, the steady state distribution of the closed-loop system has a fixed mean ($\mu_{\mathrm{CL}}$) that matches the reference value. Under these observations, the response of the system after the step command can be further simplified to:

$$\begin{aligned} \cancel{\mu_{\mathrm{CL}}} + W_{\mathrm{CL}}(z) &= S_O(z)W_{\mathrm{OL}}(z) + \cancel{T(z)R(z)} \\ W_{\mathrm{CL}}(z) &= S_O(z)W_{\mathrm{OL}}(z). \end{aligned} \tag{2.20}$$

Given that $S_O(z)$ is a linear time-invariant (LTI) transfer function, and assuming that $w_{\mathrm{OL}}[k]$ is a zero mean stationary random process, it should hold that $w_{\mathrm{CL}}[k]$ is also a zero mean stationary random process. Moreover, $w_{\mathrm{CL}}[k]$ should maintain a normal distribution after the open-loop random variables pass through the LTI system [54, Chap. 4]. The previous Section showed that the outputs in closed-loop operation are indeed approximately Gaussian distributed with a fixed variance, supporting the original hypothesis that locally the system is well approximated by an LTI system.

To conclude the statistical analysis of the Gaussian random output disturbance, it suffices to look at the normalized autocorrelation function $R_{\mathrm{OL}}[l]$, defined as follows:

$$R_{\mathrm{OL}}[l] = \frac{E\left[w_{\mathrm{OL}}[k]w_{\mathrm{OL}}[k+l]\right]}{\sigma^2_{\mathrm{OL}}} \tag{2.21}$$

where $E[\cdot]$ is the expected value operator and $l$ is the signal lag. Figure 2.9 shows the sample autocorrelation functions for the measured combustion features at open-loop operation. The bounds shown in solid lines correspond to the 95% confidence limits assuming that $w_{\mathrm{OL}}[k]$ is uncorrelated $\forall k$. Note that almost all values of $R_{\mathrm{OL}}[l]$ when $l \neq 0$ fall within such bounds, suggesting that the process $w_{\mathrm{OL}}[k]$ is indeed uncorrelated. In other words, the variability of the combustion features does not depend on effects from any other previous cycle but only on the uncertainties during

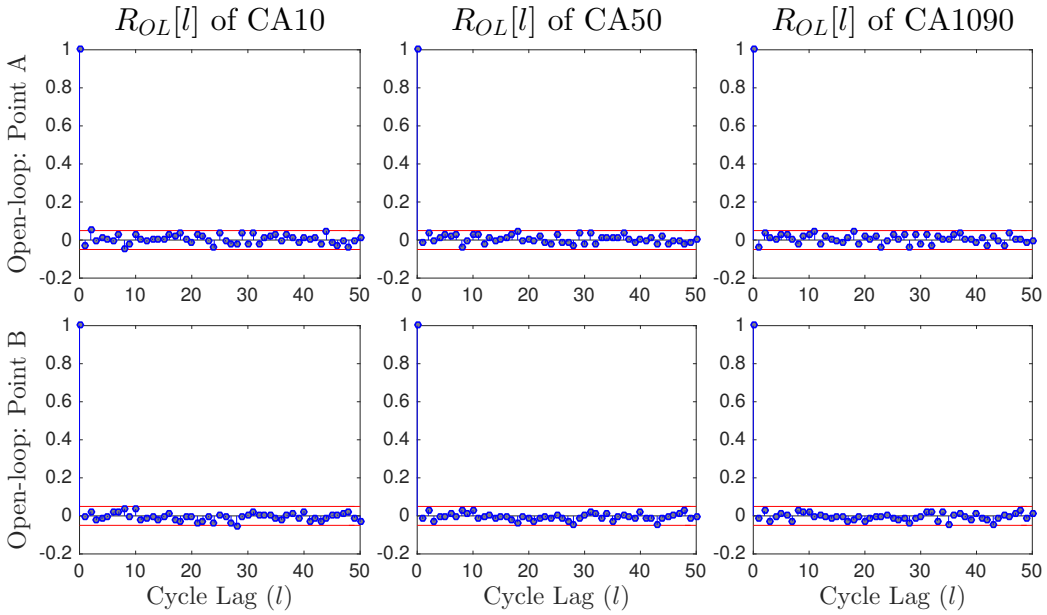


Figure 2.9: Normalized autocorrelation function at POINTS A and B for CA10, CA50, and CA1090 at steady state. Solid line represents the 95% confidence bounds for a Gaussian White Noise process.

the intake, compression, and power stroke of each individual cycle [11]. Under these observations, $R_{\mathrm{OL}}[l]$ can be modeled by a discrete-time impulse:

$$R_{\mathrm{OL}}[l] = \delta[l] = \begin{cases} 1 & \text{if } l = 0 \\ 0 & \text{if } l \neq 0 \end{cases} \tag{2.22}$$

which corresponds to a *Gaussian White Noise* process. The *power spectral density* (PSD) of a random process is defined as the Fourier transform of the autocorrelation function, hence, for the Gaussian White Noise process:

$$\mathcal{S}_{\mathrm{OL}}(\omega) = \mathcal{F}\left\{\sigma_{\mathrm{OL}}^2 R_{\mathrm{OL}}[l]\right\} = \sigma_{\mathrm{OL}}^2 \mathcal{F}\left\{\delta[l]\right\} = \sigma_{\mathrm{OL}}^2 \tag{2.23}$$

which means that the white noise has an equal distribution of energy over all frequencies of interest (equivalent to the open-loop variance). The transfer function $S_O(z)$ relates the PSD of $w_{\mathrm{OL}}[k]$ with the PSD of $w_{\mathrm{CL}}[k]$ in the following way:

$$\mathcal{S}_{\mathrm{CL}}(w) = \left|S_O(\omega)\right|^2 \mathcal{S}_{\mathrm{OL}}(\omega) = \left(\left|S_O(\omega)\right| \sigma_{\mathrm{OL}}\right)^2. \tag{2.24}$$

Consequently, the spectral power of the combustion features in closed-loop (signal variance) is directly related to the magnitude of the output sensitivity function $S_O(\omega)$.

Recall that for a multivariable system, each element of $S_O(\omega)$ is bounded by the largest singular value at any given frequency [47, Chap. 8]:

$$\left|S_{O(i,j)}(\omega)\right| \leqslant \sigma_{\max}(S_O(\omega)). \tag{2.25}$$

Therefore, knowledge of $\sigma_{\max}(S_O(\omega))$ at different frequencies determines how $\mathcal{S}_{\mathrm{CL}}(w)$ is affected by the closed loop configuration. Since the PSD is directly related to the variance of $w_{\mathrm{CL}}[k]$, frequencies where $\sigma_{\max}(S_O(\omega)) > 1$ will amplify the signal variability with respect to the open-loop case. Since any frequency can be potentially exited by $w_{\mathrm{OL}}[k]$, the peak of $\sigma_{\max}(S_O(\omega))$ is of special interest and should be kept as low as possible. This peak however is not only important for CV amplification, but also for stability and robustness. Moreover, it is recommended that $\sigma_{\max}(S_O(\omega)) < 2, \forall\omega$ [47, Chap. 8]. In order to provide guidance with the control tuning process, the output sensitivity function is analyzed when the feedback gains change with respect to the values stated in Tables 2.10 and 2.11. This analysis provides insight into how closed-loop cycle-to-cycle CV will change as we increase or decrease the aggressiveness of the controller.

### 2.5.2 Sensitivity of PI Controller

In order to determine which PI gain contributes to combustion variability amplification, the $S_O(z)$ function has been computed for different PI gains. Figure 2.10 shows how $\sigma_{\max}(S_O(\omega))$ changes when the PI controller gains change. In all four plots, the black line represents the designed controller, which gain values are stated in Table 2.10. Note that increasing the integral gain of either independent PI controller increases the peak of $\sigma_{\max}(S_O(\omega))$ at high frequencies, especially when increasing the $I_{\mathrm{EGR}}$ gain. This result suggests that the variability of the closed-loop system will increase. Note, however, that the $\sigma_{\max}(S_O(\omega))$ remains practically invariant under proportional gain sweep. So the cycle-to-cycle variability should not be significantly amplified when $P_{\mathrm{SA}}$ or $P_{\mathrm{EGR}}$ increase. A closer look at the components of $S_O(w)$ in Figure 2.10 shows how the CV measured in one input is amplified and directed to which output. For a high integral gain in the spark advance controller ($I_{\mathrm{SA}} = 0.7$), the component with the highest amplification is $S_O(1,1)$. This means that CV from the CA10 measurement directly affects the CA10 response of the system but does not interact significantly with the CA1090 response. For the case with a high integral gain in the EGR-valve controller ($I_{\mathrm{EGR}} = 0.7$), Figure 2.10 indicates that the components $S_O(1,2)$ and $S_O(2,2)$ generate the highest amplification. This suggests

that the variability in the measurements of CA1090 will affect CA10 and CA1090 responses simultaneously. It is advised that integral gains remain low to avoid negative consequences in the combustion process during closed-loop control.

The system with the PI controller in place was subject to gain variations and the measured steady state standard deviation was calculated at the targeted POINT A. Table 2.15 shows the STDv values for the combustion features in experiments performed. Note that the values for gains $P$ and $I$ do not exceed 0.7 in both PI controllers because the cycle-to-cycle CV of the closed-loop system became excessively large. When changing the gains of the PI controller for spark advance, note that increasing the integral gain increases the STDv of CA10 and CA1090. However, the average change in STDv from $I = 0.2$ to $I = 0.7$ is $\Delta$STDv $= 0.7$ for CA10, while $\Delta$STDv $= 0.3$ for CA1090. This means that the effect on the CA10 response is higher than the effect on CA1090 response, matching the behavior predicted by the analysis of $S_O$. Changing the proportional gain, on the other hand, increases the variability on both outputs, for which the linear model is unable to predict. Increasing

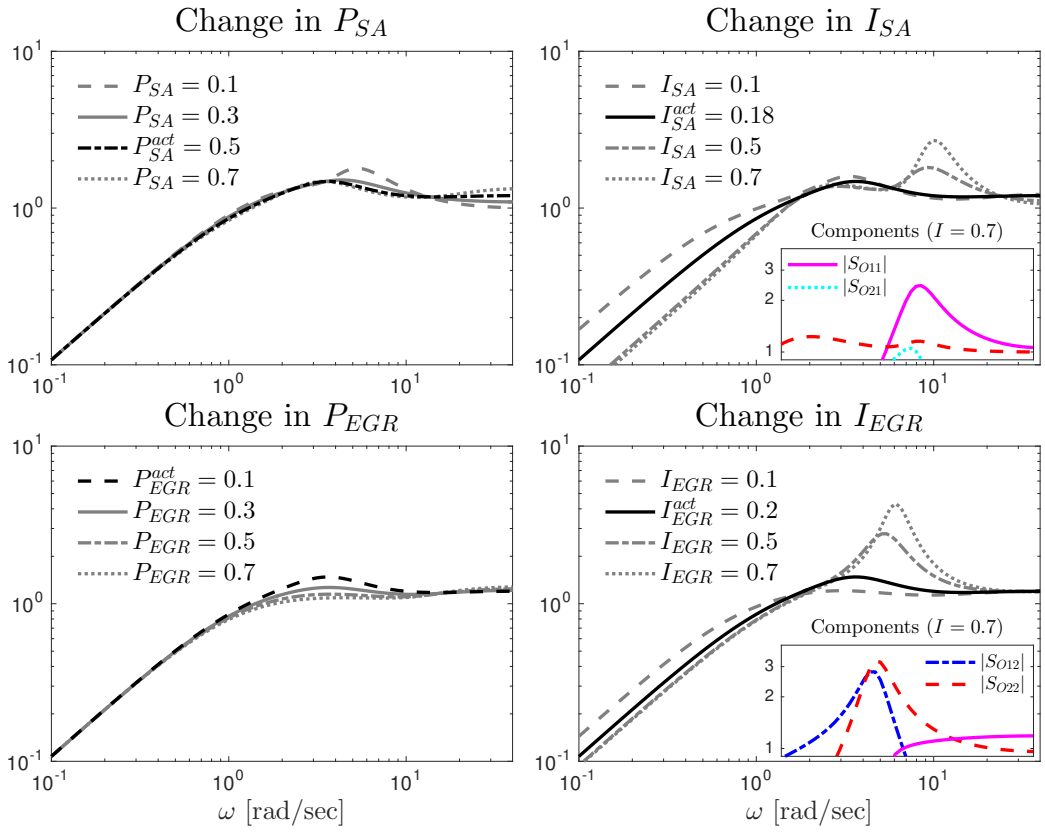


Figure 2.10: Maximum singular values ($\sigma_{\max}(S_O(\omega))$) at various PI controller gains together with selected components of $S_O$ at high integral gain.

the integral gain in the EGR-valve loop increases the variability of each feature in a similar manner, although increasing the proportional gain does not change the variability of the combustion features. The average increase in STDv for the CA10 response from $I = 0.2$ to $I = 0.7$ is $\Delta\text{STDv} = 0.4$, while $\Delta\text{STDv} = 0.6$ for CA1090. Both trends qualitatively agree with the behavior expected from the linear analysis of the system, confirming that the control-oriented combustion model is a simple, yet powerful tool to analyze the closed-loop properties of the system.

### 2.5.3 Sensitivity of LQG Controller

Recall that the LQG controller consists of a state estimator (LQE) and a state feedback gain (LQR). Considering that the LQE design depends on the statistical properties of the open-loop measured signals, the observer gains will remain unchanged in the sensitivity analysis. The state feedback gains, on the other hand, will change according to four different sets of cost values in the LQR algorithm. Each of the following sets contains the numerical values corresponding to the diagonal entries of the matrices penalizing the system output, integrator states, and control effort, as

Table 2.15: STDv at steady state using different PI gains at Point A

| | **SA controller** | | | **EGR-valve controller** | | |
|---|---|---|---|---|---|---|
| **CA10:** | $I = 0.2$ | $I = 0.5$ | $I = 0.7$ | $I = 0.2$ | $I = 0.5$ | $I = 0.7$ |
| $P = 0.3$ | 2.4 | 2.6 | 2.9 | 2.4 | 2.5 | 2.8 |
| $P = 0.5$ | 2.5 | 2.8 | 3.2 | 2.3 | 2.6 | 2.8 |
| $P = 0.7$ | 2.7 | 3.2 | 3.6 | 2.4 | 2.5 | 2.7 |
| **CA50:** | $I = 0.2$ | $I = 0.5$ | $I = 0.7$ | $I = 0.2$ | $I = 0.5$ | $I = 0.7$ |
| $P = 0.3$ | 3.8 | 4.0 | 4.4 | 4.1 | 4.4 | 4.7 |
| $P = 0.5$ | 4.0 | 4.4 | 4.8 | 3.9 | 4.4 | 4.8 |
| $P = 0.7$ | 4.2 | 4.7 | 5.3 | 4.0 | 4.3 | 4.7 |
| **CA1090:** | $I = 0.2$ | $I = 0.5$ | $I = 0.7$ | $I = 0.2$ | $I = 0.5$ | $I = 0.7$ |
| $P = 0.3$ | 3.4 | 3.6 | 3.7 | 3.9 | 4.2 | 4.5 |
| $P = 0.5$ | 3.6 | 3.7 | 3.8 | 3.8 | 4.1 | 4.6 |
| $P = 0.7$ | 3.6 | 3.9 | 4.1 | 3.8 | 4.1 | 4.5 |

previously described in Table 2.11:

$$
\begin{array}{rlccccccc}
 & & Q_{\mathrm{CA10}} & Q_{\mathrm{CA1090}} & Q_{\int \mathrm{CA10}} & Q_{\int \mathrm{CA1090}} & R_{\mathrm{SA}} & R_{\mathrm{EGR}} & \\
C_1 = & \{ & 10, & 5, & 0.6, & 0.4, & 3, & 5\}, & \\
C_2 = & \{ & 5, & 5, & 0.6, & 0.4, & 5, & 5\}, & (2.26) \\
C_3 = & \{ & 5, & 5, & 0.5, & 0.1, & 5, & 5\}, & \\
C_4 = & \{ & 10, & 10, & 0.5, & 0.5, & 5, & 5\}. &
\end{array}
$$

Note that all the combinations penalize heavily the system outputs in order to avoid overshoot and achieve the faster rise-time. The penalty on integrator states is smaller since high integral gain generated an excessive amount of cycle-to-cycle CV, similar to the previous case with the PI controller. The penalty on the actuators is kept almost constant at a high value to minimize the actuator variability. Note also that the set $C_1$ corresponds to the selected weights for the LQR algorithm previously discussed. The left plot of Figure 2.11 shows the transient response of CA1090 for all four calibrations. This shows that the sets of weights $C_2$, $C_3$, and $C_4$ do not generate overshoot on CA1090.

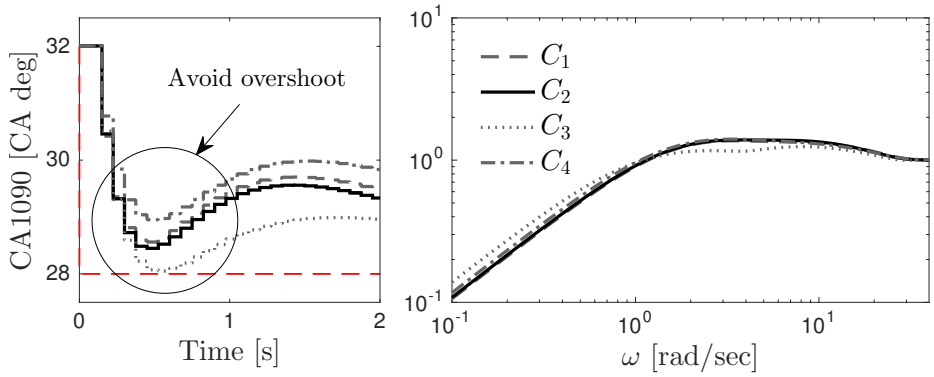


Figure 2.11: Left: CA1090 response with LQG controller under different set of state feedback gains. Right: Maximum singular values $\sigma_{\max}(S_O(\omega))$

The right plot of Figure 2.11 shows the maximum singular value $\sigma_{\max}(S_O(\omega))$ for different frequencies using the four different sets of tuning parameters in the LQR algorithm. All sensitivities are similar in magnitude, meaning that the LQG controller is robust under perturbations in state feedback gains. This implies that, for this specific step command, the choice of feedback gains mainly depends on the desired transient performance rather than the amplification of cycle-to-cycle CV. Each state feedback gain resulting from the different cost sets was tested under closed-loop operation at the target condition (Point A). Table 2.16 shows the STDv values

of each combustion feature. Note that the cycle-to-cycle CV remains practically unchanged under gain adjustment, which agrees with the linear analysis of the closed-loop system.

Table 2.16: STDv at steady state using different feedback gains at POINT A

| | **Set** $C_1$ | **Set** $C_2$ | **Set** $C_3$ | **Set** $C_4$ |
|---|---|---|---|---|
| **CA10** | 2.4 | 2.4 | 2.4 | 2.4 |
| **CA50** | 3.8 | 3.9 | 3.9 | 3.9 |
| **CA1090** | 3.6 | 3.7 | 3.7 | 3.8 |

### 2.5.4 Uncertainty in EGR-rate

The feedback combustion controller relies on in-cylinder pressure measurements to calculate combustion features and adjusts the EGR-valve that generates the desired EGR-rate to match the target combustion features. Suppose that the target for control is MBT timing to maximize torque, rather than start and duration of combustion for proper flame development. Similar to the work done by [19, 33–37, 55, 56], a SISO PI controller can be designed to adjust spark advance in response to a CA50 desired target. In general, the optimal torque, hence most fuel efficient, combustion phasing in SI engines is between $-7$ and $-10$ [deg bTDC] [18, Chap. 9], [57]. Therefore, POINT A will be the control target since its CA50 value is closer to the aforementioned range. For the SISO controller, EGR-valve must be controlled in an open-loop fashion and calibration of the valve must be performed under several speed/load/spark/EGR-rate conditions. Using the same first order combustion model shown in Figure 2.2, the PI controller for CA50 can be designed to cancel the stable pole and track the desired CA50 target without overshooting any combustion feature, such as CA1090. The following discrete-time controller achieved the transient constraints minimizing settling-time:

$$\mathrm{PI}_{\mathrm{CA50}} = 0.75\frac{z - 0.56}{z - 1}. \tag{2.27}$$

Figure 2.12 shows the simulated transient response of the PI, LQG, and the new SISO $\mathrm{PI}_{\mathrm{CA50}}$, which relies on CA50 measurements solely. When the opening of the EGR-valve is overestimated, due to the inaccuracy of the EGR-rate estimation, for example, the spark is forced to advance even further to compensate for excess in dilution. The $\mathrm{PI}_{\mathrm{CA50}}$ controller cannot achieve the desired combustion duration due to the lack of control authority over this feature and can potentially lead to undesir-

able conditions, such as misfires or slow burns. This result stresses the importance of TITO feedback control for robustness under EGR drifts and for a reduction in calibration burden, given that the PI and LQG controllers do not depend on EGR-rate estimation for EGR-valve actuation. Note however that the CA10 value is not

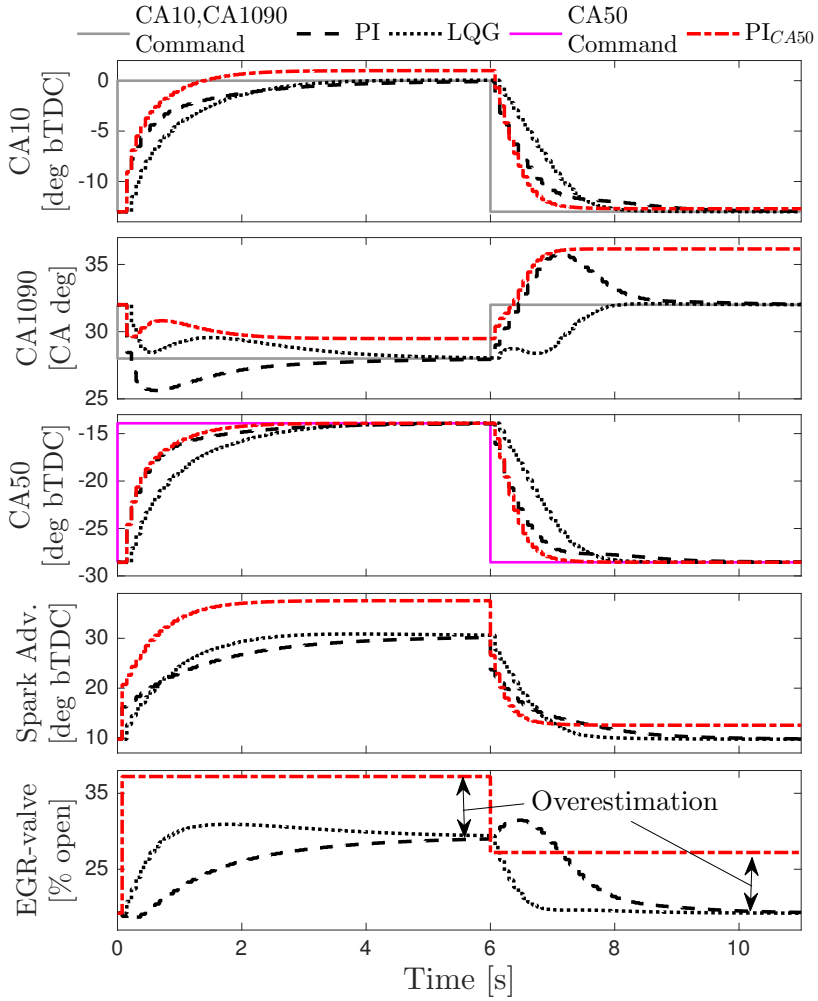


Figure 2.12: Simulated response of PI, LQG and PI$_{\text{CA50}}$ controllers for overestimation of EGR-valve opening for step Point B → A → B

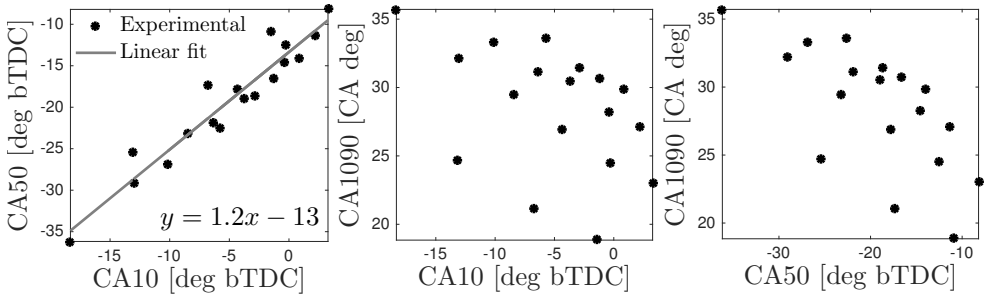


Figure 2.13: Relationship between combustion features: CA10, CA50, and CA1090.

significantly affected on either step command, suggesting that the spark solely can achieve correct CA10 and CA50 values. Figure 2.13 shows plots for the mean values of the combustion features for all spark advance/EGR-valve conditions. Only CA10 and CA50 are linearly related for all these conditions, which means that controlling one feature is equivalent to controlling the other. Also note that the slope of the interpolation is close to one, explaining why the error in CA10 in the $PI_{CA50}$ controller under EGR uncertainty is small. Thus, another possible TITO controller can use CA50 and CA1090 measurements to control the combustion process using SA and EGR-valve. This new input-to-output coupling is of special interest because of the known robustness of CA50 to disturbances in speed, load, fuel characteristics, and equivalence ratio. However, this relationship also implies that the optimal CA10 value should be somehow constant across operating conditions. If that is the case, CA10 has the additional advantage of a lower STDv compared with CA50. Further testing of this claim is needed across different engine speed/load conditions.

## 2.6 Summary

The main objective of this study was to use feedback combustion control to ensure a healthy flame development without slow burns or misfires. A decentralized (PI-based) and a centralized (LQG-based) TITO controllers have been designed and implemented for a robust combustion initiation (CA10) with targeted combustion duration (CA1090). Although typically CA50 is used as a target for combustion control, CA10 has been chosen due to its close relation with the initial flame development period and its lower cycle-to-cycle variability. The controllers adjust spark advance and EGR-valve in a cycle-to-cycle base according to the measured performance outputs (CA10 and CA1090). A control-oriented combustion model was developed based on system identification and used as a tool for control design and linear analysis of the closed-loop system. Evaluation of the transient response demonstrates that the centralize (LQG) controller is better at managing the input-output coupling of the system and the cycle-to-cycle CV compared with the decentralize (PI) controller. Frequency domain analysis points to the advantage of using the LQG controller for efficient actuator coordination. Quantification of the combustion variability indicates that the LQG controller is better than the PI controller at managing and attenuating the cycle-to-cycle and cylinder-to-cylinder variability at steady state operation. Sensitivity analysis of the system under feedback gain variation shows that integral gains have a high impact in CV at steady state, and the authors recommend to use

low gain values for further applications. Similar results were obtained when looking at the output sensitivity function based on the LTI combustion model, which indicates that such model can be a powerful design and analysis tool for at least the one speed/load condition explored in this paper. Although the control-oriented model will change at different speed/load conditions, the methodology explained in this paper for implementing and tuning a feedback combustion controller will be the same.

# CHAPTER III

# Linear Stochastic Modeling and Control of Diluted Combustion for Spark Ignition Engines

## 3.1 Motivation

The combustion process in spark-ignition (SI) engines exhibits cycle-to-cycle variability, which imposes limits on engine operation. When exhaust gas recirculation (EGR) is used to increase engine efficiency, the combustion variability (CV) increases and spark advance (SA) must be re-tuned to achieve maximum brake torque. In order to maximize EGR benefits without excessive cyclic CV, feedback control can be applied to modify EGR and SA accordingly. This study presents a control-oriented combustion model that captures the stochastic properties of combustion features. A linear quadratic Gaussian (LQG) controller is used to modify SA and EGR to achieve a particular *combustion shape*, characterized by the initiation and duration angles. Using stochastic control theory for linear Gaussian systems, analytical solutions for the cyclic variability of the combustion process and the control commands under closed-loop operation are derived. This methodology is validated against experimental engine data and results at transient and steady state operation are presented.

## 3.2 Open-loop Model

It was showed in the previous Chapter that combustion features CA10, CA50 and CA1090 present normal distributions $\mathcal{N}(\mu_{\text{xx}}, \sigma^2_{\text{xx}})$ (mean: $\mu_{\text{xx}}$ and standard deviation: $\sigma_{\text{xx}}$) when the system is operated at stationary conditions. Under that assumption, the probability density function (PDF) and time series properties of all

features CAxx,CAyy are completely characterized by:

$$\begin{aligned}
\textbf{Expectations:}\ & \mu_{\mathrm{xx}} = E[\mathrm{CAxx}] \\
\textbf{Variances:}\ & \sigma^2_{\mathrm{xx}} = \mathrm{var}(\mathrm{CAxx}) \\
\textbf{Covariances:}\ & \mathrm{cov}(\mathrm{CAxx}_k, \mathrm{CAyy}_k) \\
\textbf{Covariance functions:}\ & \mathrm{cov}(\mathrm{CAxx}_{k+m}, \mathrm{CAyy}_k)
\end{aligned}$$

for {xx,yy}∈ {10,1090} and for any cycle $k$ [52]. This behavior motivates the use of a Gaussian stochastic model for the open-loop system. Figure 3.1 shows the cylinder pressure trace and fuel mass fraction burned for 2000 steady state engine cycles. The motored pressure curve is shown as a reference for incomplete combustion. As discussed by [3], incomplete combustion leaves residual charge available for the next cycle. This works as a coupling mechanism and generates nonzero covariance functions $\mathrm{cov}(\mathrm{CAxx}_{k+1}, \mathrm{CAxx}_k)$, implying serial correlation for the combustion process. Hence, the SA/EGR combination for this study was chosen such that no partial burned cycles or misfires occurred.

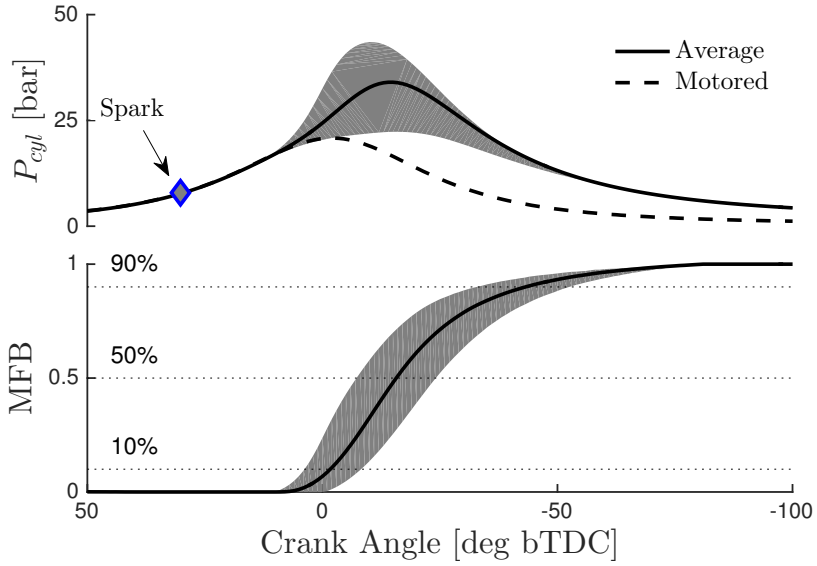


Figure 3.1: In-cylinder pressure ($P_{\mathrm{cyl}}$) and fuel mass fraction burned (MFB) as functions of CA deg. Grey colored region represents 2000 engine cycles.

### 3.2.1 General Linear Gaussian System

Consider the linear discrete-time stochastic system:

$$\begin{aligned} x_{k+1} &= Ax_k + Bu_k + Gw_k \\ y_k &= Cx_k + Hv_k \end{aligned} \tag{3.1}$$

where:

$$x_0 \sim \mathcal{N}(0, \Sigma_0), \quad w_k \sim \mathcal{N}(0, Q), \quad v_k \sim \mathcal{N}(0, R) \tag{3.2}$$

are the basic random variables, which are assumed to be mutually independent. Suppose that under certain constant open-loop command $u_k = U$ the system reaches steady state. Define:

$$\textbf{State Covariance: } \Sigma_\infty^x = \lim_{k\to\infty} \operatorname{cov}(x_k, x_k) \tag{3.3}$$

then, using Eqn. (3.1), the steady state covariance and covariance function of the output can be calculated as [52, Chap.3]:

$$\textbf{Output Covariance:} \quad \Sigma_\infty^{y,\mathrm{OL}} = \lim_{k\to\infty} \operatorname{cov}(y_k, y_k) = C\Sigma_\infty^x C^T + HRH^T \tag{3.4}$$

$$\textbf{Output Cov. Function:} \quad \Sigma_\infty^{y,\mathrm{OL}}(m) = \lim_{k\to\infty} \operatorname{cov}(y_{k+m}, y_k) = CA^m\Sigma_\infty^x C^T, \tag{3.5}$$

for $m \geqslant 1$. Steady state requires stability of matrix $A$ and reachability of the pair $(A, \sqrt{GQG^T})$. Under these assumptions, the steady state covariance $\Sigma_\infty^x$ can be obtained by finding the positive definite root of:

$$\textbf{Lyapunov equation: } \Sigma_\infty^x = A\Sigma_\infty^x A^T + GQG^T. \tag{3.6}$$

### 3.2.2 Open-loop Steady State Properties

For feedback combustion control, the inputs and outputs of the system are defined:

$$u_k = \begin{bmatrix} \mathrm{SA}_k \\ \mathrm{EGR}_k \end{bmatrix}, \quad y_k = \begin{bmatrix} \mathrm{CA10}_k \\ \mathrm{CA1090}_k \end{bmatrix} \tag{3.7}$$

The feature CA10 was chosen for control since, according to Section 2.2, it displays the least amount of variability. The start of combustion CA10 also correlates well with the initial flame development angle, which is mainly determined by the spark advance. The combustion duration CA1090 captures the effect of EGR in the combustion kinetics, elongating the combustion as EGR levels increase. For any two features

CAxx and CAyy, with xx,yy $\in \{10, 1090\}$, define:

$$\textbf{Correlation Function:} \quad \operatorname{corr}(\mathrm{CAxx}_{k+m}, \mathrm{CAyy}_k) = \frac{\operatorname{cov}(\mathrm{CAxx}_{k+m}, \mathrm{CAyy}_k)}{\sigma_{\mathrm{xx}}\sigma_{\mathrm{xx}}} \tag{3.8}$$

which is the normalized version of the covariance function. By compiling the four possible combinations of correlations between CA10 and CA1090 in one matrix:

**Correlation matrix:**

$$\chi_{\infty}^{y,\mathrm{OL}}(m) = \begin{bmatrix} \operatorname{corr}(\mathrm{CA10}_{k+m}, \mathrm{CA10}_k) & \operatorname{corr}(\mathrm{CA10}_{k+m}, \mathrm{CA1090}_k) \\ \operatorname{corr}(\mathrm{CA1090}_{k+m}, \mathrm{CA10}_k) & \operatorname{corr}(\mathrm{CA1090}_{k+m}, \mathrm{CA1090}_k) \end{bmatrix}. \tag{3.9}$$

Note that the output covariance function $\Sigma_{\infty}^{y,\mathrm{OL}}(m)$ and the correlation matrix $\chi_{\infty}^{y,\mathrm{OL}}(m)$ are related by:

$$\chi_{\infty}^{y,\mathrm{OL}}(m) = \operatorname{diag}\{\sigma_{10}, \sigma_{1090}\}^{-1} \cdot \Sigma_{\infty}^{y,\mathrm{OL}}(m) \cdot \operatorname{diag}\{\sigma_{10}, \sigma_{1090}\}^{-1} \tag{3.10}$$

with $\Sigma_{\infty}^{y,\mathrm{OL}}(0) = \Sigma_{\infty}^{y,\mathrm{OL}}$. Figure 3.2 shows the different elements of $\chi_{\infty}^{y,\mathrm{OL}}(m)$ as a function of engine cycle lags. Recall that if the measurements $\{\mathrm{CAxx}_1, \ldots, \mathrm{CAxx}_N\}$ are independent Gaussian random variables (white noise), the normalized standard error (SE) of the sample mean can be estimated as:

$$\mathrm{SE} = \frac{1}{\sigma_{\mathrm{xx}}}\sqrt{\operatorname{var}\left(\frac{\sum \mathrm{CAxx}_i}{N}\right)} = \frac{1}{\sigma_{\mathrm{xx}}}\sqrt{\frac{\sigma_{\mathrm{xx}}^2}{N}} = \frac{1}{\sqrt{N}}. \tag{3.11}$$

In order to determine if the time series behaves as a white noise process with 95% confidence, the corresponding SE equals $2/\sqrt{N}$. This bound is represented in Figure 3.2 by the solid red line and it is assumed that the coefficients falling between such bounds are equivalent to zero. Therefore, the correlation matrix is equivalent to:

$$\chi_{\infty}^{y,\mathrm{OL}}(m) = \begin{cases} \begin{bmatrix} 1 & \rho \\ \rho & 1 \end{bmatrix} & , \text{if } m = 0 \\ \\ 0 & , \text{if } m \geqslant 1. \end{cases} \tag{3.12}$$

The zero correlation is a product of the cyclic independence of the combustion process. Note that this result will not hold if partially burned cycles of misfires are present. Given that $\sigma_{10}, \sigma_{1090} \neq 0$, and assuming that the system dynamic behavior is not

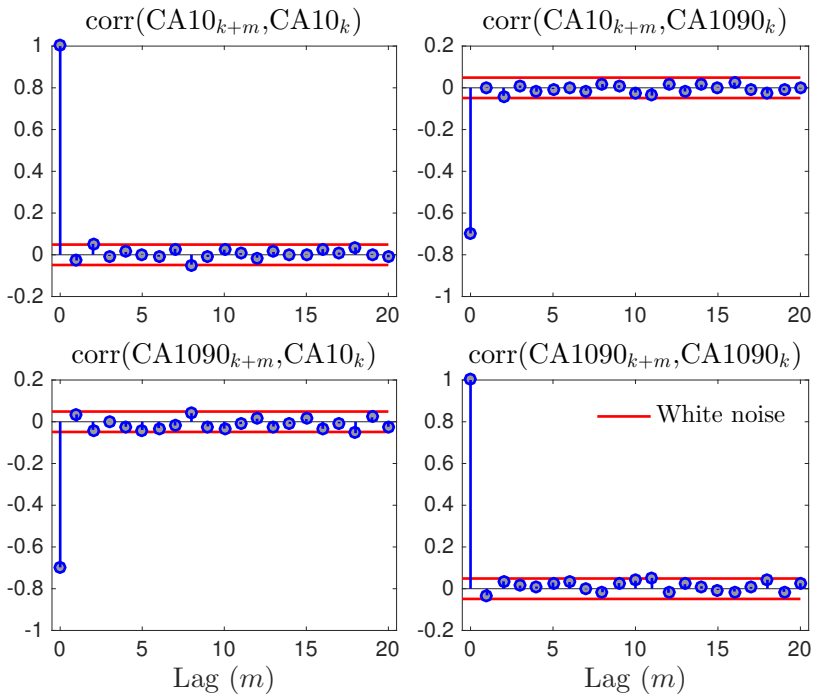


Figure 3.2: Coefficients of correlation matrix $\chi_\infty^{y,\mathrm{OL}}(m)$ for a sample of 1600 engine cycles during steady state.

trivial, Eqns. (3.5) and (3.10) imply the following:

$$\chi_\infty^{y,\mathrm{OL}}(m) = 0 \iff \Sigma_\infty^{y,\mathrm{OL}}(m) = 0 \iff \Sigma_\infty^{x} = 0. \tag{3.13}$$

The output covariance on the other hand, simplifies to:

$$\Sigma_\infty^{y,\mathrm{OL}} = HRH^T = \begin{bmatrix} \sigma_{10}^2 & \rho\sigma_{10}\sigma_{1090} \\ \rho\sigma_{10}\sigma_{1090} & \sigma_{1090}^2 \end{bmatrix}. \tag{3.14}$$

Given that $\Sigma_\infty^{y,\mathrm{OL}}$ is a symmetric, positive definite matrix, the spectral decomposition can be written as $\Sigma_\infty^{y,\mathrm{OL}} = V\Lambda V^T$. Here, $\Lambda$ is the diagonal matrix of eigenvalues and $V$ is an orthogonal matrix with corresponding eigenvectors. Therefore, the output equation for the open-loop combustion model can be written as:

$$y_k = Cx_k + Vv_k, \quad v_k \sim \mathcal{N}(0, \Lambda). \tag{3.15}$$

Figure 3.3 compares the theoretical output covariance $\Sigma_\infty^{y,\mathrm{OL}}$ with the experimental distribution of the random variable:

$$\Delta\mathrm{CAxx} = \mathrm{CAxx} - \mu_{\mathrm{xx}}. \tag{3.16}$$

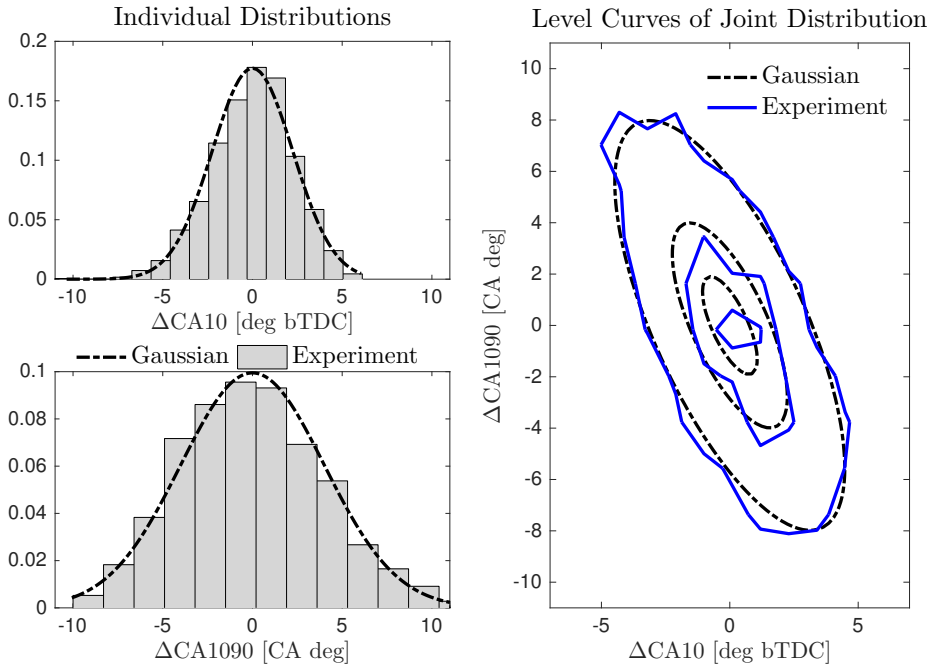


Figure 3.3: Joint and marginal PDFs for theoretical and experimental $\Sigma_\infty^{y,\mathrm{OL}}$. Equiprobable level curves of joint PDF represent compact sets containing 38%, 68%, and 95% of the total distribution.

The linear Gaussian model not only captures the properties of marginal PDFs, but can also reproduce the behavior of the joint PDF. Looking back to the Lyapunov Eqn. (3.6), $\Sigma_\infty^x = 0$ implies that $GQG^T = 0$. Assuming $G \neq 0$, the only way to satisfy the equality is with $Q = 0$. Therefore, the random variable $w_k$ degenerates to a constant value of zero. Hence, the dynamics of the system are *purely deterministic*. Combining this observation with Eqn. (3.15), the linear stochastic model for combustion control is:

$$\textbf{Open-loop system:} \quad \begin{aligned} x_{k+1} &= Ax_k + Bu_k \\ y_k &= Cx_k + Vv_k \end{aligned} \tag{3.17}$$

where $\{v_k\} \sim \mathcal{N}(0, \Lambda)$ is a white noise precess.

### 3.2.3 Open-loop Transient Properties

Although the stochasticity of the flame development governs the combustion process at steady state, the transient response has different characteristics. A step change in EGR valve will alter the manifold filling dynamics and the heat transfer properties of the charge. Moreover, the study performed by [46] showed that changes in spark

timing strongly affect the cylinder surface heat flux during the power stroke. Based on such observations, a first order response is expected for changes in command values. System identification was performed in in the previous Chapter to determine matrices $A$ and $B$ in the linear model. The matrix $C$, however, was determined by calculating the Jacobian of a nonlinear model of the output, as follows:

$$\begin{matrix} \text{CA10} = f_{10}(\text{SA,EGR}) \\ \text{CA1090} = f_{1090}(\text{SA,EGR}) \end{matrix} \Rightarrow C = \begin{bmatrix} \dfrac{\partial f_{10}}{\partial \text{SA}} & \dfrac{\partial f_{10}}{\partial \text{EGR}} \\ \dfrac{\partial f_{1090}}{\partial \text{SA}} & \dfrac{\partial f_{1090}}{\partial \text{EGR}} \end{bmatrix} \tag{3.18}$$

Functions $f_{10}$ and $f_{1090}$ were computed after steady state engine mapping. Figure 3.4 shows the open-loop model validation, excluding the variability induced by $v_k$. Although the cyclic CV makes it hard to evaluate the accuracy of the model, the comparison of statistical properties for the closed-loop system will further validate of the model.

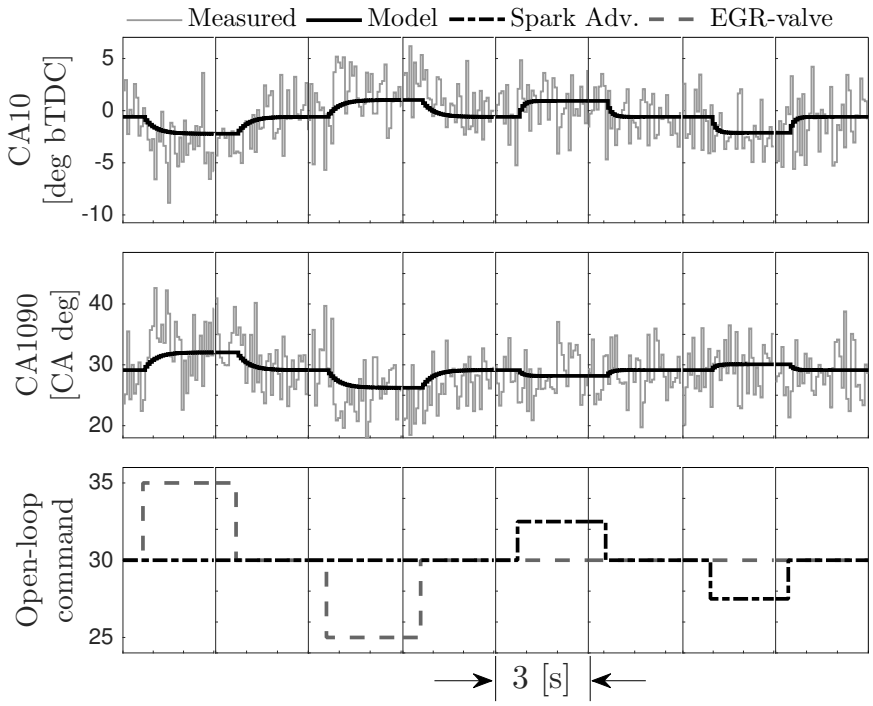


Figure 3.4: Comparison of linear model and experiments under step perturbations in SA and EGR valve.

## 3.3 Closed-loop Model

Recall that in Section 2.3.4 the stochastic control problem of tracking a step reference command $r$ based on output feedback was discussed. Integral control can achieve zero steady state tracking error with the additional advantage of rejecting constant output disturbances. The open-loop system is then augmented with the following integrator states:

$$\textbf{Discrete-time integrator: } z_{k+1} = z_k + (y_k - r) \tag{3.19}$$

Consider further the case when the controller is designed to minimize the expected quadratic cost:

$$\textbf{Cost: } J = E\left[\sum_{k=0}^{\infty} y_k^T \Gamma_y y_k + z_k^T \Gamma_z z_k + u_k^T \Omega u_k\right] \tag{3.20}$$

subject to the dynamics described by Eqns. (3.17) and (3.19). From stochastic control theory, we know that from all feasible control policies that minimize the cost, Markov policies (which only depend on the current state) are optimal [52, Chap. 6]. In particular for linear systems, the use of a control law linear on states:

$$\textbf{State Feedback: } u_k = -K_x x_k - K_z z_k \tag{3.21}$$

is sufficient to minimize the cost function $J$. Since we do not have access to the states, the conditional distribution of $x_k$ given all the information at time $k$, i.e. $\{y_0, \ldots, y_k, u_0, \ldots, u_{k-1}\}$, is required for feedback control. In the linear Gaussian case, the conditional distribution $p(x_k \mid y_0, \ldots, y_k, u_0, \ldots, u_{k-1})$ is given by the Kalman filter and is finite-dimensional. Moreover, the steady state Kalman filter is a linear estimator of the states. Consider the following linear observer for state estimation:

$$\textbf{State Estimator: } \widehat{x}_{k+1} = (A - LC)\widehat{x}_k + Bu_k + Ly_k \tag{3.22}$$

where $L$ is the estimator gain. For feedback control, replace the current state in Eqn. (3.21) by the estimated state for Eqn. (3.22). The feedback gains $K_x, K_z$ resulted from the solution of the *Linear Quadratic Regulator* control problem and the estimator gain $L$ is the solution of the *Linear Quadratic Estimator*.

By augmenting the open-loop system (3.17) with the discrete-time integrator (3.19) and the state estimator (3.22), and by using the state feedback law (3.21)

to close the loop, one can determine that the system under control satisfies:

**Closed-loop system:**

$$\begin{aligned}
\begin{bmatrix} x_{k+1} \\ z_{k+1} \\ \widehat{x}_{k+1} \end{bmatrix} &= \begin{bmatrix} A & -BK_z & -BK_x \\ C & I & 0 \\ LC & -BK_z & A - LC - BK_x \end{bmatrix} \begin{bmatrix} x_k \\ z_k \\ \widehat{x}_k \end{bmatrix} + \begin{bmatrix} 0 \\ -I \\ 0 \end{bmatrix} r + \begin{bmatrix} 0 \\ V \\ LV \end{bmatrix} v_k \\
y_k &= \begin{bmatrix} C & 0 & 0 \end{bmatrix} \begin{bmatrix} x_k \\ z_k \\ \widehat{x}_k \end{bmatrix} + V v_k, \qquad v_k \sim \mathcal{N}(0, \Lambda).
\end{aligned} \tag{3.23}$$

Let $\Psi = \begin{bmatrix} x_k & z_k & \widehat{x}_k \end{bmatrix}^T$, we simplify the notation by:

$$\begin{aligned}
\Psi_{k+1} &= A_{\mathrm{CL}} \Psi_k + B_{\mathrm{CL}} r + G_{\mathrm{CL}} v_k \\
y_k &= C_{\mathrm{CL}} \Psi_k + V v_k.
\end{aligned} \tag{3.24}$$

Note the similarities between the closed-loop system and the general linear Gaussian system described in Section 3.2.1. We will summon previous results to analyze steady state properties of the closed-loop system.

### 3.3.1 Closed-loop Steady State Properties

Since the matrix $A_{\mathrm{CL}}$ is stable by design, the system will eventually reach steady state. Let $\Sigma_\infty^\Psi$ be the closed-loop state covariance at steady state, then:

$$\begin{aligned}
\Sigma_\infty^\Psi &= \lim_{k\to\infty} \mathrm{cov}(A_{\mathrm{CL}} \Psi_k + B_{\mathrm{CL}} r + G_{\mathrm{CL}} v_k) \\
&= \lim_{k\to\infty} \mathrm{cov}(A_{\mathrm{CL}} \Psi_k + G_{\mathrm{CL}} v_k) \\
&= \lim_{k\to\infty} \mathrm{cov}(A_{\mathrm{CL}} \Psi_k) + \lim_{k\to\infty} \mathrm{cov}(G_{\mathrm{CL}} v_k) \\
\therefore \Sigma_\infty^\Psi &= A_{\mathrm{CL}} \Sigma_\infty^\Psi A_{\mathrm{CL}}^T + G_{\mathrm{CL}} \Lambda G_{\mathrm{CL}}^T.
\end{aligned} \tag{3.25}$$

The first equality follows from Eqn. (3.24). The second holds since $B_{\mathrm{CL}} r$ is constant at steady state. The third equality holds because $\Psi_k$ is a function of the random variables $\{v_{k-1}, \ldots, v_0\}$; hence, $\Psi_k$ and $v_k$ are independent. Note that Eqn. (3.25) is the closed-loop Lyapunov equation. Given that the pair $(A_{\mathrm{CL}}, G_{\mathrm{CL}}\sqrt{\Lambda})$ is reachable, the Lyapunov equation has a unique positive definite solution. Intuitively, the reachability condition is satisfied because the output noise propagates through the closed-loop system via the integrator and estimator states. Note also that the state

covariance $\Sigma_\infty^\Psi$ is a function of state feedback gain, estimator gain, and open-loop steady state covariance. Since the control is a linear function of the states, its steady state covariance can be calculated as:

$$\textbf{Control Covariance: } \Sigma_\infty^u = \begin{bmatrix} 0 & K_z & K_x \end{bmatrix} \Sigma_\infty^\Psi \begin{bmatrix} 0 \\ K_z \\ K_x \end{bmatrix} \tag{3.26}$$

which is directly determined by the feedback gains. Note that if the state gains are high (aggressive feedback) then the variability of the control commands will be amplified. Moreover, similar to Eqn. (3.5), the covariance function of the control signal can be computed from $\Sigma_\infty^\Psi$ as follows:

$$\textbf{Control Cov. Function: } \Sigma_\infty^u(m) = \begin{bmatrix} 0 & K_z & K_x \end{bmatrix} A_{\text{CL}}^m \Sigma_\infty^\Psi \begin{bmatrix} 0 \\ K_z \\ K_x \end{bmatrix} \tag{3.27}$$

Finally, define the control correlation matrix as follows:

$$\chi_\infty^u(m) = \text{diag}\{\sigma_{\text{SA}}, \sigma_{\text{EGR}}\}^{-1} \cdot \Sigma_\infty^u(m) \cdot \text{diag}\{\sigma_{\text{SA}}, \sigma_{\text{EGR}}\}^{-1} \tag{3.28}$$

The left set of plots in Figures 3.5 and 3.6 compares the theoretical steady state control covariance $\Sigma_\infty^u$ and correlation matrix $\chi_\infty^u(m)$ with the experimental distribu-

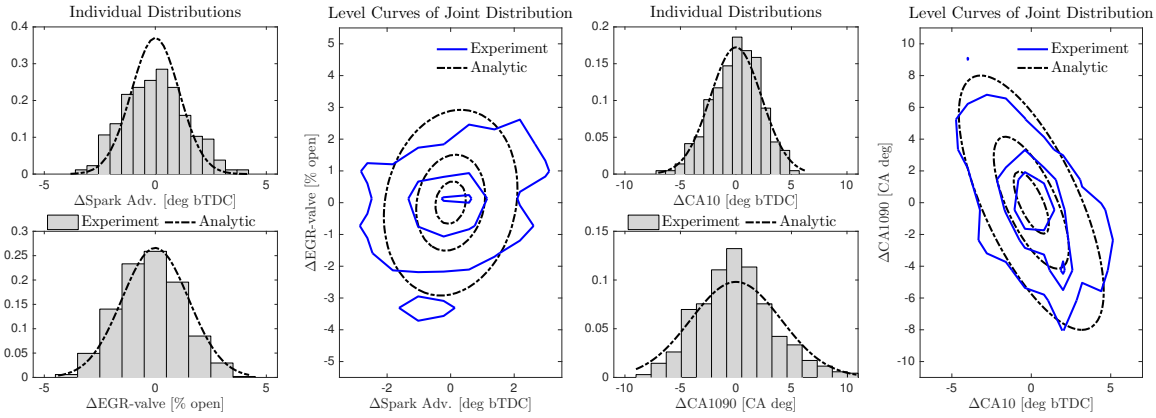


Figure 3.5: Joint and marginal PDFs for theoretical and experimental $\Sigma_\infty^u$ (left) and $\Sigma_\infty^{y,\text{CL}}$ (right). Equiprobable level curves of joint PDF represent compact sets containing 38%, 68%, and 95% of the total distribution.

tion of the zero-mean random variables:

$$\Delta\text{SA} = \text{SA} - \mu_{\text{SA}}, \quad \Delta\text{EGR} = \text{EGR} - \mu_{\text{EGR}}. \tag{3.29}$$

The analytical solution closely describes the marginal and joint distributions of the control commands, as well as the time series properties. One can also define the output covariance and covariance function for the closed-loop system, as follows:

$$\textbf{Output Covariance:} \quad \begin{aligned} \Sigma_\infty^{y,\text{CL}} &= C_{\text{CL}}\Sigma_\infty^\Psi C_{\text{CL}}^T + V\Lambda V^T \\ &= C_{\text{CL}}\Sigma_\infty^\Psi C_{\text{CL}}^T + \Sigma_\infty^{y,\text{OL}} \end{aligned} \tag{3.30}$$

$$\textbf{Output Cov. Function:} \quad \Sigma_\infty^{y,\text{OL}}(m) = C_{\text{CL}}A_{\text{CL}}^m\Sigma_\infty^\Psi C_{\text{CL}}^T. \tag{3.31}$$

The change in output covariance from open-loop to closed-loop operation is the positive definite matrix:

$$\textbf{Combustion Variability Increase:} \quad \begin{aligned} \Delta\Sigma_\infty^y &= \Sigma_\infty^{y,\text{CL}} - \Sigma_\infty^{y,\text{OL}} \\ &= C_{\text{CL}}\Sigma_\infty^\Psi C_{\text{CL}}^T. \end{aligned} \tag{3.32}$$

This result gives an analytical expression for the increase in variability due to the feedback loop. Consider the closed-loop output correlation matrix $\chi_\infty^{y,\text{CL}}(m)$ similarly defined as in Eqn. (3.28). The right set of plots in Figures 3.5 and 3.6 compare the theoretical steady state covariance $\Sigma_\infty^{y,\text{CL}}$ and the coefficients of $\chi_\infty^{y,\text{CL}}(m)$ with the

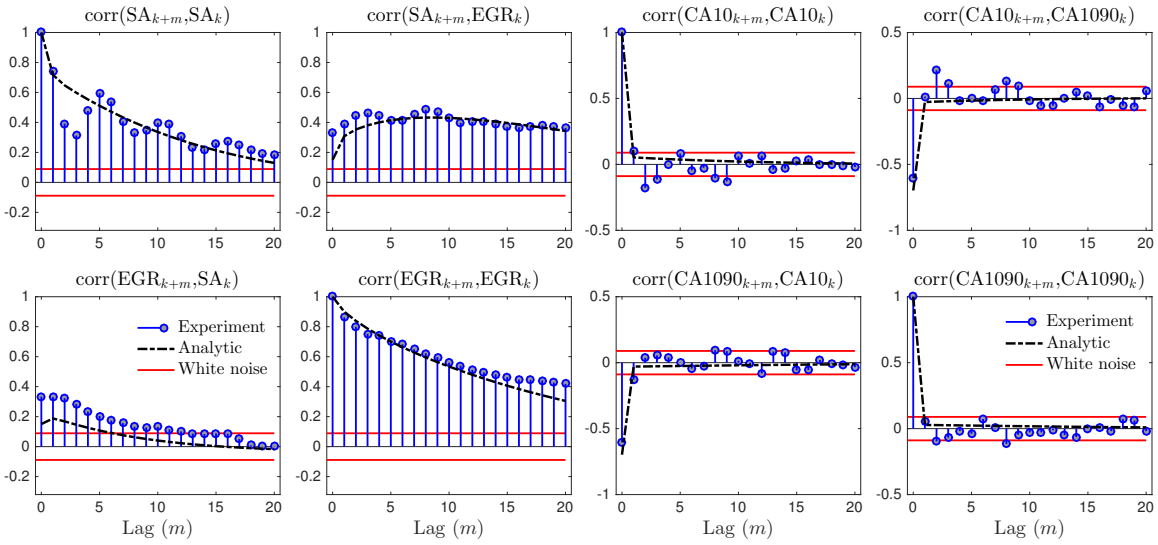


Figure 3.6: Coefficients of correlation matrices $\chi_\infty^u(m)$ (left) and $\chi_\infty^{y,\text{CL}}(m)$ (right) for a sample of 600 engine cycles.

experimental distribution. The linear model in closed-loop steady state operation can describe the stochastic properties of the joint and marginal distributions and it can also capture the time series correlation of the output signals.

### 3.3.2 Closed-loop Transient Response

Simultaneous step commands in CA10 and CA1090 were issued in closed-loop operation. A full study of the transient properties of the step response can be found in [40]. Figure 3.7 shows the experimental response together with the model simulation. In this case, the non-linear functions $f_{10}, f_{1090}$ were used to calculate the output values for feedback control. This results further validate the usefulness of the stochastic model to determine steady state and transient properties of the combustion process under closed-loop control.

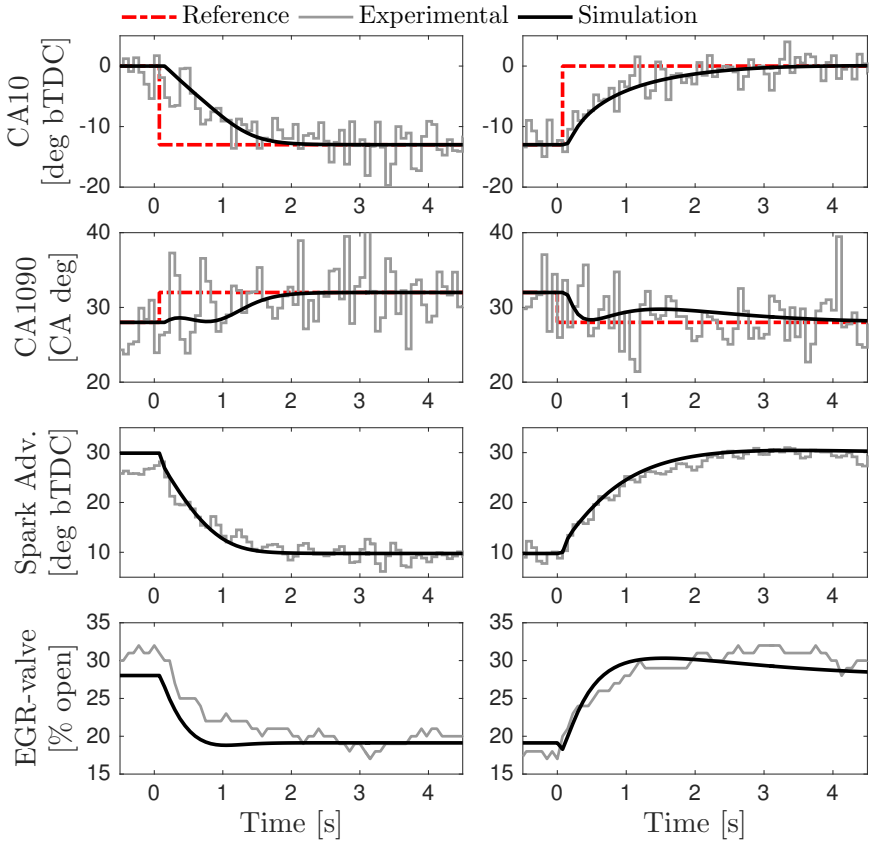


Figure 3.7: Comparison between experimental and non-linear model for step command at closed-loop operation.

## 3.4 Summary

A simple stochastic control-oriented combustion model has been developed for diluted combustion when cyclic events are independent. A linear quadratic Gaussian multivariable controller was implemented to regulate EGR valve and spark advance in order to achieve a target combustion process. In closed-loop operation, the linear model is able to predict the stochastic properties of the controlled combustion process at steady state, based on the statistical information collected in open-loop operation. In other words, given the open-loop stochastic linear model and the LQG gains, the closed-loop statistics of the system can be predicted. Moreover, an analytical solution is presented for the increase in combustion variability due to the feedback loop. Experimental results show the accuracy of the analytical prediction. The serial correlation properties, however, will not hold if the engine operates at the *misfire limit*, where incomplete combustion induces cyclic correlation. Although the controller has been tested at one operating condition, the methodology is valid for any operating condition with nominal combustion events.

# CHAPTER IV

# Stochastic Feedback Combustion Control at High Dilution Limit

## 4.1 Motivation

This study focuses on the development of a feedback control strategy to maximize the benefits of cooled EGR while, simultaneously, minimizing CV introduced by the feedback loop. A two-input two-output (TITO) controller was designed in Section 2.3.4 for spark advance and EGR valve to control the combustion process at conservative EGR levels with low CV. Extending such prior work, the linear quadratic Gaussian (LQG) controller has been redesigned to shift the engine operating condition from low-EGR to high-EGR levels. The controller gains were tuned to accurately track the target combustion, but minimize the CV that is re-introduced in the system as a result of the TITO feedback loop.

Figure 4.1 shows the block diagram of the proposed controller. The main components are discussed as follows: Section 4.2 shows the engine operating condition used as control target. Section 4.3 describes the stochastic control-oriented combustion model used for control design and simulations. Section 4.4 presents the LQG controller design and the analysis of the fundamental limitations of the control problem at the high dilution limit. Specifically, it is shown that the plant directionally at the target operating point requires large control signals that can 1) cause sporadic misfires, and 2) cause significant changes in brake torque.

## 4.2 Target Combustion Shape

The data presented in this study was collected the same engine as Section 2.2. Combustion phasing is a well known metric for engine efficiency since its optimum

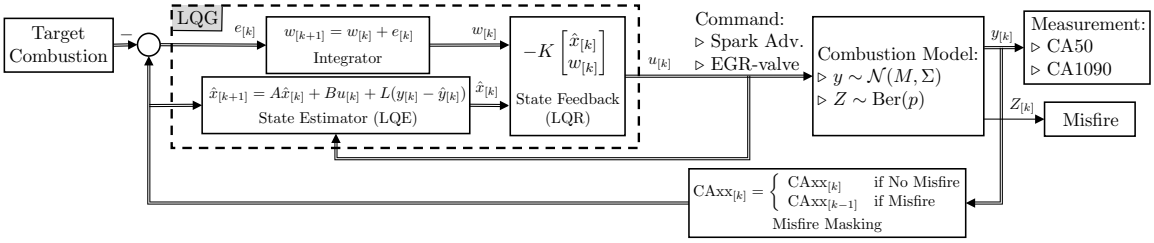


Figure 4.1: Block diagram of closed-loop system used in simulations with stochastic combustion model, misfire masking logic, and LQG controller.

value lies between −5 and −11 [deg bTDC] for a conventional engine and it has low sensitivity with respect to changes in equivalence ratio, EGR, speed, and load [31]. Control of the combustion duration is particularly important at high EGR levels since overly long CA1090 reduces the cylinder peak pressure and increases CV [13]. The *combustion shape* is defined by the MFB trace, characterized by the pair (CA50, CA1090). In this study, we identified an operating condition with high EGR levels located close to the misfire limit that can improve fuel economy. This point was compared against a high efficient point without EGR, close to the knock limit, as shown in Table 4.1. As expected, EGR increases CV, reduces brake specific fuel consumption (BSFC), and suppresses the likelihood of knock.

Table 4.1: Operating conditions at same load but different EGR levels.

| | **Point X** | **Point Y** |
|---|---|---|
| SA [deg bTDC] | 20 | 45 |
| EGR valve [% open] | 0 | 40 |
| CA50 [deg bTDC] | −8.3 ($\sigma_{50} = 1.8$) | −11.1 ($\sigma_{50} = 4.7$) |
| CA1090 [CA deg] | 23.2 ($\sigma_{1090} = 2.1$) | 40.1 ($\sigma_{1090} = 5.6$) |
| $\mathrm{CoV}_{\mathrm{IMEP}}$ | 0.6% | 5.2% |
| BSFC [g/kWh] | 258.8 | 253.8 (−1.9%) |

Steady state data within the feasible combustion region were recorded at different combinations of SA and EGR valve positions. The estimation of the mean values of CA50 and CA1090 ($\mu_{50}$ and $\mu_{1090}$) was accomplished by third order polynomial interpolations of such values. Figure 4.2 shows the contour plots of the estimated combustion features. Experimentally, not all SA/EGR valve combinations were achievable due to combustion instability, mainly due to combustion variability. Therefore, a feasible region has been outlined based on the following three limits [18]:

1. *Knock limit:* Maximum SA at low EGR levels at which spark knock is avoided.

2. *Misfire limit:* Maximum SA at medium-high EGR levels at which low cylinder temperature, dilution, and excessive turbulence prevent combustion from starting.
3. *Partial burn limit:* Minimum SA at high EGR levels where the flame quenches before consuming completely the end gas, increasing CV.

These limits however, often require a probabilistic approach. For instance, Quader [58] defines the misfire limit where the *misfire rates* is around 0.5-0.8%, while Peyton Jones [59] defines the knock limit where the probability of knocking is 1%.

Note that a constant value of CA50 $= -11$ [deg bTDC] maintains the engine operating close to the knock and misfire limit, maximizing SA for better fuel economy. Therefore, the engine operation will be restricted to such constant CA50 level curve near the engine stable operating limit. This static map however does not capture the CV. Thus, a more rigorous statistical model is required to estimate the amount of CV produced by the controlled system.

## 4.3 Combustion Model

### 4.3.1 Stochastic Model for Combustion Variability

Similar to Figure 4.2, standard deviation values of the CA50 and CA1090 (denoted by $\sigma_{50}$ and $\sigma_{1090}$) estimated at different steady state points can be interpolated by third order polynomials. Figure 4.3 shows the steady state statistics of CA50 and

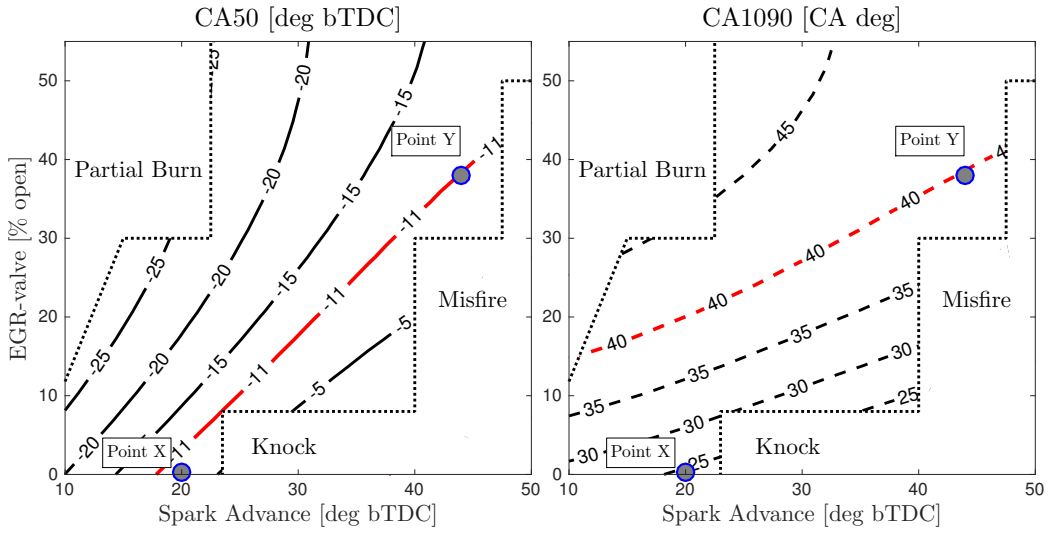


Figure 4.2: Level curves of combustion features CA50 and CA1090 calculated over the engine feasible region as function of SA and EGR valve opening.

CA1090 experimentally measured during 2000 engine cycles at POINT Y. Note that both combustion features are approximately Gaussian distributed, then:

$$\text{CAxx} \sim \mathcal{N}(\mu_{\text{xx}}, \sigma^2_{\text{xx}}), \quad \text{xx} \in \{50, 1090\}. \tag{4.1}$$

These combustion features however are not independent variables since CA10 < CA50 < CA90, if measured bTDC. Let $\rho$ be the *correlation coefficient* between the system outputs, which experimentally was determined to be $\rho = -0.85$ . If such variables have a *bivariate normal distribution*, then the open-loop response $y = \begin{bmatrix}\text{CA50} & \text{CA1090}\end{bmatrix}^T$ satisfies:

$$y \sim \mathcal{N}(M, \Sigma), \text{ where}$$
$$M = \begin{bmatrix}\mu_{50} \\ \mu_{1090}\end{bmatrix}, \quad \Sigma = \begin{bmatrix}\sigma^2_{50} & \rho\sigma_{50}\sigma_{1090} \\ \rho\sigma_{50}\sigma_{1090} & \sigma^2_{1090}\end{bmatrix}. \tag{4.2}$$

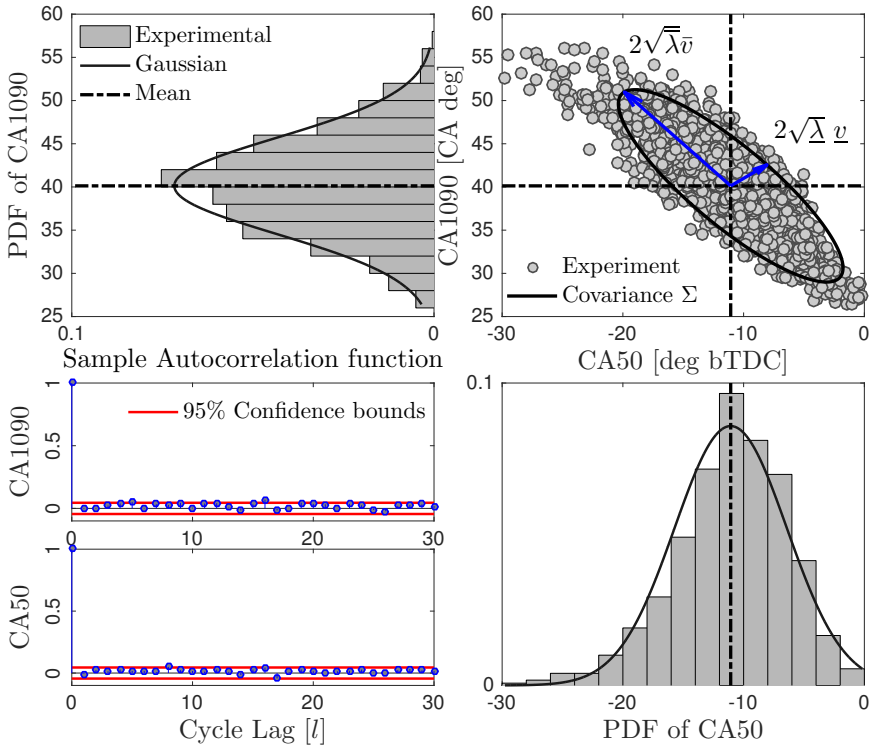


Figure 4.3: Experimental data recorded during 2000 engine cycles at POINT Y. Confidence bounds in autocorrelation test for Gaussian White Noise process.

The covariance $\Sigma$ is a symmetrical, positive definite matrix. Hence, the singular value decomposition can be written as:

$$\Sigma = V\sqrt{\Lambda}\left(V\sqrt{\Lambda}\right)^T, \quad V\sqrt{\Lambda} = \begin{bmatrix}\sqrt{\overline{\lambda}}\overline{v} & \sqrt{\underline{\lambda}}\,\underline{v}\end{bmatrix} \tag{4.3}$$

where $\{\overline{\lambda}, \underline{\lambda}\}$ are the minimum and maximum eigenvalues with corresponding eigenvectors $\{\overline{v}, \underline{v}\}$. The values $\{\sqrt{\overline{\lambda}}, \sqrt{\underline{\lambda}}\}$ can be interpreted as the standard deviations in the eigenvector basis. Therefore, approximately 95% of the measured data should be contained within the ellipse with axis lengths $\{2\sqrt{\overline{\lambda}}, 2\sqrt{\underline{\lambda}}\}$ in the basis $\{\overline{v}, \underline{v}\}$, which is a level curve of the probability density function (PDF) of $y$. The top right plot in Figure 4.3 shows that the data matches the elliptic level curves of the bivariate Gaussian distribution. Hence, the random variables (RVs) CA50 and CA1090 can be modeled as jointly Gaussian.

Figure 4.3 also shows that both outputs have an approximately constant sample autocorrelation, which equals zero for $l > 0$. Therefore, the marginal distributions CA50 and CA1090 can be modeled by Gaussian white noise (GWN) processes. Fundamentally, these RVs are deterministic functions sharing the same *sample space*, i.e. $\{\mathrm{CA50}, \mathrm{CA1090}\}\colon \Omega \to \mathbb{R}$ where $\Omega$ is the set of all feasible combustion events. Therefore, as expected, the absence of serial correlation between cycles $k$ and $k + l$ for both combustion features is the result of the uncorrelation of the elements in the same space $\Omega$. Although the stochasticity of the flame development governs the combustion process at steady state, the transient response has different characteristics. A step change in EGR valve will alter the manifold filling dynamics and the heat transfer properties of the charge. Moreover, the study performed in [46] showed that changes in SA strongly affect the cylinder surface heat flux during the power stroke. Therefore, a dynamical model is essential for an accurate control of the system along the high dilution limit.

### 4.3.2 Control-oriented Transient Combustion Model

A simple, first order, discrete-time dynamical model obtained from system identification was previously shown to be useful for control design and simulation. The proposed TITO system has the following structure:

$$\begin{aligned} x_{\mathrm{SA}}[k+1] &= (1 - a_{\mathrm{SA}})x_{\mathrm{SA}}[k] + a_{\mathrm{SA}}\mathrm{SA}[k] \\ x_{\mathrm{EGR}}[k+1] &= (1 - a_{\mathrm{EGR}})x_{\mathrm{EGR}}[k] + a_{\mathrm{EGR}}\mathrm{EGR}[k] \end{aligned} \tag{4.4}$$

$$\begin{aligned} \text{CA50}_k &= \mu_{50}(x_{\text{SA}}[k], x_{\text{EGR}}[k]) \\ \text{CA1090}_k &= \mu_{1090}(x_{\text{SA}}[k], x_{\text{EGR}}[k]) \end{aligned} \tag{4.5}$$

Equation (4.4) captures the linear dynamics from the control inputs to the states, where $a_{\{\text{SA,EGR}\}}$ are obtained from system identification. Note that at steady state $x_{\text{SA}} = \text{SA}$ and $x_{\text{EGR}} = \text{EGR}$. Figure 4.4 shows the model validation performed around the target POINT Y. If we model the CV as a superposition of the *mean value* and a stochastic output disturbance, large control signals could be required to stabilize the system under integral control.

After full understanding of the system properties, the feedback controller proposed here will: a) shape the combustion from a no-EGR to a high-EGR condition, b) maintain a constant, near optimal, combustion phasing, and c) reduce cycle-to-cycle variability in the control signal.

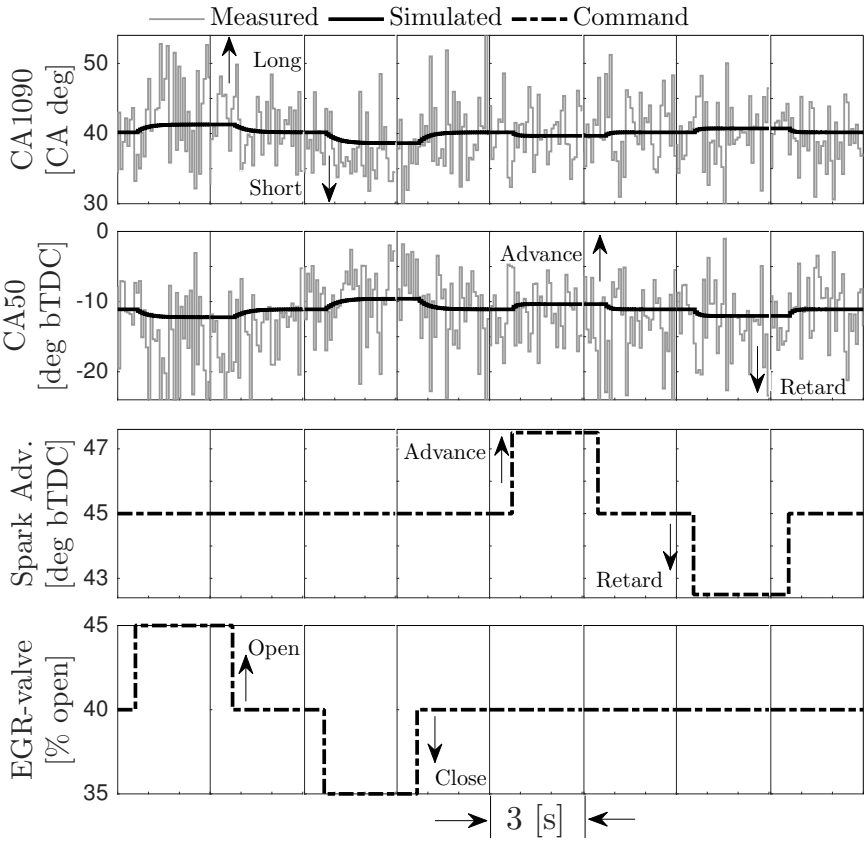


Figure 4.4: Experimental CA1090 and CA50 responses to step commands around POINT Y. Each individual window is equivalent to a period of 3 [s].

## 4.4 Feedback Combustion Control Design

### 4.4.1 Feasibility of Integral Control at the High Dilution Limit

Let $\mathbf{P}_{\mathrm{DC}}$ be the DC gain matrix at POINT Y. Consider the singular value decomposition (SVD) of such matrix:

$$\mathbf{P}_{\mathrm{DC}} = YSU^T \tag{4.6}$$

$$\begin{aligned} Y &= \begin{bmatrix} \bar{y} & \underline{y} \end{bmatrix} = \begin{bmatrix} -0.79 & 0.62 \\ 0.62 & 0.79 \end{bmatrix} \\ \text{where,} \quad S &= \mathrm{diag}\{\bar{\sigma}, \underline{\sigma}\} = \mathrm{diag}\{0.57, 0.07\} \\ U &= \begin{bmatrix} \bar{u} & \underline{u} \end{bmatrix} = \begin{bmatrix} -0.73 & 0.68 \\ 0.68 & 0.73 \end{bmatrix}. \end{aligned} \tag{4.7}$$

The singular vectors $\bar{y}, \bar{u}$ are associated with the singular value $\bar{\sigma}$ and $\underline{y}, \underline{u}$ are linked to the singular value $\underline{\sigma}$. The maximum plant gain $\bar{\sigma}$ is obtained when the input follows $\bar{u}$, which moves the actuators in opposite directions. Increasing EGR and retarding SA will drastically increase CA1090 and retard CA50 since EGR will slow the combustion process and SA will locate the phasing later in the power stroke. Similarly, decreasing EGR and advancing SA will increase the burn rate (decrease CA1090) and advance CA50. The minimum plant gain $\underline{\sigma}$ corresponds to the input $\underline{u}$, which moves the actuators in the same direction. In fact, if SA is advanced (or retarded) accordingly to the EGR increment (or reduction), the combustion phasing and the combustion duration could remained practically unchanged. In this particular direction the actuators have an almost identical effect on the outputs, yielding effectively only one degree of control authority and becoming *almost redundant*. The left plot in Figure 4.5 shows the directionality of the plant when a unit step is commanded. Since combustion control with a fixed phasing is desired, the system could potentially operate close to the direction of minimum gain.

Suppose that the closed-loop system under integral control is used to track a unit step command $y^*$, then the steady state control satisfies $u^* = \mathbf{P}_{\mathrm{DC}}^{-\mathbf{1}} y^*$. Using Eqn. (4.6) it is possible to determine the directions where the command effort will be maximum and minimum, as follows:

$$\mathbf{P}_{\mathrm{DC}}^{-\mathbf{1}} Y = US^{-1}Y^TY = US^{-1} = \begin{bmatrix} \bar{u}/\bar{\sigma} & \underline{u}/\underline{\sigma} \end{bmatrix}. \tag{4.8}$$

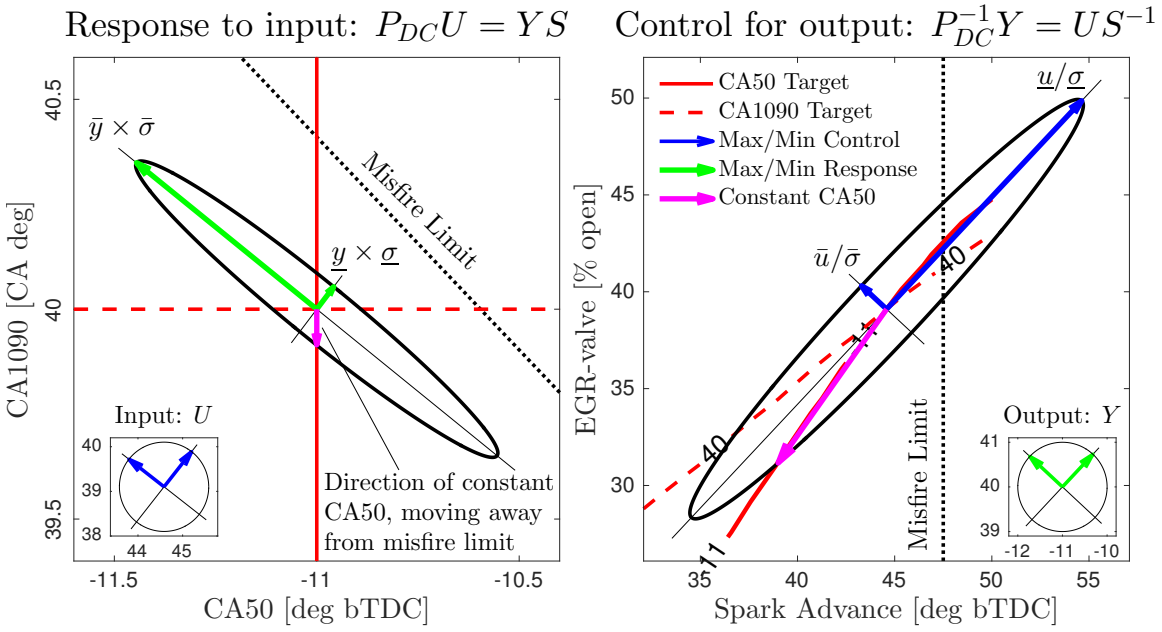


Figure 4.5: Left: Maximum and minimum directions of $\mathbf{P}_{\mathrm{DC}}$ when unit step commands $U$ are issued around Point Y. Right: Maximum and minimum control effort needed to achieve unit step changes $Y$ around Point Y.

The right plot of Figure 4.5 shows the control input required to track $y^*$. Note that the directions with low plant gain need large control signals, which could be problematic for two reasons: 1) a control action following $\underline{u}$ (↗) will drive the system towards regions of non-zero misfire probability, and 2) a control action following the desired CA50 level curve moving away from the misfire limit (↙) will require a large change in SA causing a significant change in torque.

It is well known that scaling the inputs and/or outputs with a different choice of engineering units could potentially reduce the directionality of the system [47, Chap.3]. A more robust way to analyze the fundamental limitation of integral control for ill-conditioned system is by analyzing the *maximum scaled input redundancy angle* (MSRA) introduced in [60]. Let $\mathbf{P}_{\mathrm{DC}} = \begin{bmatrix} P_1 & P_2 \end{bmatrix}$, then the *input redundancy angle* (IRA) defined in [60] is calculated as:

$$\phi_{\mathrm{in}} = \arccos \frac{\left|P_1^T P_2\right|}{\|P_1\| \, \|P_2\|} = 13.7^{\circ}. \tag{4.9}$$

The low value of $\phi_{\mathrm{in}}$ confirms that SA and EGR valve affect the combustion features in approximately the same direction. Although this angle is independent from input scaling, it does depend on output scaling. Suppose that one of the outputs is scaled

by a factor $\lambda > 0$ and that the IRA is denoted by $\phi_{\text{in}}^{\lambda}$, then the MSRA of $\mathbf{P}_{\text{DC}}$ is:

$$\phi_{\text{in}}^{\max} = \sup_{\lambda>0} \phi_{\text{in}}^{\lambda} = 14.1^{\circ}. \tag{4.10}$$

Details of the calculation are explained in [60]. Given that the MSRA is maximum among all possible scaling factors, we conclude that the directionality is a fundamental limitation of the system itself, independent from the choice of units.

If the misfire limit drift towards (or away from) POINT Y, the operating condition can be modified by decreasing (or increasing) CA1090 while maintaining the constant CA50. This new command will generate a large control signal due to the plant directionality. Therefore, the closed-loop system does not need to be designed only for the transient response X→Y, but also for steady state operation at POINT Y.

### 4.4.2 Linear Quadratic Gaussian (LQG) Controller

Consider the linearized TITO system with states $x$, control $u$, output $y$, and augmented integrator states $z$ at POINT Y:

$$\begin{aligned} x_{k+1} &= Ax_k + Bu_k + \gamma_{2_k} \\ y_k &= Cx_k + \gamma_{1_k} \\ z_{k+1} &= z_k + (y_k - y^*) \end{aligned} \tag{4.11}$$

where $y^*$ is the desired target and $\gamma_{\{1,2\}}$ are additive GWN vectors with covariance matrices $\Gamma_{\{1,2\}}$ respectively. The LQG controller consists of a state feedback gain $K$ and a state estimator gain $L$. A steady state linear quadratic estimator (LQE) was used to calculate $L$ based on the stochastic properties of the system. The infinite horizon linear quadratic regulator (LQR) technique was used to calculate $K$, minimizing the following quadratic cost function:

$$J(u) = E\left[\sum_{k=0}^{\infty} y_k^T Q_y y_k + z_k^T Q_{\int} z_k + u_k^T R u_k\right] \tag{4.12}$$

where $E[\cdot]$ denotes expected value. Table 4.2 shows the diagonal matrices $Q_{\{y,\int\}}, R, \Gamma_{\{1,2\}}$ used for calculation.

Since the desired engine operation occurs along the constant CA50 level curve, larger LQR weights are assigned to the CA50/SA output/control combination. By doing so, deviations from the desired steady state value are penalized and, simultane-

Table 4.2: Tuning parameters for LQG controller

| Variable | LQR weights | | | LQE weights | |
|---|---|---|---|---|---|
| | Output ($Q_y$) | Integrator ($Q_\int$) | Control ($R$) | Output Cov. ($\Gamma_1$) | Process Cov. ($\Gamma_2$) |
| CA50/SA | 22 | 0.07 | 1 | $4^2$ | $0.1^2$ |
| CA1090/EGR | 1 | 0.02 | 0.3 | $5^2$ | $0.1^2$ |

ously, the higher bandwidth actuator SA is used to adjust the system more quickly. The low penalty to the integrator reflects the lack of concern about changes in the states. Since the integrator states are calculated directly from the measured outputs, the CV affecting $y_k$ will propagate to the closed-loop system through $w_k$. Low integral gains can reduce the cycle-to-cycle variability of the control signals and, consequently, reduce the CV of the closed-loop system. It was discussed in Section 4.3.1 that the system output is not autocorrelated due to the underlying random process it describes. Therefore, at steady state, any attempt of using previous cycle information is futile and could increase the variability of the control signal. This result suggests that the LQE should operate in open-loop ($L = 0$). For this reason, the covariance matrix $\Gamma_2$ has much smaller diagonal components than $\Gamma_1$ in order to set $L \approx 0$ which will contribute to the estimation of $\hat{x}$ only if the difference $y_k - \hat{y}_k$ is large.

Figure 4.6 shows the simulated closed-loop system using the combustion model presented in Eqn. (4.4) and (4.5). The solid-dotted line (–o–) shows average behavior of the system without CV. Note that the transient response converges to the constant CA50 level curve shortly after the command is issued, operating the engine permanently at the misfire limit. The dotted line (··×··) represents the response when CV is introduced as an output disturbance. The low variability in the control signal is the result of low integral gain and low state estimation gain. The dash-dotted line (-·-·-) shows the estimated open-loop CV based on the covariance matrix $\Sigma$. Comparison of the closed-loop and open-loop CV in the output space shows that the cycle-to-cycle fluctuations in the control signal does not amplify the output CV by a large factor. The variability of the actuators however drives the system occasionally where the misfire probability is non-zero. Hence, the implementation of the feedback controller needs to account for misfires.

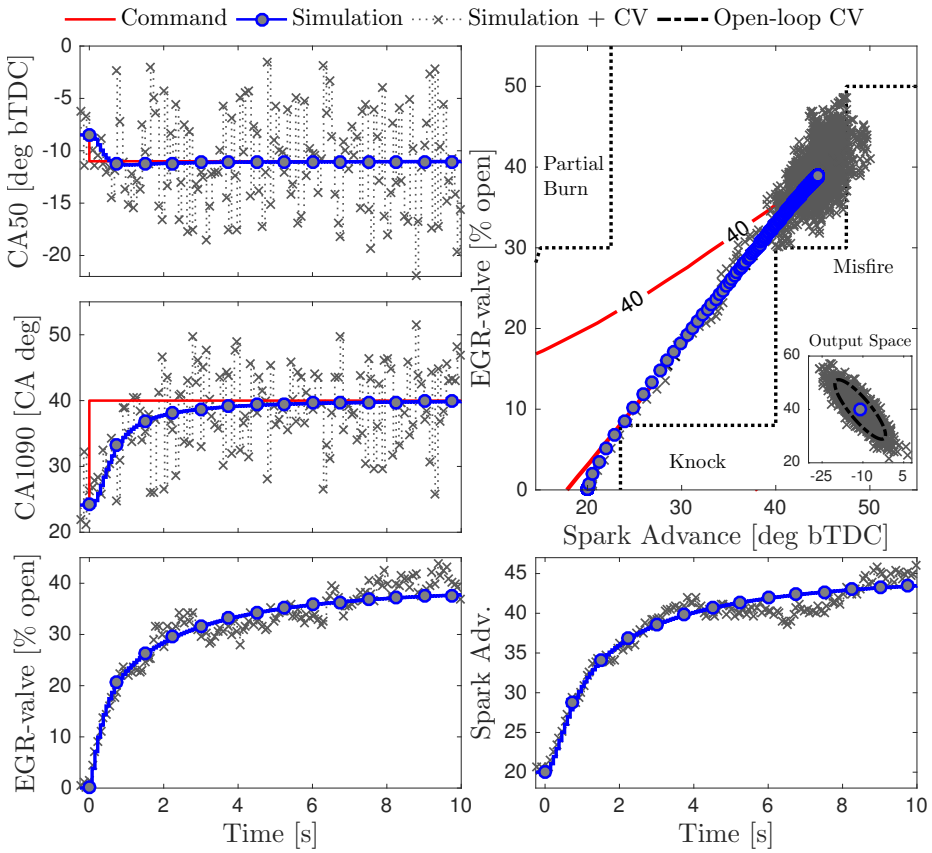


Figure 4.6: Simulated closed-loop system under LQG control during 2000 cycles. Estimated open-loop variability was based on SVD of $\Sigma$ (Eqn (4.3)).

### 4.4.3 Implementation of Feedback Controller

During a misfire event, the feedback loop is effectively broken since CA50 and CA1090 cannot be calculated and the tracking problem could be problematic. For instance, if the default value during misfire is $\text{CA1090}_k = 0$, the controller will generate a control signal to compensate for this change. Thus, misfires should be *masked* so the LQG controller does not respond to these sporadic events. This can be accomplished by the following *misfire masking logic*:

$$\text{CAxx}_k = \begin{cases} \text{CAxx}_k & \text{if No Misfire} \\ \text{CAxx}[k-1] & \text{if Misfire} \end{cases} . \tag{4.13}$$

Figure 4.7 shows the simulated steady state response of the closed-loop system at Point Y. Note that the PDF of inputs and outputs correspond to Gaussian distributions with averages that coincide with the target combustion shape. The estimated misfire probability $\hat{p}_k$ is calculated using the *maximum likelihood* principle

applied to the Bernoulli random variable $Z \sim \text{Ber}(p)$. In other words,

$$Z_k = \begin{cases} 0 & \text{if No Misfire} \\ 1 & \text{if Misfire} \end{cases}, \; \hat{p}_k = \frac{1}{N} \sum_{i=0}^{N-1} Z[k-i] \tag{4.14}$$

where $N = 2000$ is the size of the moving window for estimation. Since SA can rapidly adjust CA50, a tight control of this feature requires a low variability in SA. Note that the standard deviation of SA in closed-loop ($\sigma = 1.9$) is relatively low, which contributes to the low increment in $\sigma_{50}$ from 4.7 (open-loop) to 4.9 (closed-loop). The normality of the distributions also show that the feedback loop is not broken when misfires occur and Eqn. (4.13) do not perturb the LQG commands. Note that for this realization of the random variables CA50, CA1090 and Z, $\hat{p}$ reached a maximum of 0.3%. This occurrence rate can be problematic from the drivability point of view.

The presence of misfire is a concern for implementation on a real engine. Given the similarities in the statistical properties between knock and misfire events, stochastic

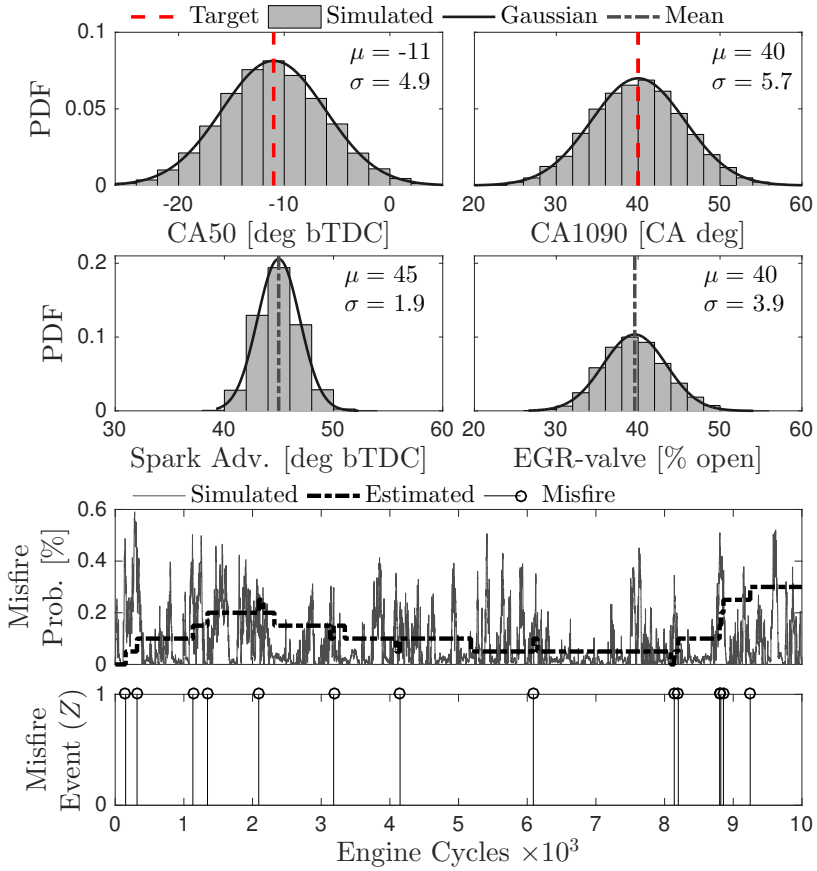


Figure 4.7: Simulated closed-loop system under LQG control at POINT Y during $10^4$ engine cycles. Total number of misfires: 14.

control architectures such as [35, 61, 62] could be implemented to protect the engine. However, this additional *misfire controller* should not create conflicts with the commands issued by the LQG in the closed-loop system.

## 4.5 Summary

Closed-loop control of the combustion process of a spark-ignition, internal combustion engine can be achieved by a coordinated action of SA and EGR valve. When a higher fuel economy is required at a given load, high levels of EGR improve engine efficiency but increase CV. In order to fully characterize the engine operation at this high dilution limit, the statistical properties of the combustion features are required for control design. The LQG controller designed tracks the desired operating condition without amplifying CV by a large factor. The variability introduced in the control signals however could drive the system occasionally to condition with a non-zero misfire probability. Consequently, the closed-loop system should be designed for adequate transient and steady state operation. Simulated results show the potential this control strategy has to ultimately manage the CV at the high dilution limit and operate at steady state without large variability in combustion phasing.

# CHAPTER V

# Cycle-to-cycle Feedback for Combustion Control of Spark Advance at the Misfire Limit

## 5.1 Motivation

Exhaust gas recirculation (EGR) in spark-ignited (SI) internal combustion engines is a well known strategy to improve fuel economy (FE). By lowering the temperature inside the cylinder, the combustion process becomes more resilient to knock and auto-ignition. Pushing the knock limit allows to advance the spark towards maximum brake torque (MBT) and, consequently, obtain a better combustion efficiency and FE. However, as EGR increases, the ignition delay and the combustion duration elongate due to the reduction in flame propagation speed. Occasionally this slow flame may lead to partial burns or misfires, increasing the combustion variability (CV) and deteriorating drivability. Controlling the start and duration of combustion guarantees the operation at high EGR levels while sustaining a healthy flame. However, even though on average the start and duration of combustion are timed to produce the desired combustion process, random misfire events can still occur. A strategy to correct the combustion process is required if the rate of misfire events exceeds a predefined allowable limit, where minimum drivability requirements and emission regulations are violated. This study focuses on the design of a feedback misfire controller to push engine efficiency to the misfire limit, maximizing the use of EGR, while not exceeding a maximum allowable misfire rate to comply with drivability and emission constraints.

Although misfire events are acknowledged as random, no study has formally characterized this process. It is shown that misfire events can be modeled as a Bernoulli random process, similarly to knocking events, based on the distribution of the total number of misfires and the distribution of the number of cycles between each misfire (interarrival time). Under this assumption, a likelihood-based controller is designed

based on a desired misfire probability to retard spark timing to a condition less prone to misfire. The closed-loop system was simulated using a control-oriented combustion model and a random generator for misfire events which obeys the Bernoulli process characteristics. Given the stochasticity of the system response, the closed-loop performance is evaluated by the probability distribution of the combustion features. The results were compared to a more conventional control strategy where spark retards every time a misfire is detected. Comparison of the steady state distribution of combustion features shows that the likelihood-based controller has a more compact distribution closer to the misfire limit, while the conventional controller has a wider distribution that contributes to cycle-to-cycle variability in the combustion process.

## 5.2 Combustion at the Misfire Limit

The data presented in this study was collected the same engine as Section 2.2. Engine operating conditions are Points X and Y described in Table 4.1. Figure 5.1 shows the combustion characteristics of two operating conditions, Point X without EGR and Point Y with EGR. Although CA1090 is elongated and CA50 is retarded at Point Y, the break specific fuel consumption (BSFC) is reduced by 1.9%, reflecting the fuel economy improvement. Points X and Y, in average, have similar IMEP values. However, EGR reduces pumping losses that decreases the pumping mean effective pressure (PMEP). Thus, according to the equation

$$\text{NMEP} = \text{IMEP} - \text{PMEP} \tag{5.1}$$

the net mean effective pressure (NMEP) at Point Y is higher. The pressure and fuel mass fraction burned (MFB) traces, as well as the standard deviation of combustion features, indicate how the combustion variability is increased in Point Y. Note that the distribution of CA50 over 2000 engine cycles follows a normal distribution (similarly for CA10 and CA1090). Hence, it is assumed the parameters of the normal distribution vary continuously as SA/EGR valve conditions change.

### 5.2.1 On-board Diagnostics

On-board diagnostics (OBD) in commercial vehicles alert the driver when a component is failing. The *misfire detection monitor* is in charge to continuously detect if the engine is operating at misfire conditions. The most cost-effective approach for misfire detection uses engine crankshaft speed information to determine if a certain

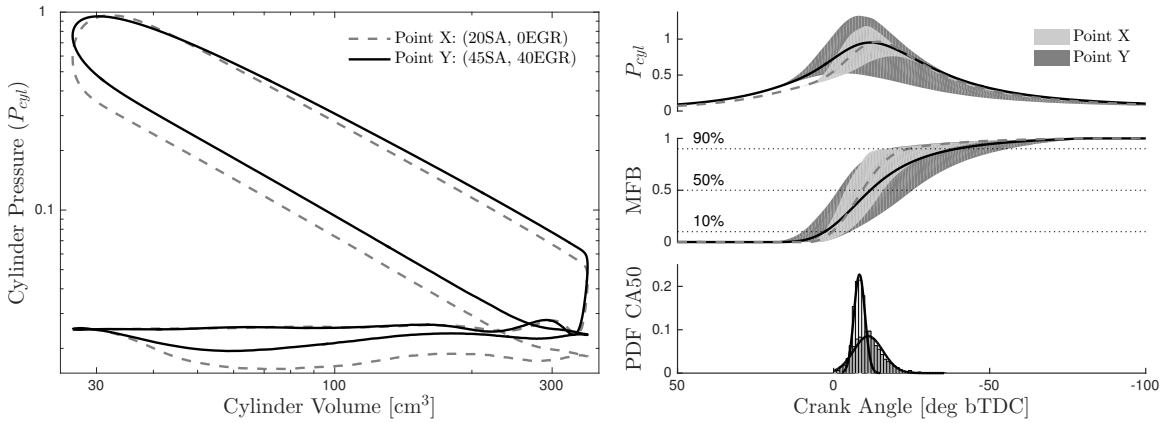


Figure 5.1: Normalized P-V diagram for two operating conditions (POINT X and POINT Y). Normalized cylinder pressure ($P_{\text{cyl}}$), fuel mass fraction burned (MFB), and probability density function (PDF) of CA50 are plotted as function of CA deg. Grey colored region represents 2000 engine cycles.

cylinder has misfired. Since factors such as cold start, rough roads and sudden throttle opening (blip) also cause variability in crankshaft speed, the detection algorithm is quite involved and occupies a significant space in the OBD-II software [63]. There are two emission-related type of faults that will trigger a *malfunction indicator light* (MIL) in the dashboard:

- **Type A**: Misfires that can overheat and damage the catalyst.
- **Type B**: Misfires that can cause an increase of exhaust emissions exceeding 1.5 times the standard.

According to [64], the misfire rate that causes catalyst damage is speed/load dependent, ranging from 5% to 25%. However, only a misfire rate of 2% is necessary to raise emission levels over the threshold defined in OBD-II [24, 64].

Drivability is another important factor when dealing with diluted combustion. The coefficient of variation of IMEP ($\text{CoV}_{\text{IMEP}}$) is widely used as a metric of CV. Table 5.1 shows the $\text{CoV}_{\text{IMEP}}$ values of all SA/EGR operating conditions together with the percentage of misfire cycles. In order to achieve the conditions with high $\text{CoV}_{\text{IMEP}}$, it was necessary to overwrite the production maps and manually modify spark advance and EGR valve. Kuroda et. al. performed similar experiments in [13] at the same speed/load condition. They concluded that for $\text{CoV}_{\text{IMEP}} > 10\%$, torque fluctuations are high enough to jeopardize drivability (*stability limit*). Note that POINT Y in Table 5.1 is right at the stability limit. Increasing SA or EGR valve opening will deteriorate the combustion process and cause occasional misfires, increasing $\text{CoV}_{\text{IMEP}}$.

Table 5.1: Coefficient of Variation of IMEP in percentage ($CoV_{IMEP}$ [%]) together with misfire rate at 60% EGR valve opening.

| EGR | Spark Advance [deg bTDC] | | | | | | | | |
|---|---|---|---|---|---|---|---|---|---|
| valve | 10 | 15 | 20 | 25 | 30 | 35 | 40 | 45 | 50 |
| 0% | 1.6 | 1.0 | **0.6** | KNOCK | | | | | |
| 20% | | 5.9 | 4.2 | 3.3 | 2.2 | 1.7 | | MISFIRE | |
| 40% | | | | 9.1 | 8.1 | 7.0 | 5.2 | **5.2** | \| |
| 60% | | PARTIAL | | 12.1 | 9.0 | 8.4 | 7.9 | 9.0 | \| 16.3 |
| | | BURN | | – | – | – | – | 0.2% | \| 0.6% |

– – –: Misfire limit

Figure 5.2 shows the normalized IMEP during a period of 2000 engine cycles for POINTS X, Y, and a point over the stability limit. POINT X shows minimum CoV since exhaust gases are not present in the combustion chamber and SA is at MBT. In contrast, POINT Y shows an increase in CV, mainly due to slow burning cycles. The third point shows a dramatic increase in combustion variability due to a high number of partial burns and sporadic misfires (IMEP $< 0$). Therefore, the misfire limit in this study is defined at 0.2% misfire rate to maintain $CoV_{IMEP} < 10\%$. Since $0.2\% < 2\%$, operating close to this limit will not trigger the MIL in the dashboard. After modeling the combustion process, a model for misfire event generation is required for simulating the combustion process at the misfire limit.

## 5.3 Misfire Event as a Random Variable

Although the randomness of misfire events is widely acknowledged, no formal study has been done to determine the distribution from which misfires emerge. Statistical tools have been developed for detection relaying on the randomness of variables related to misfires, such as torque fluctuations [65], but a stochastic control-oriented model requires the knowledge of the random behavior of the variable under control.

### 5.3.1 Misfires and the Bernoulli Process

Let $\{X_n\}$ be a stochastic process where $X_i = \{0, 1\}, \forall i \in \{1, \ldots, n\}$. For this study, $n$ is the number of engine cycles and 0 = 'No Misfire', 1 = 'Misfire'. Let $p$ be the probability that a misfire event occurs in a given cycle. Then, $X_i \sim \text{Ber}(p)$. Moreover, if $\{X_n\}$ is a sequence of independent random variables (RV), then they

describe a *Bernoulli random process*. In order to prove that the misfire events can be modeled as independent RV, two necessary conditions from the Bernoulli process are tested:

1. Let $K = \sum_{i=1}^{n} X_i$ (number of misfires in $n$ engine cycles), then $K \sim \text{Binom}(n, p)$
2. Let $Y_k = \min\{n \mid K = k\}$ for $k \geqslant 1$ (arrival time of the $k^{\text{th}}$ misfire). Define $Y_0 = 0$, then $T_k = Y_k - Y_{k-1}$ is the $k^{\text{th}}$ *interarrival time*. Moreover, $T_k \sim \text{geom}(p)$.

Following the frequentist inference, the maximum likelihood estimator of $p$ is calculated as follows:

$$p_{\text{est}} = \frac{1}{n}\sum_{i=i}^{n} X_i = \frac{k}{n}, \qquad X_i \in \{0, 1\} \tag{5.2}$$

A total of $n = 150,000$ engine cycles were recorded at the operating condition SA = 55 [deg bTDC] and EGR valve = 45 [% open] (over the misfire limit). Figure 5.3 shows the comparison between the probability mass functions (PMFs) of the experimental distribution of interarrival times $T_k$ and the theoretical geometric distribution with parameter $p_{\text{est}}$. It is clear that the hypothesis of $T_k \overset{iid}{\sim} \text{geom}(p_{\text{est}})$ is satisfied.

If $X_i \overset{iid}{\sim} \text{Ber}(p)$, then the *stationarity* property indicates that partitioning $n$ cycles into $m$ samples generates sets $S_1, \ldots, S_m$ of Bernoulli RVs with the same distribution.

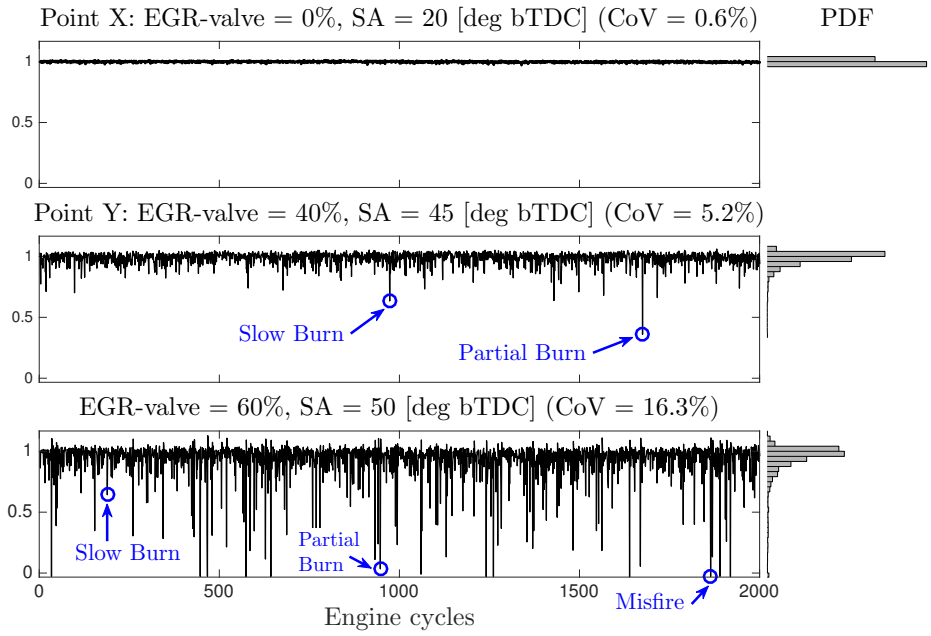


Figure 5.2: Variability or normalized IMEP at Point X, Point Y and condition EGR valve = 60% open, SA = 50 [deg bTDC] (over the stability limit).

Note that the number of cycles in each of the $m$ samples is $n/m$. Then,

$$K_m = \sum_{j=1}^{n/m} X_j, \;\; X_j \in S_m \implies K_m \sim \text{Binom}(n/m, p_{\text{est}}). \tag{5.3}$$

Note that if $n$ and $p_{\text{est}}$ are fixed, then the distribution of $K_m$ changes with $m$. Figure 5.4 shows the distribution of the number of misfires $K_m$ for $m = 150$. The comparison of the experimental data at SA = 55 [deg bTDC] and EGR valve = 45 [% open] with the theoretical binomial distribution with parameters $(n/m, p_{\text{est}})$ confirms the hypothesis that $K_m \sim \text{Binom}(n/m, p_{\text{est}})$.

Therefore, by satisfying these conditions, we conclude that misfire events can be modeled as a stochastic Bernoulli process with parameter $p_{\text{est}}$. Note that at each operating condition in Table 5.1, $p_{\text{est}}$ = 'No. of misfires'/2000 is the estimated *misfire probability*, which is equivalent to the misfire rate previously mentioned. With this information, a stochastic misfire controller can be designed to control the misfire probability to a target value lower than the misfire limit.

## 5.4 Likelihood-based Controller

Given the similarities between the distributions from which knock and misfires are drawn, stochastic control architectures such as [20,59,66] could be implemented in the misfire case. The likelihood-based controller developed in [61] has been considered for the misfire control case since the final distribution of the control command is

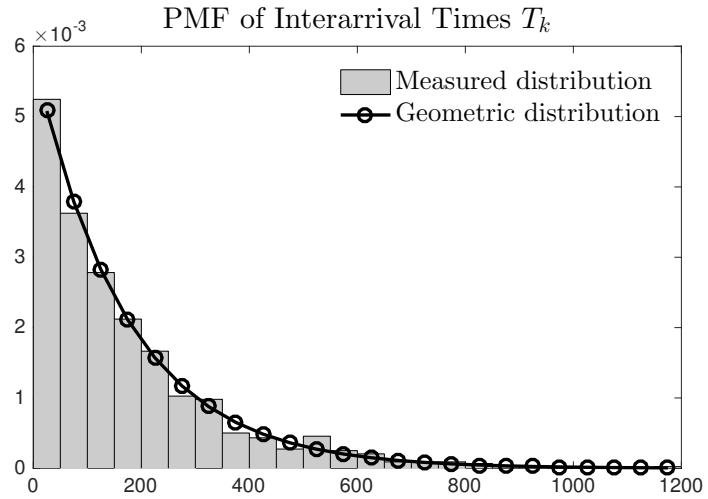


Figure 5.3: Probability mass function (PMF) of interarrival times between misfires in $n = 150,000$ engine cycles. SA = 55 [deg bTDC], EGR valve = 45 [% open].

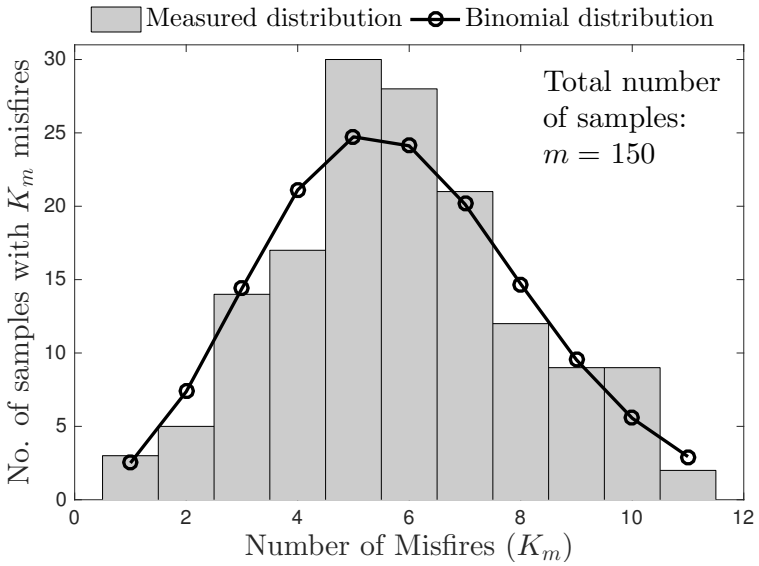


Figure 5.4: Distribution of the number of samples containing exactly $K_m$ misfires for $m = 150$ samples extracted from the data set with 150,000 engine cycles. SA = 55 [deg bTDC], EGR valve = 45 [% open].

concentrated closed to the mean (less cycle-to-cycle CV).

The likelihood ratio for a binomial random variable is defined as follows:

$$L_n(k) = \frac{p_{\text{des}}^k \left(1 - p_{\text{des}}\right)^{n-k}}{p_{\text{est}}^k \left(1 - p_{\text{est}}\right)^{n-k}} \tag{5.4}$$

where $p_{\text{des}}$ is the desired or *allowable* misfire probability. Considering that the misfire limit occurs at $p_{\text{est}} = 0.2\%$, the allowable misfire rate was set to $p_{\text{des}} = 0.1\%$. As dis-

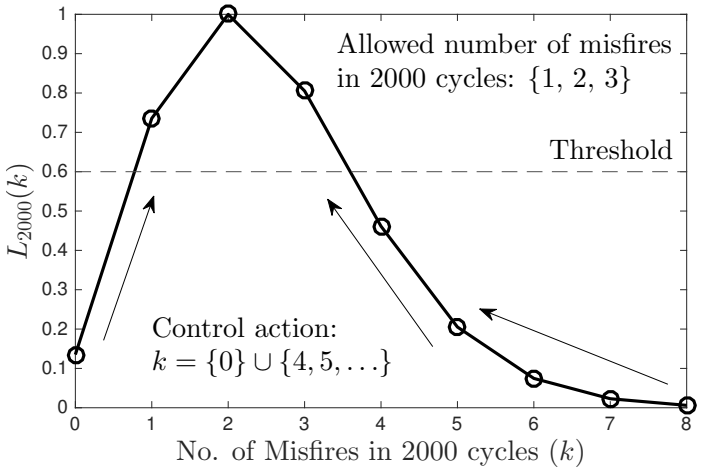


Figure 5.5: Likelihood ratio $L_n(k)$ with a fixed moving average window $n = 2000$ and threshold $L_{\text{th}} = 0.6$.

cussed in [61,67], if $n$ is free and increases unbounded in a Key ON/Engine Run/Key OFF cycle, then $p_{\text{est}}$ becomes insensitive to changes in $k = \sum X_i$. In other words, as $n \to \infty, p_{\text{est}} = k/n$ filters out changes in $X_i$. This behavior is undesirable if the engine experiences a sequence of misfire events with small interarrival times. If $n$ is large, this (locally) abrupt change will not be captured by $p_{\text{est}}$. In this study, $n$ will be a moving window with fixed size.

The *fresh-start* property of a Bernoulli process states that for any $i \in \mathbb{N}$, the sequence of RVs $\{X_{i+1}, \ldots, X_{i+n}\}$ is also a Bernoulli process with parameter $p$. Note that any time the window moves and calculates $p_{\text{est}}$, the distribution of misfires will not be altered. Hence, $p_{\text{est}}$ can be seen as a *moving average* of the variable $X_i$ (Eq. 5.2). For accuracy in the calculation of $p_{\text{est}}$, the window size was set to $n = 2000$ engine cycles. A threshold $L_{\text{th}}$ for the likelihood ratio determines the values of $k$ that will trigger a control action. Figure 5.5 shows $L_n(k)$ for $n = 2000$. Note that if $k = \{1, 2, 3\}$ misfires are detected in the window, $L_{2000}(k) > 0.7$. Moreover, the rates associated with each $k$ are $p_{\text{est}} = \{0.05\%, 0.10\%, 0.15\%\}$ respectively, which are considered allowable and no control action is taken. On the other hand, when $L_{2000}(k) < 0.5$ two possible control actions occur:

- $\mathbf{k = 0}$: The operating condition is consider *'conservative'* with respect to $p_{\text{des}}$. The controller will force the engine to operate closer to $p_{\text{des}}$.

- $\mathbf{k \geqslant 4}$: The misfire rate is too high with respect to $p_{\text{des}}$. The controller will move away from conditions with misfire rates $p_{\text{est}} \geqslant 0.2\%$.

Hence, the threshold $L_{\text{th}} = 0.6$ was used for simulations. Figure 5.6 shows the block diagram of the closed-loop system with the misfire controller in place. Knowledge of the control architecture allows for gain tuning and simulation.

### 5.4.1 Gain Tuning

The likelihood-based misfire controller has the following control law:

$$\text{SA}[i] = \begin{cases} \text{SA}[i\text{–}1] & \text{, if } L_n(k) \geqslant L_{\text{th}} \\ \text{SA}[i\text{–}1] + K(1 - L_n(k)) & \text{, if } L_n(k) < L_{\text{th}} \end{cases} \tag{5.5}$$

$$\text{where: } K = \begin{cases} K_{\text{advance}} & \text{, if } p_{\text{est}} < p_{\text{des}} \\ -K_{\text{retard}} & \text{, if } p_{\text{est}} > p_{\text{des}} \end{cases} . \tag{5.6}$$

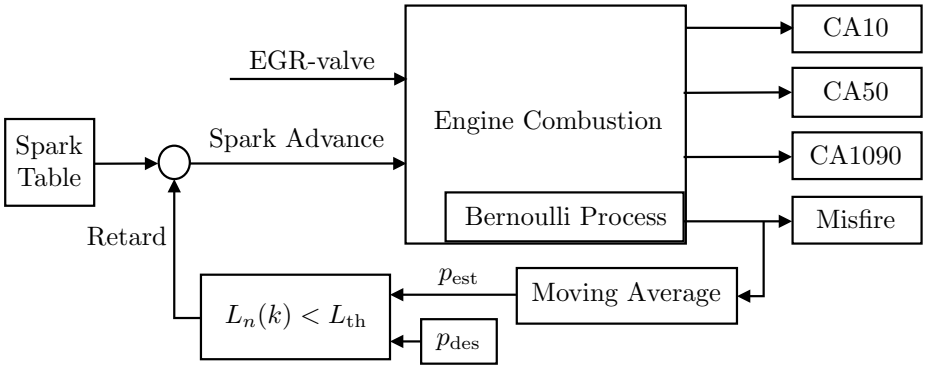


Figure 5.6: Block diagram of the closed-loop system with the likelihood-based misfire feedback controller.

Since only spark retard is needed for misfire prevention, $K_{\text{advance}} = 0$. Also note that the retarding action of the controller is proportional to $1 - L_n(k)$, which means that

$$0 < \text{SA}[i-1] - \text{SA}[i] < K_{\text{retard}}, \quad \text{when} \quad p_{\text{est}} > p_{\text{des}}. \tag{5.7}$$

According to Table 2.2, it suffices to move SA from 45 to 40 [deg bTDC] at 40% EGR valve opening to avoid a high misfire rate. Hence, for a fast reaction under a sudden increase in misfire rate, $K_{\text{retard}} = 5$.

For verification purposes, suppose that the misfire limit *drifts* towards a more retarded SA condition. The closed-loop system will respond to a high misfire rate by shifting the spark to a retarded position, by maintaining the open-loop EGR valve position.

## 5.5 Closed-loop Response

Suppose that over time the operating conditions change and the misfire limit drifts towards Point Y, then the misfire controller should reduce the misfire rate and protect the engine. Figure 5.7 shows the simulation of the closed-loop system when the misfire controller is in place. Note that as the misfire probability increases, and the estimated misfire probability gets over the allowable limit, spark advance is retarded from the original value at Point Y, causing CA10 to retard as well. As CA10 retards due to the control action, CA50 also retards. On the other hand, the EGR valve still has its open-loop value and CA1090 increases as CA10 retards. Since the CA50 value retards by at most 2 [CA deg] and CA1090 increases by at most 1.5 [CA deg], we expect that the average fuel efficiency is still superior than Point X.

Since $K_{\text{advance}} = 0$, spark advance never exceeds its original value at Point Y.

Nevertheless, the misfire controller has the potential to push the engine to the misfire limit if the open-loop value of SA is conservative. Ideally, the spark table should provide the ideal condition for fuel economy, if not, a small $K_{\text{advance}}$ gain could push the engine to a higher efficiency condition. In order to compare the performance of the likelihood-based controller with a more familiar case, we consider the application of the *conventional* knock controller for the misfire case [23].

### 5.5.1 Comparison with a Conventional Event-driven Controller for Misfire Prevention

Consider the conventional feedback control for sporadic misfire events that increases slowly SA but abruptly retards its timing any time a misfire is detected:

$$\text{SA}[i] = \text{SA}[i-1] + K_{\text{advance}} - K_{\text{retard}} \times \mathbb{1}_{\text{Misfire}} \tag{5.8}$$

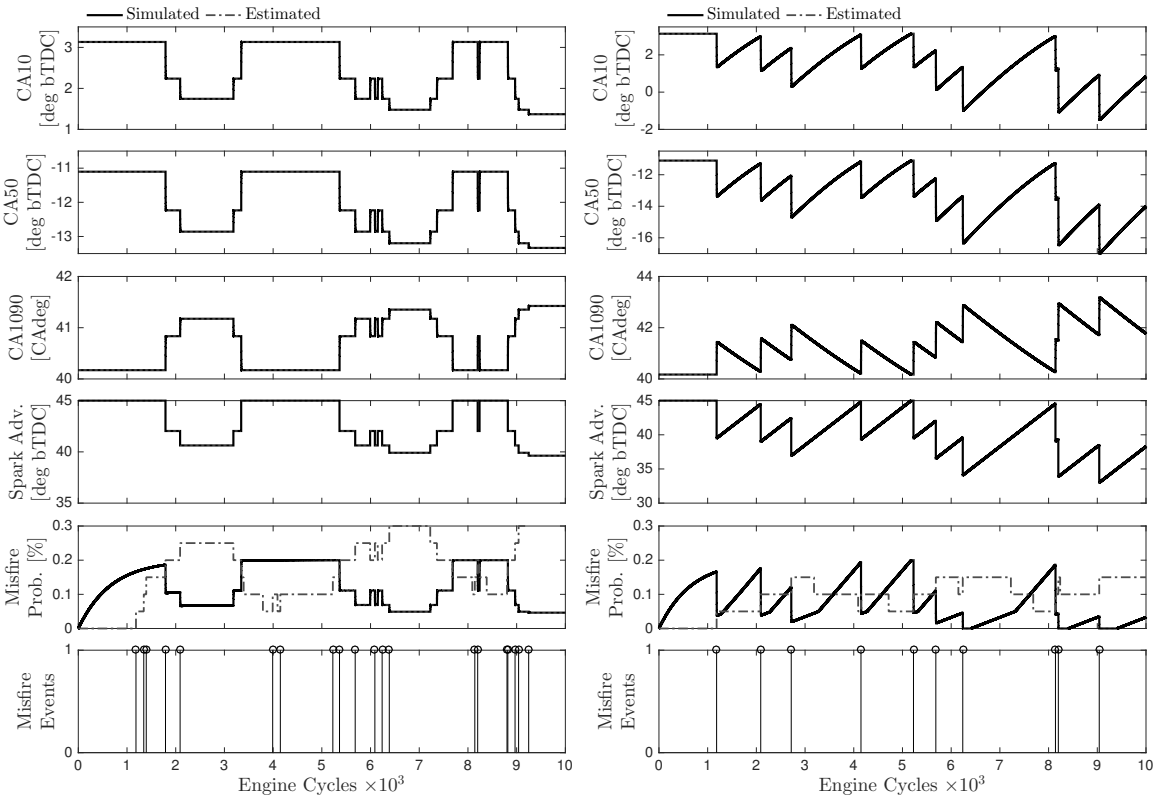


Figure 5.7: Closed-loop response of misfire controller at POINT Y. Left: Likelihood-based, Right: Conventional.

where $\mathbb{1}_{\text{Misfire}}$ is an indicator function for misfire events. In order to maintain the desired misfire probability $p_{\text{des}}$, the feedback gains must satisfy the relation:

$$K_{\text{advance}} = \frac{p_{\text{des}}}{1 - p_{\text{des}}} K_{\text{retard}}. \tag{5.9}$$

Moreover, since the controller should not exceed the value of SA at POINT Y, the feedback compensation must be only negative:

$$K_{\text{advance}} - K_{\text{retard}} \times \mathbb{1}_{\text{Misfire}} \leqslant 0. \tag{5.10}$$

Note that this is equivalent to the restriction $K_{\text{advance}} = 0$ for the likelihood-based controller. Figure 5.7 shows the closed-loop response of the system using the conventional strategy of retarding SA using $K_{\text{retard}} = 5$. Note the typical saw-tooth profile for the commands and the combustion features. The range of CA10, CA50 and CA1090 values has increased with respect to the likelihood-based controller. Due to the slow rate at which SA advances towards the desired value at POINT Y, the closed-loop system spends most of the time operating in sub-optimal conditions.

Figure 5.8 shows the PDF of CA10 and CA1090 when the system operates at POINT Y after simulation of $10^6$ engine cycles. Both control strategies for retarding SA are compared, assuming that the distribution depicted in Fig. 5.8 is closed to the steady state distribution. The likelihood-based controller locates the mean values of CA10 and CA1090 closer to the desired values at POINT Y. The conventional controller on the other hand locates the mean value of CA10 in a more retarded

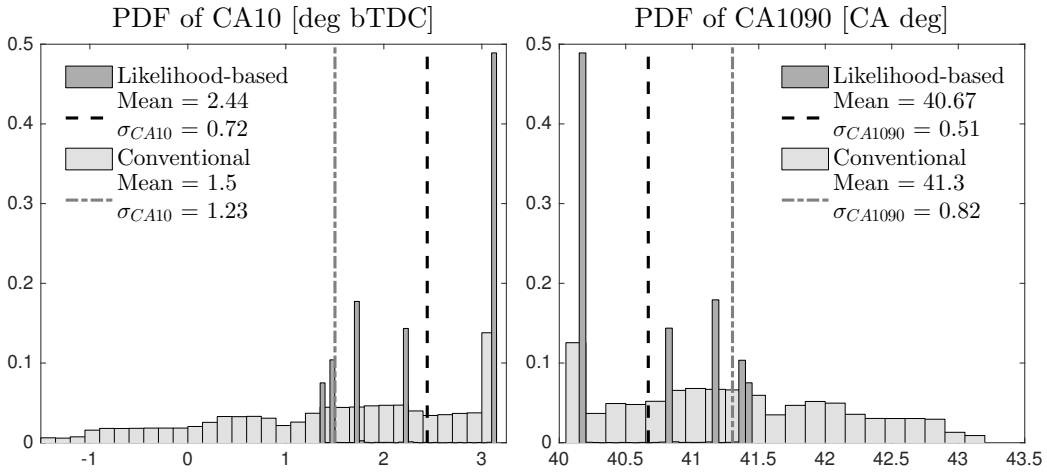


Figure 5.8: PDF of CA10 and CA1090 at closed-loop operation for the likelihood-based and the conventional misfire controller.

timing and the mean of CA1090 in a more elongated duration. The likelihood-based controller is more likely to hold the values of CA10 and CA1090 at POINT Y for longer time, resulting in an overall higher fuel efficiency. Note also the wider distribution that the conventional controller generates in the combustion features. This wider distribution combined with the combustion variability of CA10 and CA1090 could increase the probability of partial burns and/or misfires, increasing $\mathrm{CoV}_{\mathrm{IMEP}}$ and jeopardizing drivability.

## 5.6 Summary

A likelihood-based misfire controller has been designed to operate the engine close to the misfire limit. Due to the combustion variability present in the system with high EGR levels, the misfire controller monitors the operation of the engine and commands a retarded condition when the misfire rate is higher than the allowable. In order to assess the closed-loop behavior with simulations, a simple model for the combustion process and a stochastic model for the misfire event generation are discussed. The feedback gains chosen guarantee a fast reaction to high misfire rate regions. Comparison with a conventional feedback controller for misfire events shows that the likelihood-based approach reduces cycle-to-cycle variability in the closed-loop operation.

# CHAPTER VI

# Non-Equiprobable Statistical Analysis of Misfires and Partial Burns for Cycle-to-Cycle Control of Combustion Variability

## 6.1 Motivation

A new methodology is proposed for understanding the cycle-to-cycle variability of the combustion process at the tipping point where high EGR levels suddenly trigger sporadic misfires. The indicated mean effective pressure (IMEP) was used as the cyclic parameter for categorizing combustion cycles into 1) high energy, 2) nominal, 3) partial burns, and 4) misfires. Thresholds for IMEP based on return maps are suggested for cycle classification. Deterministic patterns, similar to those discussed by Daw et al. in [68] for the lean case and Finney et al. [69] for the EGR case, mainly involved misfires followed by high energy cycles due to the extra oxygen and fuel present at the intake stroke inside the cylinder immediately after a misfire. However, this paper suggests that previous cycles do not have a major influence on the occurrence of misfires and partial burns, making them random in nature. Furthermore, a multinomial distribution can be used to describe the joint distribution of partial burns and misfires.

It is demonstrated that observation of partial burns can increase the probability of observing a misfire when the conditional probability is used as the metric. Based on these findings, future work will be able to use the observation of partial burns alone to control the upper bound on the probability of misfire events. To this end, different metrics are proposed to control directly and indirectly the probability of misfires, and their advantages and disadvantages for feedback combustion control are discussed.

## 6.2 Combustion Variability at Different EGR Levels

As EGR levels increase, the laminar flame burning velocity decreases and combustion duration elongates. In particular, the initial flame development period is highly susceptible to charge homogeneity, charge dilution, and turbulence intensity [6, 12]. A physics-based model for flame burning velocity under high EGR levels at this early stage was developed by [15] in order to understand and extend the benefits of diluted combustion. The effect of EGR on combustion kinetics changes the combustion phasing due to the elongated combustion duration. Spark advance is then required to increase in order to achieve maximum break torque (MBT). Table 6.1 shows three different spark/EGR valve combinations at the same engine speed and load. The EGR-rate, defined as the percentage of exhaust gas respect to total cylinder mass, was obtained from the estimation algorithm in the stock engine control unit (ECU). Point X is a condition without EGR dilution and MBT spark. Point Y is a condition with approximately 20% EGR rate and spark advance at the MBT. Note that, as previously discussed, EGR dilution reduces break specific fuel consumption (BSFC) at the cost of a more advanced spark timing and a significant increase in cyclic combustion variability, quantified by the coefficient of variation (CoV) of IMEP. Point Z is a condition with the maximum amount of EGR-rate (25%) at the same engine load. The spark has been over-advanced to cause sporadic misfires, which are captured by the drastic increase in $\text{CoV}_{\text{IMEP}}$.

Figure 6.1 shows the return map of the normalized IMEP for Points X, Y, and Z. In such plot, cycle $k+1$ is a function of cycle $k$ in order to capture deterministic correlation between consecutive cycles. The resulting map for Point X consists of a disk centered at the nominal value, which reflects the randomness of the combustion process. The return plot for Point Y is no longer circular but stretches to a "Delta"

Table 6.1: Engine operating conditions with similar indicated mean effective pressure (IMEP) and different EGR levels.

| | **Point X** | **Point Y** | **Point Z** |
|---|---|---|---|
| Spark Adv. [deg bTDC] | 20 | 45 | 50 |
| EGR valve [% open] | 0 | 40 | 60 |
| EGR rate (ECU est.) [%] | 0 | 20 | 25 |
| $\text{CoV}_{\text{IMEP}}$ [%] | 0.60 | 5.24 | 16.33 |
| BSFC [g/kWh] | 258.8 | 253.8 | 278.4 |

shape that reflects an increasing tendency to cycles with lower energy release. As discussed in [70], the presence of EGR decreases combustion efficiency due to its effect on flame kinetics, generating incomplete combustion cycles. However, the maps for POINTS X and Y are symmetric with respect to the 45° diagonal, indicating no major cyclic deterministic behavior between consecutive cycles. On the other hand, POINT Z presents a clear asymmetry with respect to the diagonal, indicating prior-cycle determinism. At the high EGR levels and high spark advance of POINT Z, the return map present "arms" that extend all the way to the misfire zone, where IMEP $< 0$. This phenomenon is due to the sensitivity of the flame kernel development at the *misfire limit* with respect to mixture composition, as observed initially by Quader in [58] and further modeled by Daw et al. in [68] and Ayala et al. in [71].

Figure 6.2 shows the autocorrelation function $R(m)$ of IMEP for 2000 engine cycles recorded at POINTS X, Y and Z, where $m$ denotes the number of cycle lags for the delayed signal. Note that if $m = 0$ then $R(m) = 1$, which explains why Figure 6.2 shows $R(m)$ for $m > 0$. Recall that if the measurements $\{\text{IMEP}_{[1]}, \ldots, \text{IMEP}_{[N]}\}$ are independent random variables (white noise), the normalized standard error (SE) of

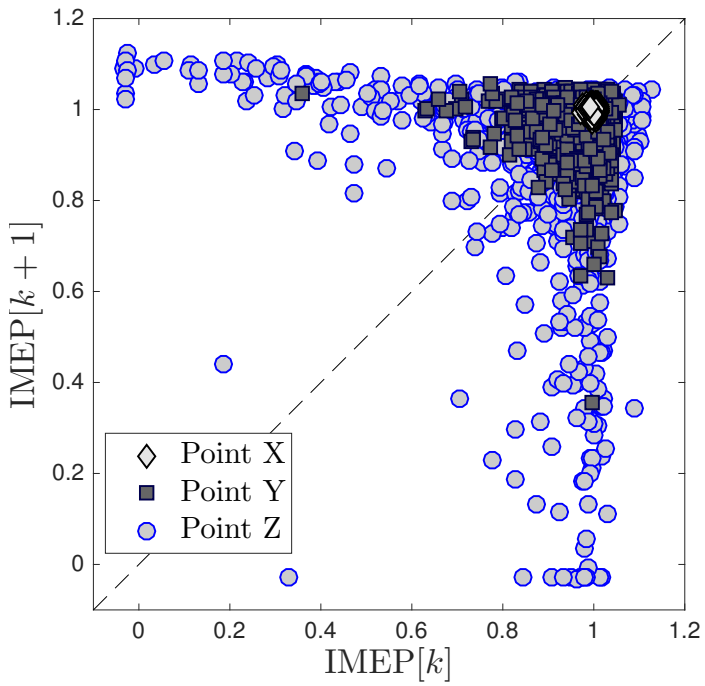


Figure 6.1: Return maps of normalized IMEP for different Spark/EGR valve combinations producing similar net output torque.

the sample mean can be estimated as:

$$\mathrm{SE} = \frac{1}{\sqrt{\mathrm{Var}[\mathrm{IMEP}]}} \sqrt{\mathrm{Var}\left(\frac{\sum \mathrm{IMEP}_{[i]}}{N}\right)} = \frac{1}{\sqrt{N}} \tag{6.1}$$

where Var[·] denotes the variance operator. If one wants to determine if the time series behaves as a white noise process with 95% confidence, the corresponding SE equals $2/\sqrt{N}$. This bound is represented in Figure 6.2 by the solid line and it is assumed that the coefficients falling between such bounds are equivalent to zero. Similar to Figure 6.1, the autocorrelation function for Point X shows no cyclic correlation, and hence no deterministic patterns. One can see the increasing trend on the value of $R(1)$ as EGR levels increases. For $m > 1$ however, $R(m)$ seems to stay close to zero. This observation suggests that cycle $k+1$ will feel *only* the effects of the combustion characteristics of cycle $k$, while cycles $k-m$ for $m \geqslant 1$ will have no significant effect on cycle $k+1$. This apparent cycle dependence has been used by Wagner et al. in [72] for the lean case to derive non-linear dynamic equations that relate cycle $k+1$ with cycle $k$. We will use a similar technique to study the deterministic component of cyclic CV at the misfire limit. Previously, Kaul et al. in [73] showed that, at high enough levels of dilution, the EGR loop induces periodic patterns alternating between high-energy and low-energy cycles. This periodic behavior, with a period in the order of tens of cycles, was achieved with EGR levels above 30% where the occurrence of

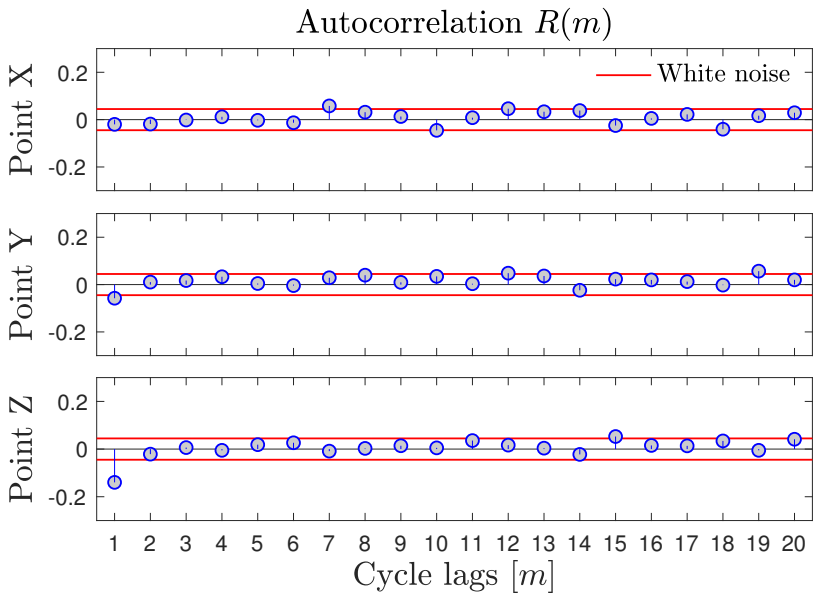


Figure 6.2: Autocorrelation function for samples of 2000 engine cycles recorded in steady state at Points X, Y and Z.

misfires is very frequent. Since our study focuses on the diluted combustion process at the edge of stability, such periodic patterns have not been identified. Hence, we assume that prior-cycle correlation is the major contributor to deterministic CV.

## 6.3 Deterministic Patterns of Cycle-to-Cycle Combustion Variability at the Misfire Limit

Based on the observations in Section 6.2, assume that the deterministic component of cyclic CV can be modeled as follows:

$$\mathrm{IMEP}_{k+1} = f\left(\mathrm{IMEP}_k\right) \tag{6.2}$$

where $f$ is a non-linear function. Moreover, analogous to the analysis done by Finney et al. in [74] to identify deterministic patterns in time series with noisy data, we will categorize the combustion cycles into four groups: 1) nominal cycles (N), 2) partial burns (P), 3) misfires (M), and 4) high energy cycles (H).

### 6.3.1 Equiprobable Classification of Cycles

Following the methodology in Kaul et al. in [3], we classified combustion cycles in binary symbols: "1" = above nominal IMEP, and "0" = below nominal IMEP. According to their study, deterministic patterns could be observed when the symbols are arranged in sequences of 6. In particular, sequences of alternating high-low cycles (1-0-1-0-1-0 and 0-1-0-1-0-1) were clearly occurring with a frequency higher than random sequences. Figure 6.3 shows the sequence frequency histogram of such cycles classified into binary symbols for the study performed in [3] (top) and Points Y and Z used in this study (bottom). The solid line represents the expected uniform probability mass function (PMF) when all possible outcomes are equiprobable: $Pr(X) = 1/2^6$. Note that, form the plot extracted from [3], the $\mathrm{CoV}_{\mathrm{IMEP}}$ is much larger than 16% and the corresponding probabilities of alternating high-low sequences (1-0-1-0-1-0 and 0-1-0-1-0-1) are above 5%. For our study, at 5.2% $\mathrm{CoV}_{\mathrm{IMEP}}$, where no misfires were reported, the PMF is close to a uniform distribution. At 16.3% $\mathrm{CoV}_{\mathrm{IMEP}}$, where misfires occur sporadically, a small peak appears around the sequence 0-1-0-1-0-1. However, the magnitude is not large enough to suggest a strong determinism.

Therefore, the equiprobable binary classification method is not useful to discern deterministic patterns at the *ragged edge* of combustion stability where partial burns and misfires occur with a very low occurrence rate.

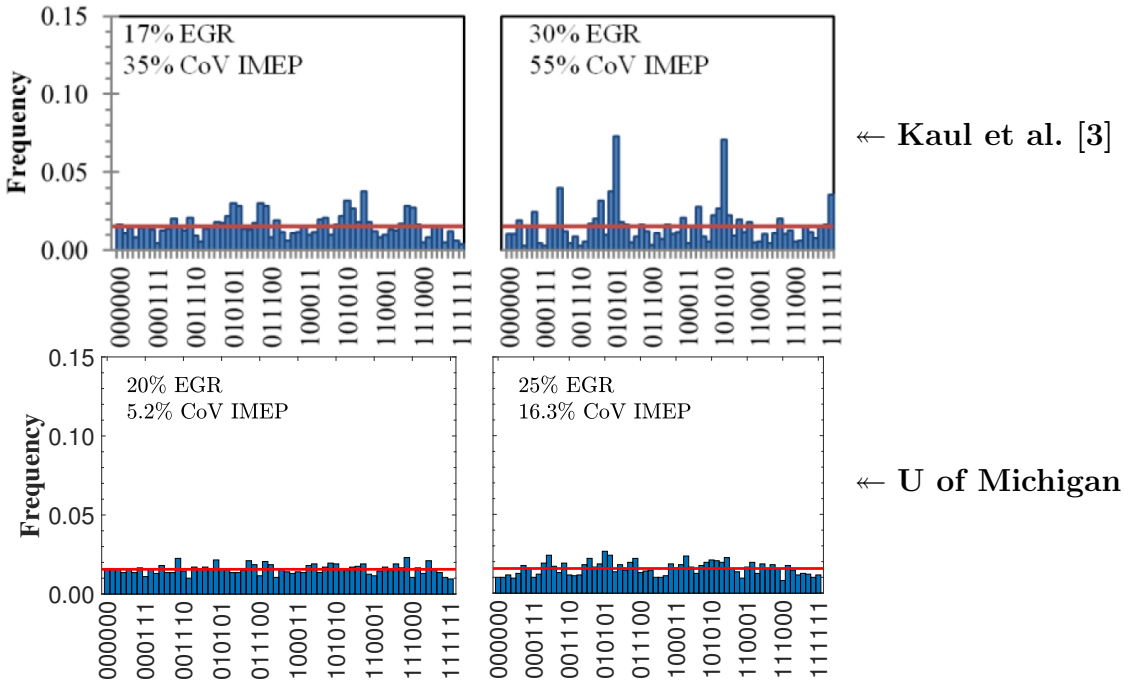


Figure 6.3: Sequence frequency histogram for sequences of 6 equiprobable binary symbols for data reported in [3] (top) and University of Michigan data recorded at Point Y (bottom left) and Z (bottom right).

### 6.3.2 Non-equiprobable Classification of Cycles

The autocorrelation function in Figure 6.2 suggests that there is no serial correlation between the delayed signals $\{\text{IMEP}_k\}$ and $\{\text{IMEP}_{k+2}\}$. This remark also suggests that if either abnormal cycle P,M, or H occur at instance $k$, then the dynamic system will adjust itself and return to the nominal value N by cycle $k+2$. Such observations can be used to determine upper and lower bounds for nominal combustion cycles N.

To infer statistical properties with a high confidence level, 150,000 steady state measurements were taken at spark advance of 55 [deg bTDC] and 45% EGR valve opening. Figure 6.4 shows the return map of the normalized IMEP for signals with 2 cycles delay. As expected, the data points look symmetric with respect to the 45° diagonal clustered around IMEP = 1. The *nominal band* (indicated by the shaded region) was chosen such that more than 99% of the data is contained within. We assume that the scattered points outside the bands are due to random noise. In this case, the nominal value falls between the bounds: $87\% < \mathsf{N} < 107\%$. Note that the interval for N is not symmetric around 1 since at these EGR levels combustion efficiency is reduced and the likelihood of having lower than nominal energy release increases. Hence, the following IMEP bounds define the 4 combustion cycle categories

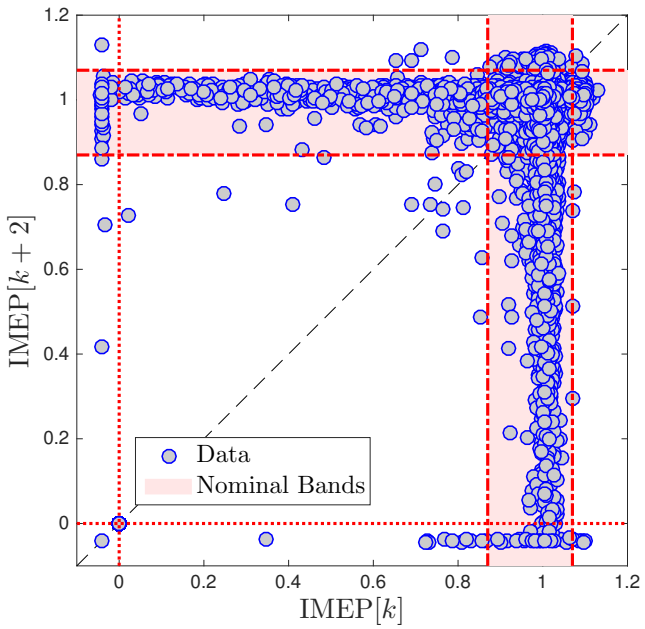


Figure 6.4: Return map of normalized IMEP for a sample of 150,000 engine cycles with a cycle lag of $m = 2$.

used in this study:

$$\mathsf{M} \leqslant 0 < \mathsf{P} \leqslant 87\% < \mathsf{N} < 107\% \leqslant \mathsf{H}. \tag{6.3}$$

This classification differs from the one proposed by Heywood in [18, Chap. 9] in the number of combustion categories. Here, we add the new category H and combine slow-burn cycles and partial-burn cycles into the category P. The later sections will show that this new grouping will result in a simple probabilistic model for combustion events, based only on three categories.

For better visualization of the new combustion cycle categories, the left plot of Figure 6.5 shows the time evolution of the normalized IMEP at Point Z. Note immediately that the discrete bins $\{\mathsf{H}, \mathsf{N}, \mathsf{P}, \mathsf{M}\}$ are not equiprobable since nominal cycles N occur with a very high frequency. The right plot of Figure 6.5 shows examples of fuel mass fraction burned (MFB) traces of three combustion events: H, N, and P. The high energy cycle H in this plot reports 8% more IMEP than the nominal, slightly above the upper bound for N. High energy release is characterized by early flame kernel initiation and fast combustion rate. On the other hand, the partially burned cycle P in Figure 6.5 reports an IMEP value 15% less than nominal, right below the limit stated in Eqn. (6.3). In this case, the combustion process extends all the way past BDC (90 [deg aTDC]), suggesting a not optimal utilization of the fuel's chemical energy. This approach for categorizing combustion cycles is different from

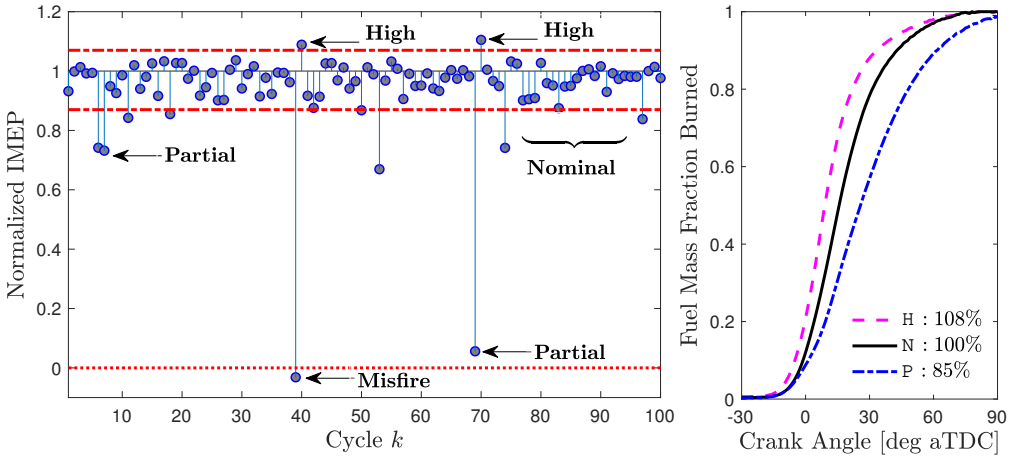


Figure 6.5: Left: Normalized IMEP at Point Z with cycle categorization. Right: Fuel mass fraction burned (MFB) of H, N, and P cycles.

the analysis in [3,68,69,75], where they divide the cycles into equiprobable categories. The reason behind this lies in the difficulty to identify deterministic patterns at the high dilution limit, where misfires are very infrequent (as illustrated in Seciton 6.3.1).

### 6.3.3 Nonlinear Dynamics and Deterministic Cyclic Characteristics

The categorization $\{\mathsf{H}, \mathsf{N}, \mathsf{P}, \mathsf{M}\}$ together with the nonlinear function $f$ in Eqn. (6.2) can be used to unravel the deterministic component of cyclic combustion variability. Figure 6.6 shows the return map of the normalized IMEP used for studying prior-cycle determinism. Wagner in [72] used a seventh order polynomial interpolation to capture more complex dynamics. In our case, since the dynamic system only has one equilibrium point (▲) at the nominal IMEP = 1, a third order polynomial is deemed sufficient (black solid line). To better understand the deterministic behavior, Figure 6.7 shows the plot of $f(\text{IMEP}_k)$ solely. Starting from elements in each category $\{\mathsf{H}, \mathsf{N}, \mathsf{P}, \mathsf{M}\}$, one can find the deterministic sequence that leads to equilibrium. One can show that the equilibrium point is attractive, meaning that every element in the domain of $f$ will eventually converge to IMEP = 1. Moreover, note that the set $\mathsf{N} = \{x \in \text{IMEP}_k \mid 87\% < x < 107\%\}$ is a positive invariant set for the dynamic system $\text{IMEP}_{k+1} = f(\text{IMEP}_k)$. Therefore, it suffices to start with any element in the domain of $f$ and continue until an element in N is reached. As an example, four different initial conditions (one from each category) have been chosen and their deterministic sequences have been indicated with arrows in Figure 6.7. The following

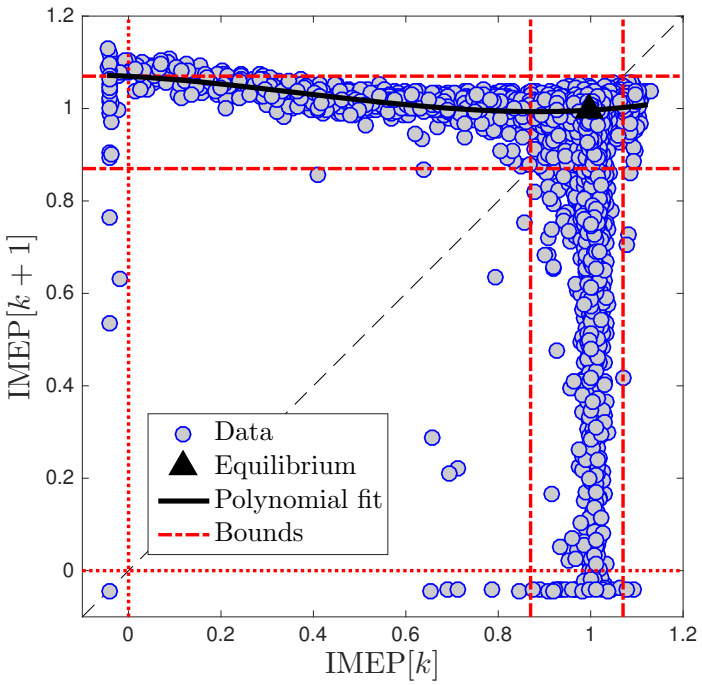


Figure 6.6: Return map of normalized IMEP for a sample of 150,000 engine cycles with a cycle lag of $m = 1$.

symbolic sequences are then considered deterministic:

$$\mathsf{H} \to \mathsf{N}, \quad \mathsf{N} \to \mathsf{N}, \quad \mathsf{P} \to \mathsf{N}, \quad \mathsf{M} \to \mathsf{H} \to \mathsf{N}. \tag{6.4}$$

After any element from H or P occur, the system returns to its nominal state N. In this case, most of the fuel has been burned or no significant amount of residual charge is present in the next cycle. However, after a misfire M occurs, there is a substantial amount of residual oxygen and fuel that will remain during the next cycle, causing a high energy release H. In more general terms, at the EGR dilution limit, combustion cycles with significantly low energy release (or no energy release at all) are followed by cycles with high energy release. This observation has been previously made by Kaul et al. in [3]. However, this deterministic behavior only predicts what will happen after M occurs, and it does not provide information of what triggers the events P or M. To further understand how the occurrence of events P or M can be modeled, we remove the deterministic component of cyclic CV to study only its stochastic component.

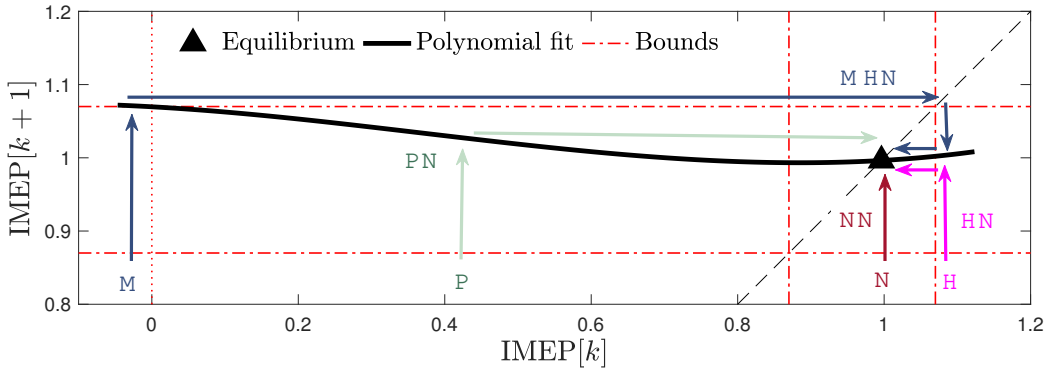


Figure 6.7: Nonlinear polynomial function $f(\text{IMEP}_k)$. Arrows describe the deterministic sequence starting with an element from $\{\mathsf{H}, \mathsf{N}, \mathsf{P}, \mathsf{M}\}$ continuing until the nominal condition $\mathsf{N}$ is reached.

## 6.4 Stochastic Cycle-to-Cycle Combustion Variability at the Misfire Limit

The previous Chapters showed that the occurrence of misfires can be modeled as a Bernoulli random process, when combustion cycles are classified into misfiring and non-misfiring cycles. In this case, however, combustion cycles are divided into four different categories. To do so, we first use the deterministic pattern discussed in Section 6.3.3 to simplify the number of categories for the analysis. Intuitively, we can reduce the number of symbols, i.e. $\{\mathsf{H}, \mathsf{N}, \mathsf{P}, \mathsf{M}\}$, in the time series by considering the deterministic sequences $\{\mathsf{NN}, \mathsf{PN}, \mathsf{MHN}\}$ as the new "symbols". Formally, this can be done by defining the following random variables:

$$\begin{aligned} W_{k+1} &= \text{IMEP}_{k+1} - f\left(\text{IMEP}_k\right), \qquad k > 0 \\ W_0 &= \text{IMEP}_0 - 1 \end{aligned} \quad . \tag{6.5}$$

This relation intrinsically defines the categorical transformation
$T\colon \ \{\mathsf{H}, \mathsf{N}, \mathsf{P}, \mathsf{M}\} \longrightarrow \{\mathbf{H}, \mathbf{N}, \mathbf{P}, \mathbf{M}\}$ , where the new categories are defined by the following bounds:

$$\mathbf{M} \leqslant -1 < \mathbf{P} \leqslant -13\% < \mathbf{N} < 7\% \leqslant \mathbf{H}. \tag{6.6}$$

This categorization captures the true nature of the variables $W_k$, which are the deviations from the expected IMEP cyclic behavior. Figure 6.8 shows the return map of the time series $\{W_k\}$. First, note that the plot is symmetric with respect to the 45° diagonal, which indicates no cyclic correlation between the events $W_k$ and $W_{k+1}$. Second, the set $\mathbf{H} = \{x \in W_k \mid 7\% \leqslant x\}$ is empty (indicated by the shaded area), meaning that the transformation $T$ effectively maps onto the simplified set $\{\mathbf{N}, \mathbf{P}, \mathbf{M}\}$.

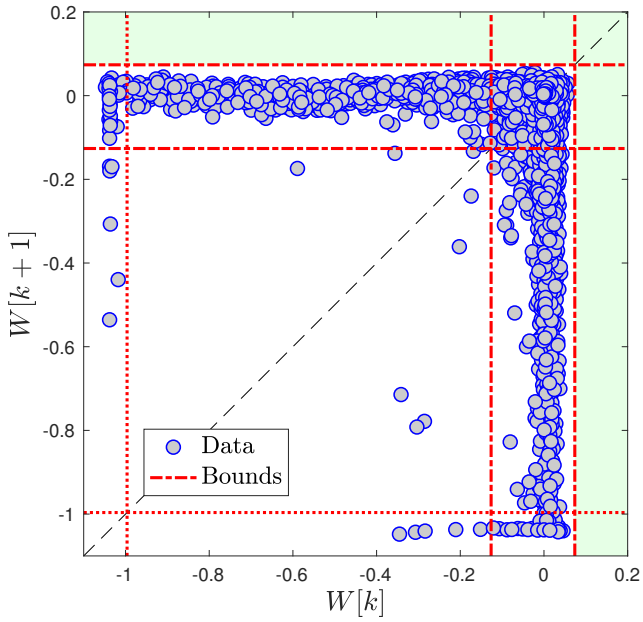


Figure 6.8: Return map of random variable $W$ defined in Eqn. (6.5).

This result stresses the fact that the occurrence of high energy cycles is deterministic. Furthermore, this behavior is the only deterministic component of cyclic CV, suggesting that the occurrence of partial burned cycles and misfires are stochastic in nature and require a probabilistic approach for modeling and control.

The normalized IMEP data was divided into the four original categories $\{\mathsf{H}, \mathsf{N}, \mathsf{P}, \mathsf{M}\}$. After the time series $\{W_k\}$ was computed, the number of elements in each new category $\{\mathbf{H}, \mathbf{N}, \mathbf{P}, \mathbf{M}\}$ was also calculated. Table 6.2 compares the number of engine cycles that fall into each category. Note that the number of elements in the categories $\mathsf{P}$ and $\mathbf{P}$ is very similar, despite the 2% reduction in cardinality. A similar scenario is apparent for categories $\mathsf{M}$ and $\mathbf{M}$. Therefore, the transformation $T$ induced by Eqn. (6.5) can be approximated by:

$$\begin{aligned} \widehat{T}\colon \quad \{\mathsf{H},\mathsf{N},\mathsf{P},\mathsf{M}\} &\longrightarrow \{\mathbf{N},\mathbf{P},\mathbf{M}\} \\ \{\mathsf{H},\mathsf{N}\} &\longmapsto \{\mathbf{N}\} \\ \{\mathsf{P}\} &\longmapsto \{\mathbf{P}\} \\ \{\mathsf{M}\} &\longmapsto \{\mathbf{M}\}. \end{aligned} \tag{6.7}$$

The reduction of the number of categories follows directly from removing the deterministic component of cyclic CV. Hence, the elements of the new categories $\mathbf{N}$, $\mathbf{P}$, and $\mathbf{M}$ are independent random variables. Note that the transformation $\widehat{T}$ does not require the calculation of the nonlinear function $f$. The advantage here is that the

Table 6.2: Cardinality of combustion cycles categories.

| Time series $\{\text{IMEP}_k\}$ | Time series $\{W_k\}$ | Reduction |
|---|---|---|
| $\lvert\mathsf{H}\rvert = 575$ | $\lvert\mathbf{H}\rvert = 0$ | 100% |
| $\lvert\mathsf{P}\rvert = 1365$ | $\lvert\mathbf{P}\rvert = 1337$ | 2% |
| $\lvert\mathsf{M}\rvert = 809$ | $\lvert\mathbf{M}\rvert = 807$ | 0.25% |

bounds for IMEP defined in Eqn. 6.3 are sufficient to categorize combustion cycles and separate the deterministic from the stochastic component of cyclic CV. The following sections rely on the stochastic component to determine probability metrics that can be used as feedback signals for combustion control.

### 6.4.1 Partial Burns and Misfires as Multinomial Random Variables

Consider any sequence of $n$ symbols **N**, **P**, and **M** extracted from the time series $\{W_k\}$. The previous result showed that such events are purely stochastic and statistically independent. Let $p_N$, $p_P$, and $p_M$ be the probability that a cycle falls in the category **N**, **P**, or **M** respectively. Within these $n$ samples, let $X_N$, $X_P$ and $X_M$ be the number of cycles classified as **N**, **P**, or **M** respectively. Since any $W_k$ can only be classified into one of the three previously mentioned categories, the following holds:

$$p_N + p_P + p_M = 1 \quad \text{and} \quad X_N + X_P + X_M = n. \tag{6.8}$$

Let $\mathbf{X} = \begin{bmatrix} X_N & X_P & X_M \end{bmatrix}^T$ and $\mathbf{p} = \begin{bmatrix} p_N & p_P & p_M \end{bmatrix}^T$. Then, $\mathbf{X}$ brings together the characteristic of a *multinomial random variable* with parameters $n$ and $\mathbf{p}$, denoted as $\mathbf{X} \sim \text{Multinom}(n, \mathbf{p})$. The probability mass function (PMF) of $\mathbf{X}$ can be calculated as follows:

$$\Pr\left( \mathbf{X} = \begin{bmatrix} x_N \\ x_P \\ x_M \end{bmatrix} \middle| \, n, \mathbf{p} \right) = \frac{n!}{x_N! x_P! x_M!} p_N^{x_N} p_P^{x_P} p_M^{x_M} \tag{6.9}$$

where $\Pr(\cdot \mid n, \mathbf{p})$ represents conditional probability given $n$ and $\mathbf{p}$. By means of Eqn. (6.8), we can simplify this calculation as a function of the two random variables

of interest, as follows:

$$\Pr\left(\mathbf{X} = \begin{bmatrix} x_N \\ x_P \\ x_M \end{bmatrix} \middle| n, \mathbf{p}\right) = \Pr\left(\begin{bmatrix} X_P \\ X_M \end{bmatrix} = \begin{bmatrix} x_P \\ x_M \end{bmatrix} \middle| n, \begin{bmatrix} p_P \\ p_M \end{bmatrix}\right) =$$

$$\frac{n!}{(n - x_P - x_M)! x_P! x_M!}(1 - p_P - p_M)^{n - x_P - x_M} p_P^{x_P} p_M^{x_M}. \tag{6.10}$$

Recall that if $\mathbf{X} \sim \text{Multinom}(n, \mathbf{p})$, the marginal random variables $X_P$ and $X_M$ must follow binomial distributions:

$$X_P \sim \text{Binom}(n, p_P) \quad \text{and} \quad X_M \sim \text{Binom}(n, p_M) \tag{6.11}$$

Using the maximum likelihood estimator (MLE), the probabilities $p_P$ and $p_M$ can be estimated as $\widehat{p}_P = \dfrac{x_P}{n}$ and $\widehat{p}_M = \dfrac{x_M}{n}$.

This behavior of $X_M$ was expected based on previous results. Using a similar procedure described in our previous study, the 150,000 experimental cycles where divided into smaller samples of size $n$ and the distributions of the variables $X_P$ and $X_M$ were computed. Figure 6.9 shows the PMF of the random variables $X_P$ and $X_M$ for a sample size of $n = 200$, utilizing the estimates $\widehat{p}_P$ and $\widehat{p}_M$ respectively. As expected, the marginal PMFs are in close agreement with the theoretical binomial distribution, according to Eqn. (6.11).

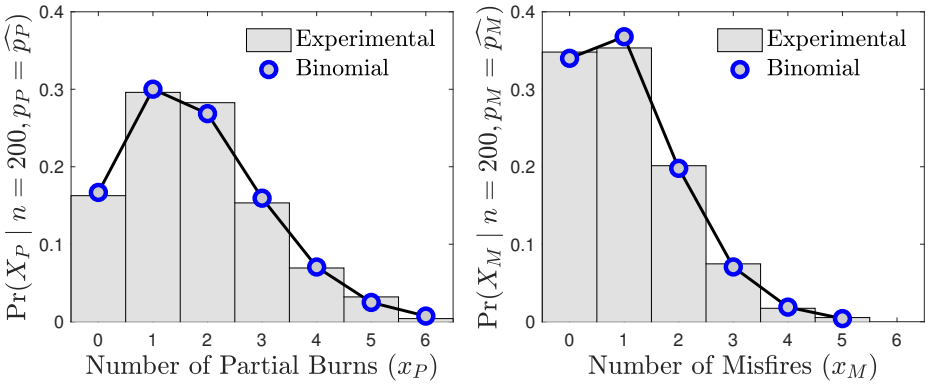


Figure 6.9: Experimental and theoretical marginal PMFs of random variables $X_P$ (number of partial burns: left) and $X_M$ (number of misfires: right).

Figure 6.10 shows the theoretical and experimental joint PMF of $X_P$ and $X_M$. Although the overall shape resembles the theoretical multinomial distribution, it is not immediate that the hypothesis of $\mathbf{X} \sim \text{Multinom}(n, \mathbf{p})$ is true. The Pearson's chi-squared goodness-of-fit test was used to establish if the differences be-

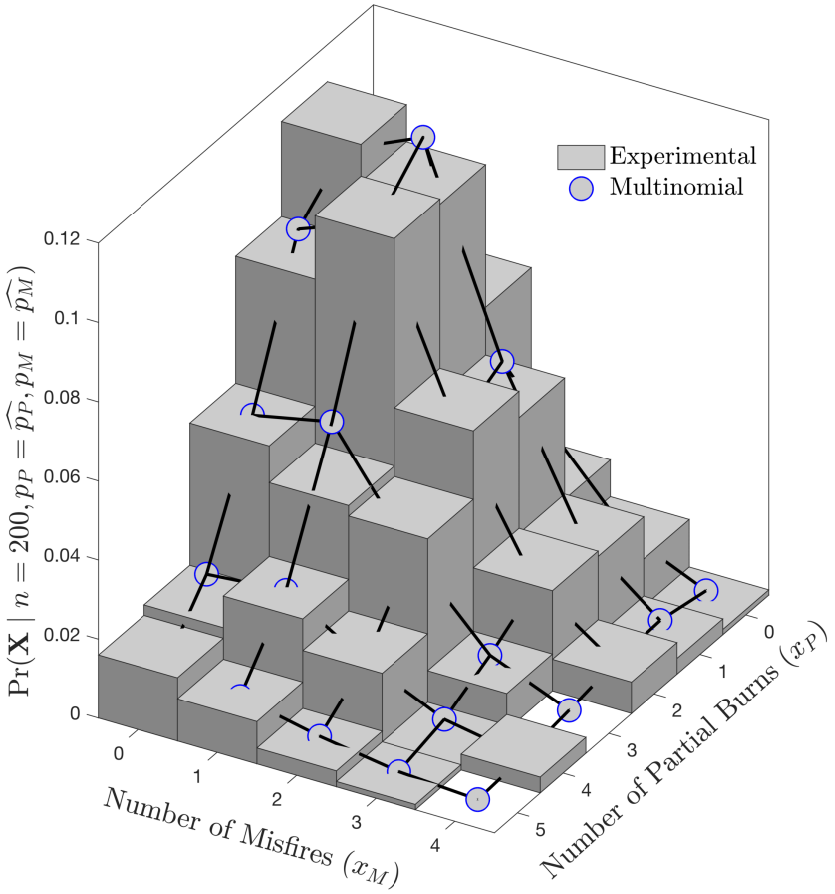


Figure 6.10: Experimental and theoretical multinomial PMF of $\mathbf{X}$, or equivalently, joint PMF of $X_P$ and $X_M$.

tween the observed frequency and theoretical distribution arose by mere randomness. The result shows that there is no statistical evidence against the hypothesis that $\mathbf{X} \sim \text{Multinom}(n, \mathbf{p})$.

### 6.4.2 Pearson's Chi-squared Goodness-of-fit Test for Multinomial Distribution

Table 6.3 shows the comparison between the observed ($O$) and expected ($E$) frequencies of pairs $(x_P, x_M)$ for $x_P \in \{0, 1, 2, 3, 4, 5\}$ and $x_M \in \{0, 1, 2, 3, 4\}$. These values were calculated by dividing the experimental set of 150,000 engine cycles into samples of size $n = 200$ and counting the numbers of samples that contain $x_P$ number of partially burned cycles and $x_M$ number of misfires. Define the following test-statistic:

$$\overline{\chi}^2 = \sum_{i=1}^{M} \frac{(O_i - E_i)^2}{E_i} \longrightarrow \chi^2(df) \tag{6.12}$$

Table 6.3: Observed and Expected frequencies ($\mathbf{O_i} \,|\, E_i$) of pairs $(x_P, x_M)$, equivalent to the joint PMF showed in Figure 6.10.

| **Misfires**: | **Partial burned cycles**: $x_P$ | | | | | |
|---|---|---|---|---|---|---|
| $x_M$ | 0 | 1 | 2 | 3 | 4 | 5 |
| 0 | **44** \| 42 | **83** \| 76 | **65** \| 69 | **41** \| 41 | **14** \| 18 | **12** \| 6 |
| 1 | **49** \| 46 | **76** \| 83 | **77** \| 74 | **34** \| 44 | **20** \| 19 | **8** \| 7 |
| 2 | **17** \| 25 | **40** \| 45 | **45** \| 40 | **32** \| 24 | **14** \| 10 | **3** \| 4 |
| 3 | **10** \| 9 | **18** \| 16 | **19** \| 14 | **7** \| 8 | **1** \| 4 | **1** \| 1 |
| 4 | **1** \| 2 | **3** \| 4 | **6** \| 4 | **0** \| 2 | **3** \| 1 | **0** \| 0 |

Assuming that the sample size is adequate, the random variable $\overline{\chi}^2$ approaches asymptotically a chi-squared distribution with degrees of freedom $df = M - m_p - 1$, where $m_p = 2$ is the number of estimated parameters. Note that some cells in Table 6.3 have a expected cell count $E_i < 5$. It is common practice to group such cells into a larger class where $E_i > 5$. Hence, $M$ is smaller than the number of cells in the Table 6.3. If the data indeed follow a multinomial distribution and using a confidence level of 95%, the corresponding critical value from the chi-squared distribution is $\chi^2_{.95}(df) = 31.4$. The value of the test-statistic is $\overline{\chi}^2 = 21$. Therefore, there is insufficient statistical evidence against the hypothesis that $\mathbf{X} \sim \text{Multinom}(n, \mathbf{p})$.

## 6.5 Estimation and Control of the Misfire Probability

A stochastic control strategy can be design to target a given misfire probability $p^*_M$ using the likelihood ratio approach developed by Peyton Jones in [21, 61, 67]. This controller, however, assumes that there are only two categories (misfires or no misfires). By extending this notion to three categories (**N**, **P**, and **M**) one can use the information of events **P** to update the PMF of $X_M$. By observing partial burns, which occur with a higher probability than misfires, the sample size required for MLE can be reduced. Consequently, the response of the controller is expected to 1) improve with respect to aggressively adjusting EGR-vale and/or spark to move away from misfires, and 2) reduced cyclic CV induced by closed-loop control.

### 6.5.1 Estimating the Misfire Probability Given the Probability Mass Function (PMF) of Partial Burns

Consider that, in a given sample, the number of partial burned cycles $x_P$ are counted. Given the join probability distribution of the number of misfires and partial

burns, the conditional probability of $X_M$ given that $x_P$ partial burned cycles have occurred can be calculated as follows:

**Proposition 6.1.** *Let* $\mathbf{X} \sim Multinom(n, \mathbf{p})$ *with* $\mathbf{X} = \begin{bmatrix} X_N & X_P & X_M \end{bmatrix}^T$ *and* $\mathbf{p} = \begin{bmatrix} p_N & p_P & p_M \end{bmatrix}^T$. *Then,*

$$Pr(X_M = x_M \mid X_P = x_P, n, \mathbf{p}) \sim Binom\left(n - x_P, \frac{p_M}{1 - p_P}\right). \tag{6.13}$$

*Proof.* By the definition of conditional probability:

$$\begin{aligned}
\Pr(X_M = x_M \mid X_P = x_P, n, \mathbf{p}) &= \frac{\Pr(X_M = x_M, X_P = x_P \mid n, \mathbf{p})}{\Pr(X_P = x_P \mid n, \mathbf{p})} \\
&= \frac{\dfrac{n!}{(n - x_P - x_M)! x_P! x_M!}(1 - p_P - p_M)^{n - x_P - x_M} p_P^{x_P} p_M^{x_M}}{\dfrac{n!}{x_P!(n - x_P)!} p_P^{x_P}(1 - p_P)^{n - x_P}} \\
&= \frac{(n - x_P)!}{x_M!(n - x_P - x_M)!} \cdot \frac{p_M^{x_M}(1 - p_P - p_M)^{n - x_P - x_M}}{(1 - p_P)^{n - x_P}} \\
&= \frac{(n - x_P)!}{x_M!(n - x_P - x_M)!} \left(\frac{p_M}{1 - p_P}\right)^{x_M} \left(1 - \frac{p_M}{1 - p_P}\right)^{n - x_P - x_M}.
\end{aligned}$$

□

Note that this distribution is different from the one defined in Eqn.(6.11), where no information of partial burned cycles is used.

**Remark 1.** $p_M \leqslant \dfrac{p_M}{1 - p_P}$ *always holds for* $0 \leqslant p_M, p_P \leqslant 1$. *This means that when* $\mathbf{P}$ *cycles are observed, the conditional probability of observing misfiring cycles increases.*

**Remark 2.** *According to Eqns.*(6.11) *and* (6.13), *if* $x_p \ll n$ *and* $p_P \ll 1$, *then* $Pr(X_M = x_M \mid X_P = x_P, n, \mathbf{p}) \approx Pr(X_M = x_M \mid n, p_M)$. *This means that observing* $\mathbf{P}$ *cycles does not alter significantly the distribution of* $X_M$ *if the probability* $p_P$ *is too small and the sample window is large compared with* $x_p$.

**Remark 3.** *Recall that the expected value of the variable* $X_M$ *is* $E[X_M \mid n, p_M] = np_M$. *On the other hand, the conditional expectation is* $E[X_M \mid X_P = x_P, n, \mathbf{p}] = (n - x_p)\dfrac{p_M}{1 - p_P}$. *However, when the maximum likelihood estimator* $\widehat{p}_P = x_P/n$ *is used:*

$$E[X_M \mid X_P = x_P, n, \widehat{p}_P, p_M] = E[X_M \mid n, p_M] = np_M. \tag{6.14}$$

*The information from* $\mathbf{P}$ *cycles is lost when MLE of* $p_P$ *is used for calculating conditional expectation.*

Although the expected number of misfires $\mathrm{E}[X_M]$ is not altered when partially burned cycles are observed, the misfire probability $p_M$ is affected in the conditional case. Let $p_{M|P} = \dfrac{p_M}{1-p_P}$, then the probability of observing a misfire given that $x_M$ misfires and $x_P$ partial burns have been observed can be estimated as follows:

**Proposition 6.2.** *If the conditional density*
$Pr(X_M = x_M \mid x_P, n, p_P, p_M) \sim Binom\left(n - x_p, p_{M|P}\right)$ *where* $p_{M|P} = \dfrac{p_M}{1-p_P}$*, then the maximum likelihood estimator (MLE) for the parameter* $p_{M|P}$ *is*

$$\widehat{p}_{M|P} = \frac{\widehat{p}_M}{1-\widehat{p}_P} = \frac{x_M}{n-x_P}. \tag{6.15}$$

*Proof.* For the binomial distribution described by Proposition 6.1, the log-likelihood function is defined as:

$$\begin{aligned}
&\ln \mathcal{L}(p_{M|P}, x_M, x_P) = \ln \Pr(X_M = x_M \mid X_P = x_P, n, \mathbf{p}) \\
&= \ln\left(\frac{(n-x_P)!}{x_M!(n-x_P-x_M)!}\right) + x_M \ln\left(p_{M|P}\right) \\
&+ (n - x_P - x_M)\ln\left(1 - p_{M|P}\right).
\end{aligned}$$

Taking the partial derivative with respect to the parameter of interest:

$$\frac{\partial}{\partial p_{M|P}} \ln \mathcal{L}(p_{M|P}, x_M, x_P) = \frac{x_M}{p_{M|P}} - \frac{n - x_P - x_M}{1 - p_{M|P}}.$$

The log-likelihood function is maximized when the partial derivative equals zero, then:

$$\frac{x_M}{\widehat{p}_{M|P}} - \frac{n - x_P - x_M}{1 - \widehat{p}_{M|P}} = 0 \iff \widehat{p}_{M|P} = \frac{x_M}{n - x_P}.$$

□

So far, three different probabilities related to events $\mathbf{P}$ and $\mathbf{M}$ can be estimated: $\widehat{p}_P$, $\widehat{p}_M$, and $\widehat{p}_{M|P}$. Either of this values can be targeted for control. However, since all of them are inverse proportional to the parameter $n$, choosing $\max\{\widehat{p}_P, \widehat{p}_M, \widehat{p}_{M|P}\}$ can reduce the number of samples required for estimation, increasing effectively the responsiveness of the control strategy.

### 6.5.2 Relationship between Conditional Probabilities

Remark 1 shows that $\widehat{p}_M \leqslant \widehat{p}_{M|P}$. In order to derive a relationship between $\widehat{p}_{M|P}$ and $\widehat{p}_P$ consider defining the function:

$$\Phi(\widehat{p}_M, \widehat{p}_P) = \widehat{p}_P(\widehat{p}_P - 1) + \widehat{p}_M. \tag{6.16}$$

Note that if $\Phi \leqslant 0$ then $\widehat{p}_{M|P} \leqslant \widehat{p}_P$. Let $p_P^c$ be the critical value for the probability of **P** events such that $\widehat{p}_{M|P} = p_P^c$, then:

$$p_P^c = \frac{\widehat{p}_M}{1 - p_P^c} \implies p_P^c = \frac{1}{2} \pm \sqrt{\frac{1}{4} - \widehat{p}_M}. \tag{6.17}$$

Note further that $\Phi(\widehat{p}_M, p_P^c) = 0$. Assuming that the function $\Phi$ is defined over the domain $D$: $(\widehat{p}_M, \widehat{p}_P) \in [0, 1/4] \times [0, 1/2]$, Eqn. (6.17) has a unique real solution for a given $\widehat{p}_M$. Figure 6.11 shows the function $\Phi$ evaluated in the domain $D$. The solid line indicates the critical value of $\Phi$ where $\widehat{p}_{M|P} = p_P^c$. The shaded area to the left of such line represents the subset of $D$ where $\Phi < 0$, and hence where $\widehat{p}_{M|P} < \widehat{p}_P$. The dashed line in Figure 6.11 represents the equality $\widehat{p}_P = 2\widehat{p}_M$. Note that it suffices that:

$$\text{if} \quad \begin{array}{c} \widehat{p}_P \geqslant 2\widehat{p}_M \\ (\text{or } x_P \geqslant 2x_M) \end{array} \quad \text{and } \widehat{p}_M \in [0, 1/4] \implies \widehat{p}_M \leqslant \widehat{p}_{M|P} \leqslant \widehat{p}_P. \tag{6.18}$$

Figure 6.12 shows the estimated probabilities $\widehat{p}_M$, $\widehat{p}_{M|P}$ and $\widehat{p}_P$ for a variety of spark advance/EGR valve combinations. For each estimator, three different sample

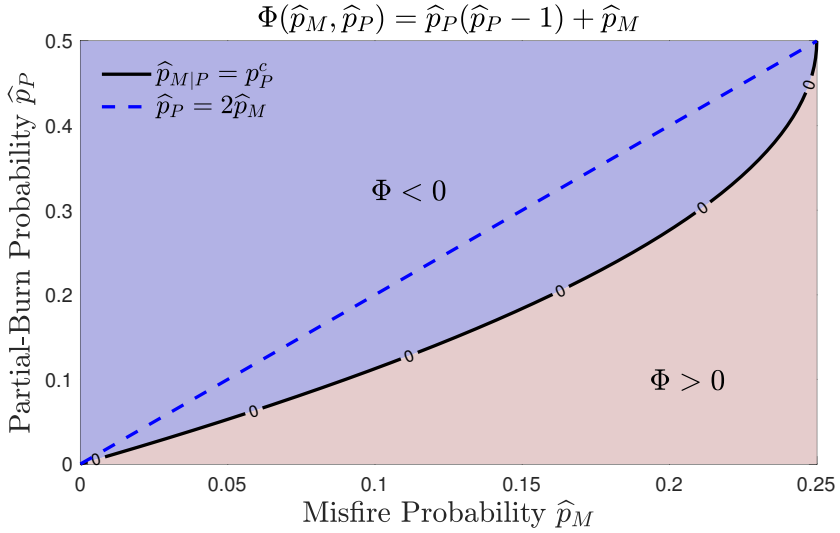


Figure 6.11: Function $\Phi(\widehat{p}_M, \widehat{p}_P)$ evaluated over domain $D$.

sizes $n \in \{200, 1000, 2000\}$ were used for all operating conditions. As expected, $\widehat{p}_P$ increases as EGR valve opening increases. Also, $\widehat{p}_M$ increases when EGR valve opening and spark advance increase. The experimental values show that $\widehat{p}_P \approx 20\widehat{p}_M$, which corroborates the analytical result that $\widehat{p}_M \leqslant \widehat{p}_{M|P} \leqslant \widehat{p}_P$. The different columns of Figure 6.12 show the sensitivity of the estimation with respect to the parameter $n$. Although $n = 2000$ provides the highest level of accuracy, the estimator will have a very slow transient response when either spark advance of EGR valve are adjusted. If either $\widehat{p}_M$ or $\widehat{p}_{M|P}$ is the target for control, $n = 1000$ resembles accurately the estimated values. However, when $n = 200$ the estimators $\widehat{p}_M$ or $\widehat{p}_{M|P}$ loose resolution. On the other hand, the estimator $\widehat{p}_P$ is relatively accurate for any $n \in \{200, 1000, 2000\}$. Despite the fact that targeting a desired $\widehat{p}_P$ requires the least amount of sampled cycles, this strategy only controls the upper bound of $\widehat{p}_M$ and not the misfire probability itself. In other words, control of the probability $\widehat{p}_P$ provides *indirect control* over the misfire probability $\widehat{p}_M$ but it requires the least amount of cycles for estimation, making it preferable for a fast response feedback controller.

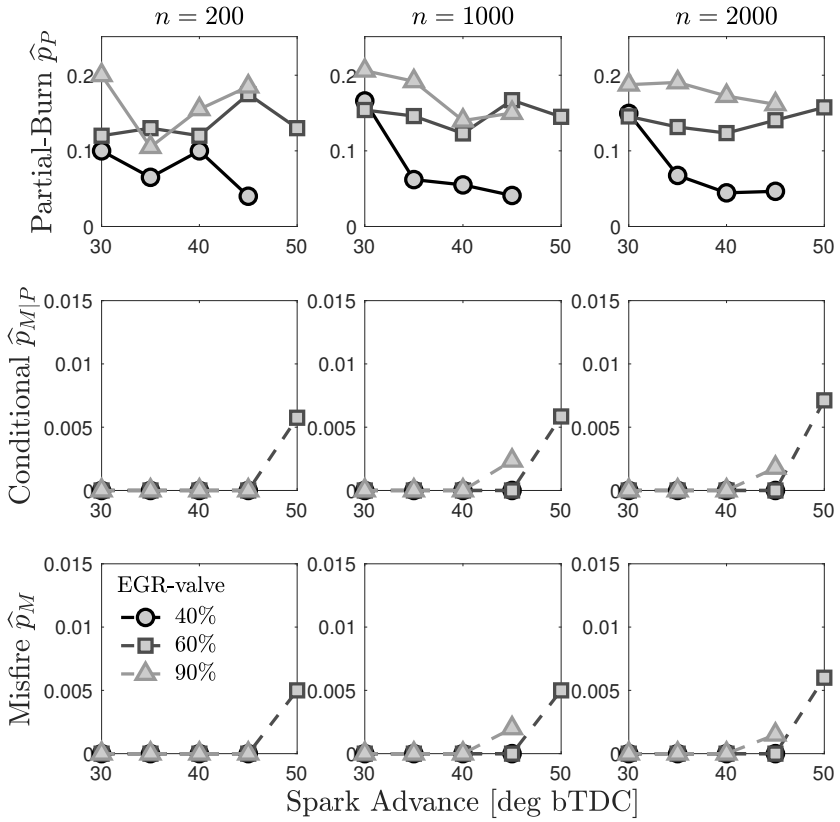


Figure 6.12: Comparison between $\widehat{p}_M$, $\widehat{p}_{M|P}$ and $\widehat{p}_P$ for experimental data at different spark advance and EGR valve positions. When $n = 200$, $\widehat{p}_M$ and $\widehat{p}_{M|P}$ loose resolution. However, $\widehat{p}_P$ is relatively accurate.

### 6.5.3 Implementation of Non-equiprobable Cyclic Categorization for Feedback Combustion Control

Figure 6.13 summarizes how the non-equiprobable categorization method can be implemented in a feedback control strategy. After calculating the magnitude of IMEP, the first block categorizes the combustion cycle into $\{\mathsf{H}, \mathsf{N}, \mathsf{P}, \mathsf{M}\}$ according to the inequalities described in Eqn. (6.3). Immediately after, the categorical transformation $\widehat{T}$, described in Eqn. (6.7), is applied and the new categories $\{\mathbf{N}, \mathbf{P}, \mathbf{M}\}$ are used. Recall that the transformation $\widehat{T}$ is the approximation of the actual removal of the deterministic component of cyclic CV. Once the combustion cycle has been categorized as either **N**, **P**, or **M**, and using a fixed window size $n$ for estimation, the MLE is used to estimate the probabilities $\widehat{p}_M$, $\widehat{p}_{M|P}$, and $\widehat{p}_P$. If the conditions discussed in Eqn. (6.18) are met, $\widehat{p}_P$ achieves the highest value, which requires the least amount of samples for estimation (decreasing $n$). Hence, $\widehat{p}_P$ can be used to indirectly control the misfire probability by using the least amount of cycles for estimation, which improves the speed of response without the drawback of high cyclic variability. On the other hand, if a precise control of $p_M$ is needed, the conditional probability $\widehat{p}_{M|P}$ should be used for feedback. The feedback (stochastic) controller will target a desired probability, either $p^*_{M|P}$ or $p^*_P$, and will adjust spark advance and/or EGR valve to change the operating condition. By adjusting the dilution and keeping spark at MBT, the controller can reduce the probability of misfire while maximizing EGR benefits.

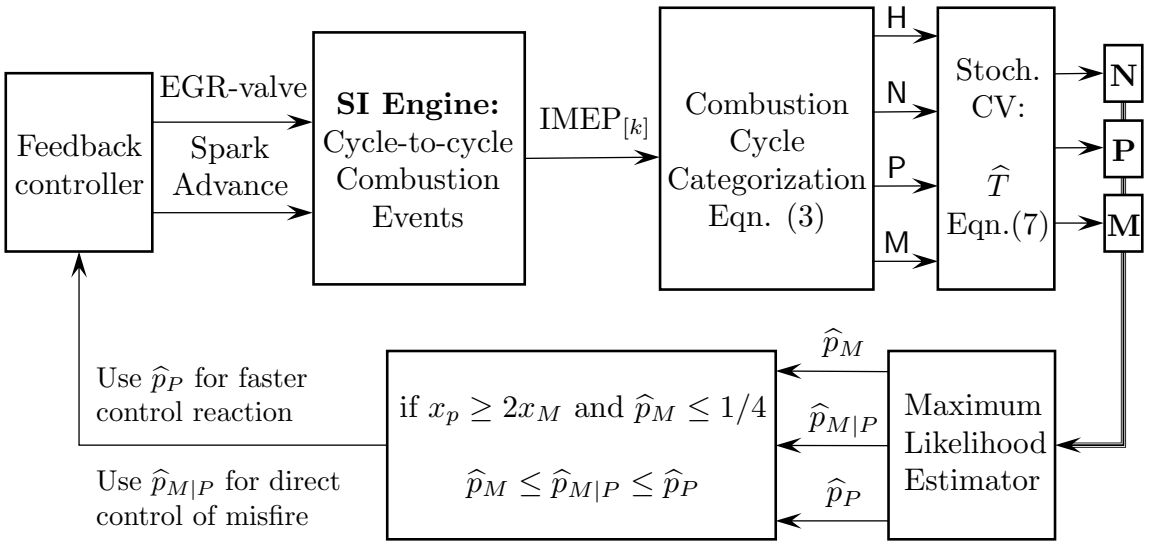


Figure 6.13: Block diagram of proposed control strategy using non-equiprobable combustion cycle classification.

## 6.6 Summary

A non-equiprobable categorization method has been developed to classify engine combustion cycles at high levels of EGR. Upper and lower bounds on the normalized IMEP were used to group combustion cycles into four different categories:

1. High energy release ($\mathsf{H}$): values above nominal conditions
2. Nominal ($\mathsf{N}$): values between predefined bounds
3. Partial Burns ($\mathsf{P}$): values below nominal, but with nonzero energy release
4. Misfires ($\mathsf{M}$): values with zero energy release

Time series analysis of IMEP showed that deterministic prior cycle correlation corresponds to sequences of misfires followed by high energy cycles ($\mathsf{M} \rightarrow \mathsf{H}$). Meanwhile, the occurrence of misfires and partial burns appear to be random. These categories can be used to easily separate the deterministic from the stochastic component of cycle-to-cycle combustion variability. Therefore, stochastic control theory can be applied for controlling the probability of misfire events while a deterministic controller can be designed to avoid high energy cycles after misfires.

A multinomial distribution was fitted to the experimental joint PMF of partial burns and misfires. After this process, observation of partial burns can be used to obtain a better estimate of the misfire probability. Hence, three different probability measures can be estimated by observing partial burns and/or misfires:

1. $\widehat{p}_M$: estimated misfire probability
2. $\widehat{p}_{M|P}$: estimated conditional misfire probability given that some number of partial burns have been observed
3. $\widehat{p}_P$: estimated probability of partial burns

Under certain conditions, $\widehat{p}_P$ achieves the highest value, which requires a smaller window for estimation. This metric is preferred for feedback control due to their responsiveness when the actual probability changes. However, targeting $\widehat{p}_P$ only changes the upper bound on $\widehat{p}_M$, resulting in indirect control of the misfire probability. On the other hand, $\widehat{p}_{M|P}$ guarantees a direct control over the misfire probability but requires a larger sample size for estimation.

# CHAPTER VII

# Learning Reference Governor for Cycle-to-Cycle Combustion Control with Misfire Avoidance in SI Engines at High EGR-Diluted Conditions

## 7.1 Motivation

Worldwide regulations on greenhouse gas emissions demand a reduction in fuel consumption from the transportation sector. As a consequence, increasingly stringent tailpipe emission targets have to be met, especially during real-world driving cycles. Feedback combustion control has the potential to improve the overall efficiency of spark-ignition (SI) engines by optimizing combustion efficiency, reducing heat transfer losses, and reducing pumping losses at medium loads. In particular, external cooled exhaust gas recirculation (EGR) in modern SI engines has provided numerous benefits in fuel economy and emissions. This study focuses on the control problem of optimizing combustion phasing while maximizing EGR benefits during load transients. Additionally, the controller will be designed to avoid transient states where the EGR level is higher than the dilution tolerance of the charge, thereby avoiding occasional misfires. The methodology presented in this Chapter is intended to be applied for different load demands during real-world driving scenarios.

The control strategy was designed from a control-oriented model that includes the effects of throttle changes in the combustion. An adaptive extended Kalman filter was designed to estimate intake manifold states and filter combustion measurements used for feedback. A linear quadratic regulator (LQR) was designed to reject throttle disturbances and maintain an optimal combustion phasing while maximizing EGR levels at different loads. A learning reference governor was designed to modify aggressive throttle commands in order to avoid transient states located over the misfire

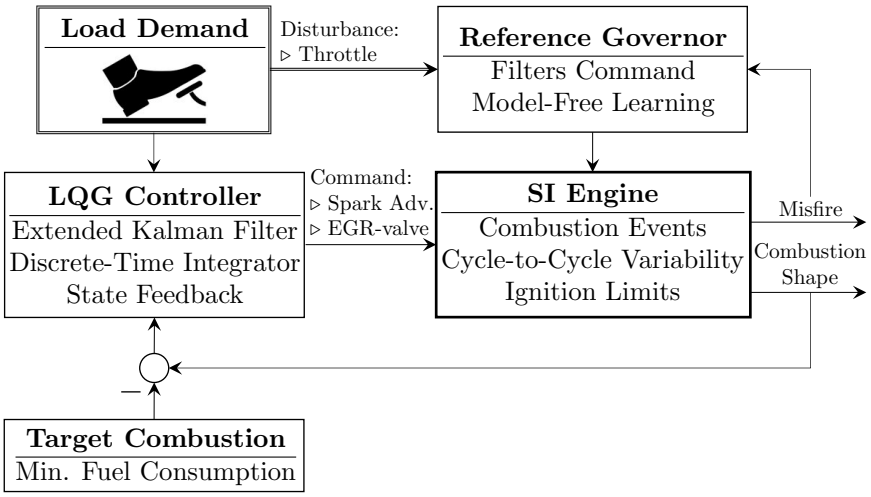


Figure 7.1: Block diagram of proposed control algorithm.

limit. Figure 7.1 shows the block diagram of the proposed control strategy explored in this Chapter.

## 7.2 Optimal Phasing and Combustion Limits

The single-zone heat release analysis was performed in order to calculate combustion features. The net heat release ($Q_{\text{net}}$) was calculated by considering only the changes in sensible internal energy and work transfer to the piston but omitting heat transfer and blow-by effects. Assuming a constant polytropic coefficient of $\gamma = 1.32$, the rate of heat release can be calculated as [18]:

$$dQ_{\text{net}} = \frac{\gamma}{\gamma - 1} P\, dV + \frac{1}{\gamma - 1} V\, dP, \tag{7.1}$$

where $P$ and $V$ are the in-cylinder pressure and volume respectively. Integrating over the crank angle (CA) domain and normalizing by $\max\{Q_{\text{net}}\}$ results in the mass fraction burned (MFB) shown in Figure A.1. Define the combustion features based on the MFB trace as:

**CAxx:** Crank angle at xx% of MFB, xx $\in [0, 100]$.

In particular, CA50 will be used as the indicator of optimal combustion phasing due to the large modeling efforts for engine optimization and calibration found in the literature in recent years [31, 76–79].

The three actuators influencing the combustion process in this study are 1) the throttle valve to adjust airflow, 2) the EGR valve to adjust the EGR rate into the

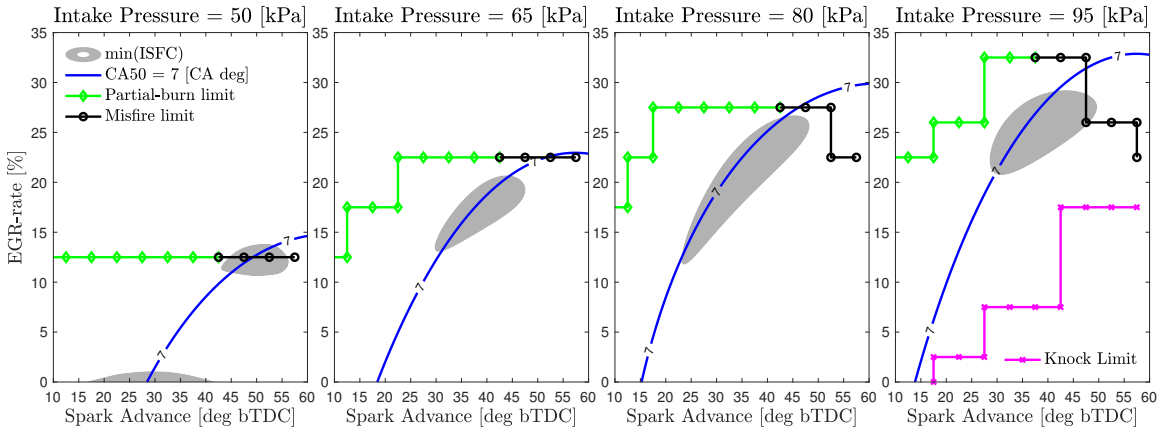


Figure 7.2: Steady state spark/EGR sweep at different intake manifold pressures. 2000 engine cycles were recorded at each spark/EGR pair. Partial-burns, misfires, and knocking cycles constraint the nominal operating region. Minimum fuel consumption is indicated by the grey shaded area and optimal combustion phasing (CA50 = 7 [CA deg]) by the blue solid line.

cylinders, and 3) the spark advance to adjust phasing. Figure 7.2 shows a spark/EGR sweep at four different intake manifold pressures (50, 65, 80, and 95 [kPa]). Each spark/EGR combination was ran at steady state and 2000 engine cycles were recorded. Experimentally, not all combinations were achievable due to the occurrence of undesired combustion events. Therefore, the nominal stable operating region is constraint by the following three combustion limits:

**Partial-burn limit:** Minimum spark advance and maximum EGR rate for complete combustion (-◇-).

**Misfire limit:** Maximum spark advance and maximum EGR rate where no misfire event is identified (-○-).

**Knock limit:** Maximum spark advance at low EGR levels at which knock is avoided (-×-).

Misfire and partial-burn cycles are defined based on their net mean effective pressure (NMEP). Here, if cycle $k$ has NMEP $\leqslant 0$ then it is classified as misfire and if NMEP is positive but produces less than 70% of the nominal expected NMEP, it is classified as a partial-burn. The grey shaded area on each subplot corresponds to the region where the minimum indicated specific fuel consumption (ISFC) is achieved. Note that, across load conditions, the minimum fuel consumption is achieved right before the misfire limit. Since the misfire limit changes with load, increasing the dilution tolerance as intake pressure increases, the optimal EGR valve and spark advance need

to be adjusted continuously. Nonetheless, the optimal combustion phasing seems to be fairly constant across EGR and load conditions, with a value of CA50 = 7 [CA deg] (solid blue line).

### 7.2.1 Combustion Control Targets

Consider a controller that automatically adjusts the spark advance and EGR valve to achieve the target combustion phasing of CA50$^*$ = 7 [CA deg]. Figure 7.2 shows that, at any given load, such a spark/EGR combination is not unique. Hence, it is required to choose another target variable that renders a unique solution for a two-input two-output (TITO) system. Based on the effect that EGR has on the combustion kinetics, previous studies done by the authors used the crank angle duration from CA10 to CA90 (CA1090) as the second variable for feedback control [40]. However, further analysis showed that the feasibility of the tracking control problem could be compromised if the pair (CA50, CA1090) is used as a target [42]. A more recent study showed that the angle $\Theta^{\mathrm{SA50}}$ = CA50+SA, which is the duration from spark to CA50, together with CA50 is sufficient for a feasible TITO tracking control problem [80]. By using the pair $(\mathrm{CA50}, \Theta^{\mathrm{SA50}})$, the modeling effort for control design is reduced, while guaranteeing a unique equilibrium point for the closed-loop system. Note that, for intake pressures between 65 and 95 [kPa], the optimal spark timing is fairly constant around 37 [deg bTDC] even though the EGR rate increases from around 17 to 27 [%]. Therefore, the optimal duration for these conditions is $\Theta^{\mathrm{SA50}^*} = 44$ [CA deg]. At 50 [kPa] intake manifold pressure the target needs to be adjusted to $\Theta^{\mathrm{SA50}^*} = 50$ [CA deg], reflecting the increase in spark advance needed.

The TITO system then consists of EGR valve and spark advance as inputs, CA50 and $\Theta^{\mathrm{SA50}}$ as outputs, and changes in throttle angle as a disturbance induced by the driver's load demand. The controller will be based on a control-oriented model that captures the effects of actuators on the combustion targets.

## 7.3 Control-Oriented Engine Model

During load transients, changes on the throttle and EGR valve generate a change in the air and EGR flow into the cylinder. This directly affects the combustion process and needs to be accounted for in the control design. The gas properties in the intake manifold are captured by a two-state model representing the dynamics of intake manifold pressure ($P_m$) and EGR rate ($X_{\mathrm{EGR}}$). The manifold filling dynamics are derived from the total gas and EGR gas flow balances, together with the ideal

gas law [81]. This results in the following:

$$\frac{d}{dt}P_m = \frac{RT_m}{V_m}(W_{\text{air}} + W_{\text{EGR}} - W_{\text{cyl}}) \tag{7.2}$$

$$\frac{d}{dt}X_{\text{EGR}} = \frac{RT_m}{P_m V_m}\left[W_{\text{EGR}}(1 - X_{\text{EGR}}) - W_{\text{air}}X_{\text{EGR}}\right]. \tag{7.3}$$

Here, $T_m$ and $V_m$ are the intake manifold temperature and volume, $R$ is the specific gas constant for dry air, and $W_{\text{air}}$, $W_{\text{EGR}}$, and $W_{\text{cyl}}$ correspond to the airflow through the throttle body, EGR flow through the EGR valve, and engine pumping rate, respectively.

The air and EGR flows were modeled using standard orifice equations that depend on upstream conditions, pressure differential across the valves, and the corresponding valve openings [23]:

$$W_{\text{air}} = A_\theta(d_\theta)\frac{P_b}{\sqrt{RT_b}}\Psi\left(\frac{P_m}{P_b}\right) \tag{7.4}$$

$$W_{\text{EGR}} = A_{\text{EGR}}(U_{\text{EGR}})\frac{P_{\text{EGR}}}{\sqrt{RT_{\text{EGR}}}}\Psi\left(\frac{P_m}{P_{\text{EGR}}}\right). \tag{7.5}$$

Here, $T_b$ and $P_b$ are the boost temperature and pressure, $T_{\text{EGR}}$ and $P_{\text{EGR}}$ are the temperature and pressure in the EGR loop, $d_\theta$ is the throttle position, and $U_{\text{EGR}}$ is the EGR valve position. The functions $A_\theta(\cdot)$ and $A_{\text{EGR}}(\cdot)$ correspond to the effective flow area of each valve that is determined by regressing experimental data. The function $\Psi(\cdot)$ is the standard orifice flow function:

$$\Psi(x) = \begin{cases} \sqrt{\gamma\left(\frac{2}{\gamma+1}\right)^{\frac{\gamma+1}{\gamma-1}}}, & x < \left(\frac{2}{\gamma+1}\right)^{\frac{\gamma}{\gamma-1}} \\ x^{\frac{1}{\gamma}}\sqrt{\frac{2\gamma}{\gamma-1}\left[1 - x^{\frac{\gamma-1}{\gamma}}\right]}, & x \geqslant \left(\frac{2}{\gamma+1}\right)^{\frac{\gamma}{\gamma-1}} \end{cases} \tag{7.6}$$

where $\gamma$ is the ratio of specific heats. The total engine intake mass flow ($W_{\text{cyl}}$) depends on the volumetric efficiency, which itself depends on intake and exhaust pressures. This dependence needs to be experimentally regressed. Therefore, at a specific constant engine speed:

$$W_{\text{cyl}} = h_{\text{cyl}}(P_m, T_m, P_{\text{EGR}}) \tag{7.7}$$

where $h_{\text{cyl}}(\cdot)$ is a nonlinear function regressed from steady state data. According to

Figure A.1, most of these variables are known or measured by pressure-temperature sensors. The only quantity that is not currently measured directly in the engine is the EGR rate ($X_{\text{EGR}}$). Therefore, $X_{\text{EGR}}$ needs to be estimated in order to use a state feedback controller.

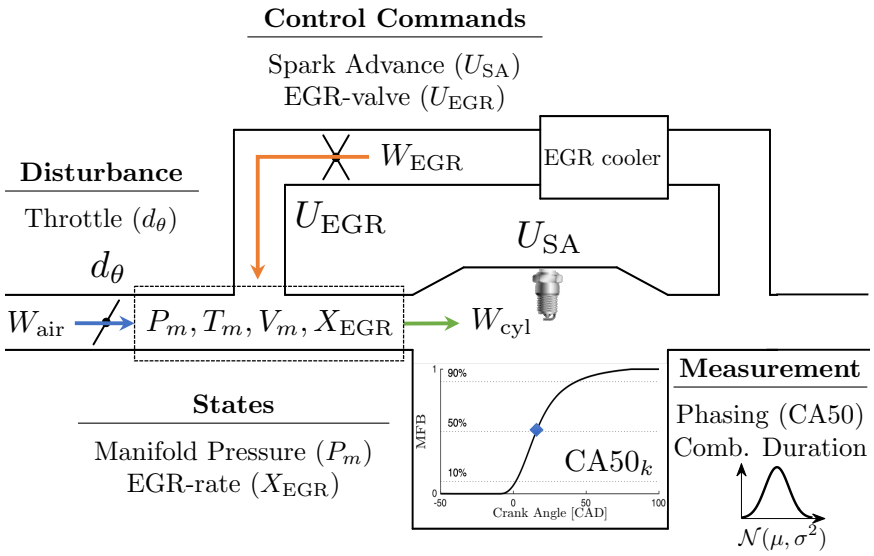


Figure 7.3: Control-oriented modeling of intake manifold filling dynamics and combustion phasing with CCV.

The engine breathing dynamics are described by a set of continuous-time nonlinear ordinary differential equations. However, the combustion events occur at discrete-time instants with a sample time equivalent to one engine cycle. In addition to this, cycle-to-cycle variability (CCV) affects the measurement of combustion-related parameters, such as CA50. Based on the observations made from Figure 7.2, the combustion phasing with stochastic CCV is modeled as follows:

$$\text{CA50}_k = g(P_m[k], X_{\text{EGR}}[k], U_{\text{SA}}[k]) + \sigma_{\text{CA50}}[k] w_k. \tag{7.8}$$

The index $k$ emphasizes the discrete-time nature of the observations. Here, $g(\cdot)$ is a nonlinear function regressed from the experimental results reported in Figure 7.2 and $U_{\text{SA}}$ is the spark advance command that acts on a cycle-by-cycle basis. The combustion CCV is introduced by the set of variables $\{w_k\}_{k\in\mathbb{N}}$ as additive output disturbances. Based on previous literature, such variables are modeled by a sequence of independent and identically distributed Gaussian random variables with zero mean and unit variance [40, 82]. The magnitude of the CCV is captured by the standard deviation $\sigma_{\text{CA50}}$ which depends on intake pressure, EGR rate, and spark advance.

Figure 7.3 shows the main components of the proposed TITO system. Note that this modeling approach only focuses on the intake manifold conditions and the combustion phasing. Hence, turbocharger modeling is not required.

Given the measured $\text{CA50}_k$ at each cycle and using the proposed model, a cycle-by-cycle estimate of $X_{\text{EGR}}$ can be obtained using a dynamic estimator. This state estimate not only will be used for state feedback control but could also filter the CA50 signal used for tracking.

## 7.4 State Estimation and CA50 Filtering

Consider the EGR rate dynamics described in Eqn.(7.3). Such a differential equation can be rewritten as:

$$\begin{aligned}\frac{d}{dt}X_{\text{EGR}} &= -\frac{W_{\text{EGR}} + W_{\text{air}}}{\frac{P_m V_m}{RT_m}}X_{\text{EGR}} + \frac{W_{\text{EGR}}}{\frac{P_m V_m}{RT_m}} \\ \frac{d}{dt}X_{\text{EGR}} &= -aX_{\text{EGR}} + b \end{aligned} \tag{7.9}$$

which is linear with respect to $X_{\text{EGR}}$. The combustion measurements are described by the nonlinear Eqn. (7.8). Since combustion events occur in discrete-time, Eqn. (7.9) needs to be discretized in order to use the CA50 measurements to estimate $X_{\text{EGR}}$ at each cycle. Therefore, an extended Kalman filter (EKF) can be used for state estimation. The standard EKF approach depends on additive noise disturbances for the system dynamics and output. Note, however, that the dynamics in the model are not corrupted by noise. Since such disturbance is a quantification of the uncertainty on the states, the variable $v_k \sim \mathcal{N}(0, G|P_m - \overline{P}_m|)$ will be introduced in the estimation algorithm. Here, $P_m$ is the measured intake manifold pressure, $\overline{P}_m$ is the estimated value using the model, and $G$ is a calibration parameter. This variable is only used for estimation and reflects the uncertainty on $X_{\text{EGR}}$ modeling. Hence, consider the equivalent time-varying discrete-time system for EGR rate estimation, assuming zero-order hold for the inputs:

$$X_{\text{EGR}}[k+1] = a_k X_{\text{EGR}}[k] + b_k + v_k \tag{7.10}$$

$$\text{CA50}_k = g(X_{\text{EGR}}[k]) + \sigma_{\text{EGR}}[k] w_k. \tag{7.11}$$

where

$$a_k = e^{a\Delta T_k}, \quad b_k = a^{-1}(e^{a\Delta T_k} - 1)b, \tag{7.12}$$

and $\Delta T_k$ is the time interval for cycle $k$. The EKF algorithm consists of the following steps:

$$
\begin{aligned}
\widehat{\mathrm{CA50}}_k &= g(\widehat{X}_{k|k}) && \textbf{(output filtering)} \\
\widehat{X}_{k|k} &= \widehat{X}_{k|k-1} + L_k e_k && \textbf{(state estimate)} \\
\widehat{X}_{k+1|k} &= a_k \widehat{X}_{k|k} + b_k && \text{(state prediction)} \\
e_k &= \mathrm{CA50}_k - g(\widehat{X}_{k|k-1}) && \text{(prediction error)} \\
\Sigma_{k|k} &= (1 - L_k C_k)\Sigma_{k|k-1} && \text{(estimate variance)} \\
\Sigma_{k+1|k} &= a_k^2 \Sigma_{k|k} + G|P_m - \overline{P}_m| && \text{(prediction variance)} \\
L_k &= \frac{\Sigma_{k|k-1} C_k}{\Sigma_{k|k-1} C_k^2 + \sigma^2_{\mathrm{EGR}}[k]} && \text{(Kalman Gain)}
\end{aligned}
$$

where $\widehat{X}_{i|j} = \mathrm{E}\left[X_{\mathrm{EGR}}[i] \mid I_j\right]$, $\Sigma_{i|j} = \mathrm{Var}\left[X_{\mathrm{EGR}}[i] \mid I_j\right]$, $I_k = \{\mathrm{CA50}_k, \mathrm{CA50}_{k-1}, \ldots\}$ is the set of observations, and $C_k = \partial g / \partial X_{\mathrm{EGR}}$ is the linearization of Eqn. (7.11). The state estimate $\widehat{X}_{k|k}$ will be used for state feedback while the filtered $\widehat{\mathrm{CA50}}_k$ will be used for tracking the optimal phasing. However, the variance $\sigma^2_{\mathrm{EGR}}[k]$ is not known a priori and online estimation is required.

Mehra [83] discusses different methods of adaptive filtering. One of them is the covariance-matching method, where the variance is approximated by an online unbiased estimate. This variance estimation can be achieved by either an infinite impulse response (IIR) filter, as previously done by Akhlaghi et al. [84], or by a finite impulse response (FIR) filter as originally suggested by Mehra. Given that the system will be tested during throttle tip-ins and tip-outs, the following minimum variance unbiased estimator for $\sigma^2_{\mathrm{EGR}}[k]$ (realized by FIR filters) was shown to have better transient properties than equivalent IIR filters [85]:

$$
S_k^2 = \frac{1}{N-1} \sum_{i=0}^{N-1} \left( \mathrm{CA50}_{k-i} - \frac{1}{N} \sum_{j=0}^{N-1} \mathrm{CA50}_{k-j} \right)^2 . \tag{7.13}
$$

Note that a large $N$ could be a potential problem during transients since the variance estimate will be affected by the error between CA50 and the mean estimate. Additionally, the algorithm should be robust under misfire events, which can generate wrong estimates in the adaptive EKF.

### 7.4.1 Adaptive EKF modification during transients

Let us rewrite Eqn. (7.13) into the following two:

$$Y_k = \frac{1}{N}\sum_{i=0}^{N-1} \mathrm{CA50}_{k-i} \qquad \text{(sample mean)} \tag{7.14}$$

$$S_k^2 = \frac{1}{N-1}\sum_{i=0}^{N-1} (\mathrm{CA50}_{k-i} - Y_k)^2 \qquad \text{(sample variance)} \tag{7.15}$$

and define $Z_k = \mathrm{CA50}_k - Y_k$. It should hold that $\mathrm{E}[Z_k] = 0 \quad \forall k$. However, this becomes nonzero during transients, which affects the estimate $S_k^2$. As soon as $\mathrm{E}[Z_k]$ converges to zero after a throttle tip-in or tip-out, the estimator $S_k^2$ becomes accurate again. Therefore, the modified algorithm freezes the variance estimation when $\mathrm{E}[Z_k]$ is nonzero. To determine when such event occurs, one can define a confidence interval for $Z_k$ based on its stochastic properties. Recall that if $Z \sim \mathcal{N}(0, \mathsf{SE}^2)$, then the probability $\Pr[|Z| \leqslant 3.3\mathsf{SE}] \approx 99.9\%$. Here, $\mathsf{SE}$ denotes the standard error of the mean estimate, which can be computed by the following unbiased estimator [85]:

$$\mathsf{SE}_k = \sqrt{\frac{(N-1)^2}{2N}}\frac{\Gamma\left(\frac{N-1}{2}\right)}{\Gamma\left(\frac{N}{2}\right)}\sqrt{S_k^2} \tag{7.16}$$

where $\Gamma(\cdot)$ if the Gamma function. Therefore, if $|Z_k| \leqslant 3.3\mathsf{SE}_{k-1}$ then the innovation variance estimator updates normally; otherwise, the estimator stops updating and outputs the last stored value.

### 7.4.2 Adaptive EKF modification during misfires

During a misfire event, the adaptive EKF algorithm cannot provide an estimate since CA50 cannot be calculated. Thus, misfires should be masked so the algorithm does not stop estimating. This can be accomplished by the following misfire masking logic:

$$\mathrm{CA50}_k = \begin{cases} \mathrm{CA50}_k & \text{if No Misfire} \\ \mathrm{CA50}_{k-1} & \text{if Misfire} \end{cases}. \tag{7.17}$$

### 7.4.3 Experimental results

For implementation in the RPECS, $X_{\mathrm{EGR}}$ in Eqn. (7.10) was scaled to obtain EGR rate values in percentage. The calibration variables for the adaptive EKF algorithm were chosen as $G = 0.05$ and $N = 20$. Note that a value of $G = 0$ forces the EKF to

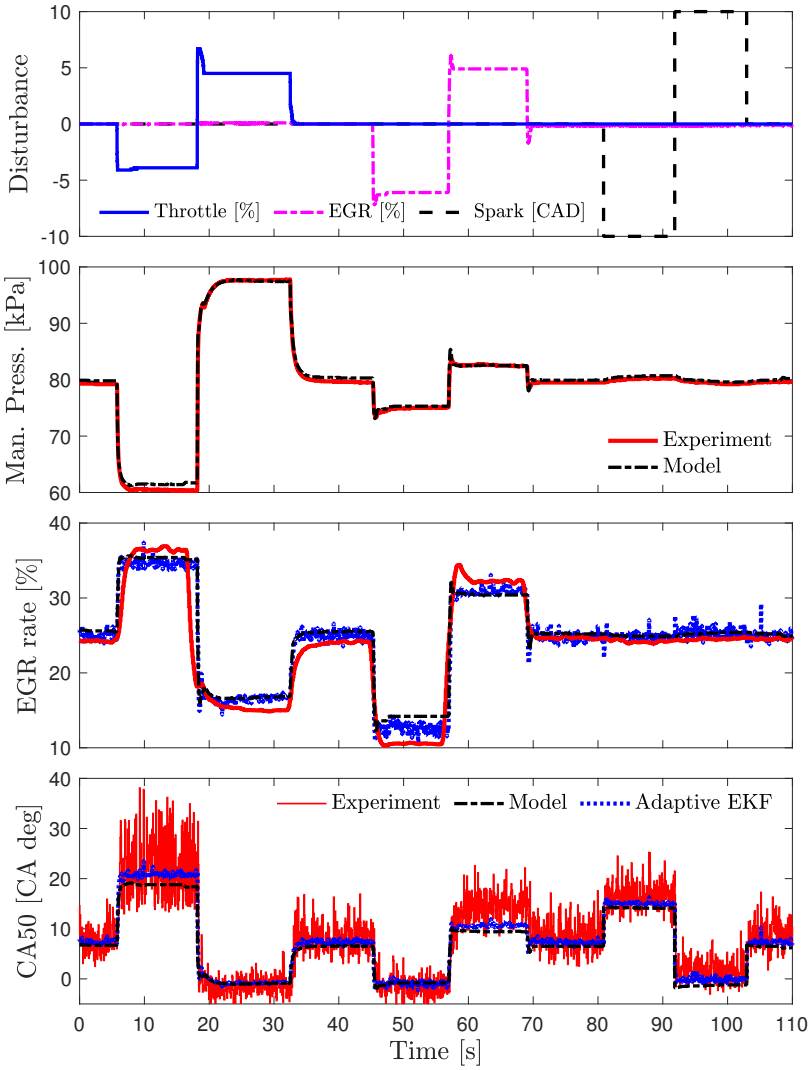


Figure 7.4: Comparison between experimental data, engine model, and adaptive EKF algorithm under step disturbances in throttle position, EGR valve position, and spark advance.

use open-loop estimation, ignoring CA50 measurements. The relatively small value of $G$ was used to ignore very noisy measurements ($\sigma^2_{\text{EGR}} \gg G|P_m - \widehat{P}_m|$) by reducing the Kalman gain. This reduces the CCV propagation from $\text{CA50}_k$ to $\widehat{X}_{k|k}$ but increases the convergence time of the algorithm, generating initially biased estimates after transients.

Figure 7.4 shows the performance of the adaptive EKF and the proposed engine model during actuator disturbances. The top plot shows the magnitude of the disturbances in the throttle valve, EGR valve, and spark advance. The second plot shows the measured intake manifold pressure ($P_m$) and the estimated pressure using the model described in the previous section ($\overline{P}_m$). One can see that the error $|P_m - \overline{P}_m|$

varies with the operating conditions, but is generally small. The third plot shows the measured, modeled, and estimated EGR rate. Firstly, note that the dynamic response is different between the measurements (solid line) and the model/estimator (dashed/dotted lines). This is due to the location of the measurement device with respect to the engine. The intake/exhaust gases need to be removed from the intake/exhaust manifolds and rerouted to the AVL SESAM exhaust measurement system, which is located far away from the engine. This generates a pure time delay ($\approx 5$ [s]), which was compensated in the plot, and extra filtering due to the additional volume the gasses need to fill. Nonetheless, the steady state values are relatively close between all three signals. As expected, the EKF tries to minimize the amount of CCV propagated towards the $X_{\text{EGR}}$ estimate, which generates a prediction closer to the open-loop model. Note, however, that the conditions where the model mismatch is larger, the adaptive EKF estimate drifts towards the measured values. The last plot shows the measured, modeled, and filtered CA50. Note that around the optimal $\text{CA50}^* = 7$ [CA deg] the model is fairly accurate and the filtering is highly effective. For late-burns, when $\text{CA50} > 15$ [CA deg], the combustion CCV is very high, reducing the Kalman gain even more. This causes a very slow convergence of the estimator towards the mean values, and the plot shows an initial mismatch between the measured and filtered signals. All in all, Figure 7.4 shows a large variety of conditions, some of which the adaptive EKF has a faster convergence time and increased filtering than others. After the controller is in place, however, the adaptive EKF will prove useful for feedback control.

## 7.5 Controller Design

The engine model presented in this study corresponds to a nonlinear, hybrid (continuous- and discrete-time), stochastic dynamic system. For control design, however, linear feedback theory is exploited in this section as it adequately addresses the control design requirements. In particular, a discrete-time infinite-horizon linear quadratic regulator (LQR) is designed to adjust the EGR valve and spark advance to achieve optimal combustion phasing and maximize EGR levels while, at the same time, rejecting disturbances caused by the driver's load demand. In order to design such a controller, the nonlinear state equations corresponding to the system dynamics (Eqns. (7.2) and (7.3)), usually denoted as $f(\cdot)$, need to be linearized and discretized while the observation Eqn. (7.8) needs to be linearized. For the linear system, let $x = \begin{bmatrix} \Delta P_m & \Delta X_{\text{EGR}} \end{bmatrix}^T$ be the state vector, $u = \begin{bmatrix} \Delta U_{\text{EGR}} & \Delta U_{\text{SA}} \end{bmatrix}^T$ be the input

vector, $y = \begin{bmatrix} \text{CA50} & \Delta\Theta^{\text{SA50}} \end{bmatrix}^T$ be the output vector, and $d = \Delta d_\theta$ be the throttle disturbance. Here, $\Delta$ designates the deviation from the equilibrium point. Therefore, consider the following linear discrete-time parameter-varying system:

$$\begin{aligned} \frac{d}{dt}x = f(x,u,d) \xrightarrow[\text{Discretize}]{\text{Linearize}} \quad & x_{k+1} = A_k x_k + B_k u_k \\ & \quad + E_k d_k \\ \text{CA50}_k = g(x_k,u_k) \xrightarrow{\text{Linearize}} \quad & y_k = C_k x_k + D_k u_k. \end{aligned} \tag{7.18}$$

Note that the stochastic component of Eqn. (7.8) has been dropped. Moreover, the adaptive EKF design will be ignored assuming some level of separation between estimation and control, typical of a linear quadratic Gaussian (LQG) control problem. Linearizing around the nominal condition shown in Figure 7.4 results in the following system:

$$\begin{aligned} x_{k+1} &= \underbrace{\begin{bmatrix} 0.13 & 0 \\ -0.03 & 0.54 \end{bmatrix}}_{A} x_k + \underbrace{\begin{bmatrix} 0.45 & 0 \\ 0.71 & 0 \end{bmatrix}}_{B} u_k + \underbrace{\begin{bmatrix} 1.79 \\ -1.2 \end{bmatrix}}_{E} d_k \\ y_k &= \underbrace{\begin{bmatrix} -0.37 & 1.53 \\ -0.37 & 1.53 \end{bmatrix}}_{C} x_k + \underbrace{\begin{bmatrix} 0 & -0.82 \\ 0 & 0.18 \end{bmatrix}}_{D} u_k. \end{aligned} \tag{7.19}$$

Note how the gains reflect the trends observed in Figure 7.4. Opening the throttle increases the manifold pressure but reduces the EGR rate, while advancing CA50. Opening the EGR valve increases both EGR rate and intake pressure, but generates more retarded combustion. Advancing spark does not affect the intake manifold conditions, but advances CA50.

The control objective is to achieve optimal combustion phasing of CA50$^*$ while maximizing EGR levels, captured by the optimal $\Theta^{\text{SA50}*}$. Assuming that the linearization was performed around such optimal values, the discrete-time integrators $z_{k+1} = z_k + y_k$ are introduced to guarantee offset-free tracking. The augmented system can be written as:

$$\begin{aligned} \begin{bmatrix} x_{k+1} \\ z_{k+1} \end{bmatrix} &= \begin{bmatrix} A & 0 \\ C & I_2 \end{bmatrix} \begin{bmatrix} x_k \\ z_k \end{bmatrix} + \begin{bmatrix} B \\ D \end{bmatrix} u_k + \begin{bmatrix} E \\ 0 \end{bmatrix} d_k \\ \xi_{k+1} &= \Gamma^A \xi_k + \Gamma^B u_k + \Gamma^E d_k \end{aligned} \tag{7.20}$$

Table 7.1: Diagonal values for weighting matrices $Q$ and $R$

| System states ($Q$) | | | | Control ($R$) | |
|---|---|---|---|---|---|
| $\Delta P_m$ | $\Delta X_{\mathsf{EGR}}$ | $z_{\mathsf{CA50}}$ | $z_{\Theta^{\mathsf{SA50}}}$ | $\Delta U_{\mathsf{EGR}}$ | $\Delta U_{\mathsf{SA}}$ |
| 0.2 | 0 | 0.2 | 0.08 | 85 | 5.5 |

where $\xi_k$ and $\Gamma^{(\cdot)}$ are the augmented system states and matrices, respectively. Consider a control law consisting of a state feedback term and a feedforward term related to the magnitude of the disturbance:

$$u_k = -K\xi_k + Hd_k. \tag{7.21}$$

The state feedback gain $K$ at the given equilibrium point can be designed using the infinite-horizon LQR theory:

$$\min_{u_k=-K\xi_k} \sum_{k=0}^{\infty} \xi_k^T Q \xi_k + u_k^T R u_k, \text{ s.t. } \xi_{k+1} = \Gamma^A \xi_k + \Gamma^B u_k. \tag{7.22}$$

Here, $Q$ and $R$ are tunable diagonal matrices. Table 7.1 shows the diagonal values chosen. Such quantities were manually calibrated according to the following logic:

- Changes in $P_m$ should be penalized since they translate to changes in torque, which can be perceived as poor drivability by the driver.
- Changes in $X_{\mathrm{EGR}}$ should not be penalized since, for implementation, the estimated state $\widehat{X}_{k|k}$ propagates combustion CCV from the combustion measurements.
- Penalty over the integrator states $z$ should be small since they are directly related to the integral gain of the controller [40]. A high integral gain will amplify the propagation of combustion CCV in the closed-loop system. This could cause unacceptable levels of variability that reduce engine performance and fuel economy.
- Penalty on $z_{\mathrm{CA50}}$, which is used for tracking the combustion phasing, should be higher than $z_{\Theta^{\mathrm{SA50}}}$. This reflects the control goal of optimal phasing.
- Penalty over changes in $U_{\mathrm{EGR}}$ (EGR valve) should be larger than the penalty on the spark advance change since the EGR flow directly affects the intake manifold dynamics, influencing the overall engine torque and drivability.

### 7.5.1 Feedforward Control Design

The components of the feedforward gain $H = \begin{bmatrix} h_1 & h_2 \end{bmatrix}^T$ correspond to the EGR valve command ($h_1$) and the spark advance command ($h_2$). Since the spark timing should not change significantly between conditions, according to Figure 7.2, consider $h_2 = 0$. Note that $h_1$ should be positive since dilution tolerance increases with load. In other words, as the throttle opens/closes the EGR valve should also open/close. Hence, the feedforward component not only can reduce disturbance effects but can also contribute to a faster intake manifold pressure increase/decrease during transients. In order to pick $h_1$, consider the closed-loop system:

$$\xi_{k+1} = \left(\Gamma^A - \Gamma^B K\right) \xi_k + \left(\Gamma^E + \Gamma^B H\right) d_k. \tag{7.23}$$

Based on the matrices described by Eqn. (7.19), and exploiting the system structure, we get that:

$$\Gamma^E + \Gamma^B H = \begin{bmatrix} E \\ 0 \end{bmatrix} + \begin{bmatrix} b_1 & 0 \\ 0 & d_2 \end{bmatrix} \begin{bmatrix} h_1 \\ 0 \end{bmatrix} = \begin{bmatrix} E + b_1 h_1 \\ 0 \end{bmatrix}$$

where

$$E + b_1 h_1 = \begin{bmatrix} 1.79 \\ -1.2 \end{bmatrix} + \begin{bmatrix} 0.45 \\ 0.71 \end{bmatrix} h_1. \tag{7.24}$$

Then, we can choose such gain to cancel the throttle disturbance effect on the EGR rate. Taking the second row equal to zero results in $h_1 = 1.7$.

### 7.5.2 Experimental results

The control law described in Eqn. (7.21) was tested in the experimental engine using the state estimate $\hat{X}_{k|k}$ and the filtered $\widehat{\text{CA50}}_k$ from the adaptive EKF. In addition to this, the engine model used for control design was simulated in RPECS during the same execution time. In such a model, the same feedback control policy was applied and the resulting commands drove the model forward in time. Figure 7.5 shows the block diagram of the control law applied to the engine and the online model calculated simultaneously. For the online simulation, the throttle and EGR valve dynamics were modeled by first-order unit-DC gain stable systems with time constants of $\tau_\theta = 0.02$ [s] and $\tau_{\text{EGR}} = 0.04$ [s] respectively.

Figure 7.6 shows how the experimental engine under closed-loop control, together with the proposed online model, responds to a sequence of throttle commands. The solid red lines represent the measured experimental values while the black dashed lines

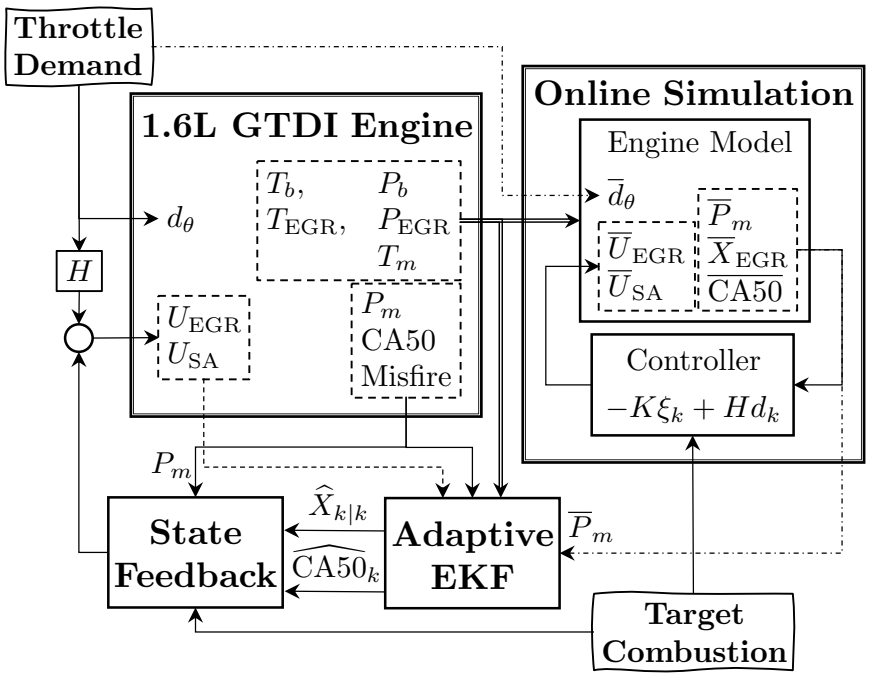


Figure 7.5: Block diagram of control strategy tested on experimental engine together with online model simulated concurrently in RPECS.

show the accuracy of the online model. In general, the model accurately represents the steady state and the dynamic response of the real system, further validating the model-based control strategy. The top plot shows the throttle disturbance that affects the closed-loop system. The mismatch between the recorded throttle values and the square command is due to the low-level controller that cannot perfectly track the step command.

During a throttle tip-in command, the EGR valve immediately opens to rapidly increase intake manifold pressure. However, as the EGR rate increases, the EGR valve needs to back off to avoid excessive EGR levels. Since the throttle valve has a faster response time (smaller time constant) than the EGR valve, the simultaneous opening of the throttle and EGR valves generates an initial reduction of EGR rate before its expected increase. This is due to the initial rush of air that reaches the manifold before the EGR flow does. Using the linearized model described by Eqn. (7.19) and the feedback law from Eqn. (7.21), the closed-loop transfer function from $\Delta d_\theta \rightarrow \Delta X_{\text{EGR}}$ shows a non-minimum phase (NMP) zero, which explains how the model matches the experiment. After this NMP behavior, however, we see that the EGR rate increases rapidly. To maintain the desired combustion phasing during the initial EGR valve response, the spark advance increases. As expected, at steady state the spark change is minimal, while the EGR valve opening increases.

On the other hand, the throttle tip-out presents serious problems regarding combustion behavior. As the command is issued, the EGR valve rapidly closes to reduce intake manifold pressure. This combined effort results in a 95% rise-time of 0.45 [s] for $P_m$. However, due to the NMP response, the EGR rate initially increases. Note that the measured EGR rate presents a wider peak of similar magnitude. Although the dynamic response is distorted at the emission's analyzer, the initial increase of the EGR rate might last longer than expected since the physical system has a small volume between the EGR valve and the intake manifold. In response to this, the

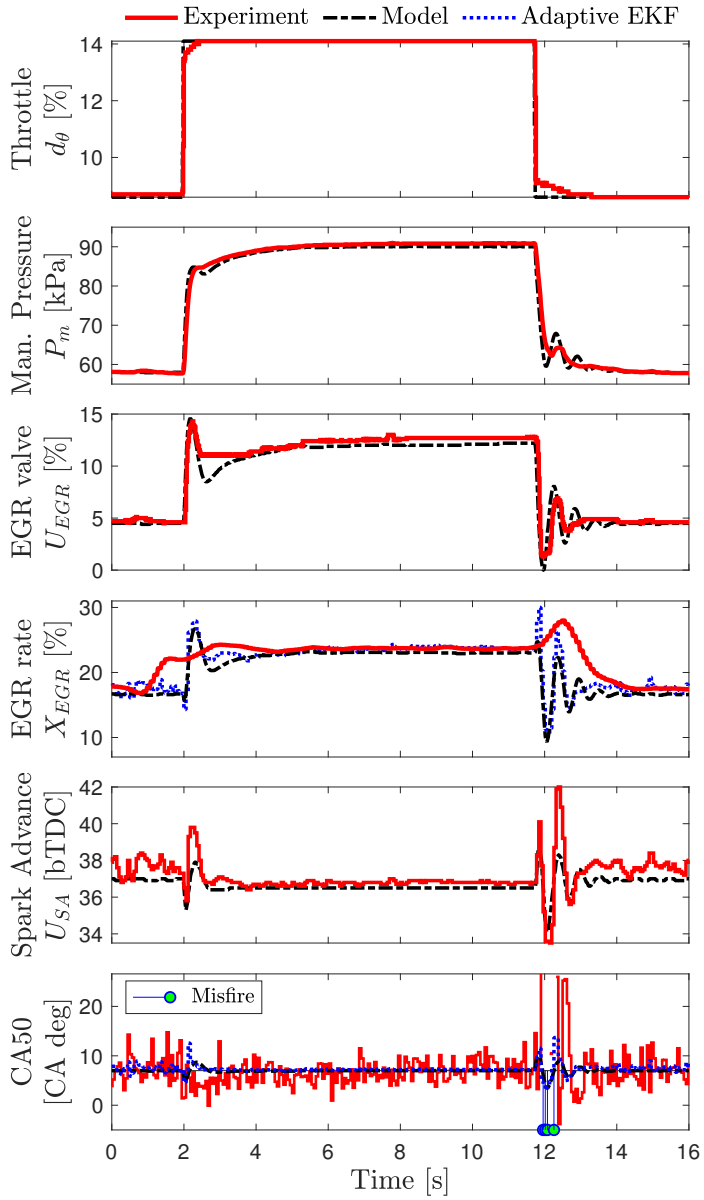


Figure 7.6: Response of the experimental engine under closed-loop control (together with online simulated model) under throttle step perturbations.

spark advance increases to maintain the desired phasing. However, according to the combustion limits shown in Figure 7.2, the simultaneous increase of spark advance and EGR rate crosses the misfire limit and generates the series of misfires experimentally observed. Although misfires are masked in order to maintain a stable controller, the spark advance begins to decrease assuming that the reduction in the EGR rate will result in adequate combustion. However, the late phasing observed after the misfires forces the spark to rapidly advance and the EGR valve to back off again. This generates the oscillatory response towards the end of the tip-out.

Given that the stock engine is driven by an electronic throttle, this study proposes to filter the aggressive tip-out commands before they reach the control policy. By limiting the throttle closing rate, the NMP effect can be reduced, replicating a quasi-steady transition, and the misfire events will be avoided. This task can be accomplished by an explicit reference governor which filters the step command and slows down the overall system response to avoid constraint violations [86].

## 7.6 Learning Reference Governor for Avoiding Misfire Events

Reference governors (RG) are add-on strategies applied to pre-stabilized systems that can enforce input, output, and state constraints. For automotive applications, load governors are popular strategies to limit the fueling and/or throttling rates during transients. For instance, a fuel governor has been previously implemented in a homogeneous-charge compression-ignition (HCCI) engine to avoid poor combustion (including misfires) during tip-outs [87]. Such a strategy, however, requires a detailed combustion model and complete knowledge of the constraint boundary to predict if the fuel command will result in a constraint violation. Unfortunately, the misfire limit is very hard to characterize with a model and requires an intense calibration effort. Additionally, the limit changes with operating conditions and engine aging. To address these challenges, a learning-based reference governor approach to avoid misfire limit violation is proposed.

Recently, Liu et al. [88] introduced the concept of model-free learning applied to systems where constraint violations are undesirable but not catastrophic. Under such an assumption, the system will initially exhibit occasional constraint violations (e.g. misfires) and the reference governor will learn, over time, to avoid them. In order to achieve this goal, the throttle command $d_\theta$ will be modified by the following feedback

law:

$$\frac{d}{dt}v = \begin{cases} K_p \dfrac{d_\theta - v}{\max\{|d_\theta - v|, \eta\}}, & \text{if } \varepsilon(x,v) < \Gamma(v) \\ 0, & \text{otherwise} \end{cases} \tag{7.25}$$

where $v$ is the modified throttle command, $K_p$ and $\eta$ are positive constants to be tuned, and the functions $\varepsilon(\cdot)$, $\Gamma(\cdot)$ are such that the current state and constant throttle command pairs $(x, v)$ satisfying $\varepsilon(x, v) \leqslant \Gamma(v)$ do not lead to constraint violations for all current and future time. The feedback gain $K_p$ is usually large for fast command tracking, and the parameter $\eta \ll 1$ guarantees Lipschitz continuity of the differential equation and facilitates numerical stability. The function $\varepsilon(\cdot)$ is typically chosen as $\|x - x^v\|_*$ where $x^v$ is the steady state value under the command $v$ and $\|\cdot\|_*$ is an arbitrary vector norm. The function $\Gamma(\cdot)$ is adjusted during the learning phase of the algorithm, typically starting with a constant-value initial condition $\Gamma^0(v) = \overline{\gamma} \quad \forall v$ with $\overline{\gamma} > 0$ sufficiently large. During the learning period, the value of the function $\Gamma([v_{k-1}, v_k])$ is decreased every time a misfire is detected ($\text{NMEP}_k \leqslant 0$) at cycle $k$. Here, $[v_{k-1}, v_k]$ corresponds to the time period preceding the misfire. This is done to compensate for the one-cycle delay generated in calculations done by the Xilinx Zynq module (see Figure A.2). Such a learning procedure is formally presented in Algorithm 1. Theoretical properties of the learning algorithm, including its convergence, are given in Liu et al. in [88]. Note that the algorithm is contractive in nature and is not able to increase the point-wise values of $\Gamma(v)$ to "hunt" for the misfire limit. Such limitations will be a subject of future studies.

### 7.6.1 Experimental results

For implementation in the experimental engine, the learning RG parameters were chosen as $K_p = 12$, $\eta = 0.01$, $\overline{\gamma} = 16$, $\lambda = 0.8$, and $\varepsilon(x, v)$ as the uniform norm:

$$\begin{aligned} \varepsilon(x,v) &= \|x - x^v\|_\infty \\ &= \max\left\{|\widehat{X}_{k|k} - X^v_{\text{EGR}}|, |P_m - P^v_m|\right\}. \end{aligned} \tag{7.28}$$

Note that the states $\widehat{X}_{k|k}$ and $P_m$ are estimated/measured at each cycle, respectively. However, the steady state values $X^v_{\text{EGR}}$ and $P^v_m$ as functions of $v$ need to be known a priori. This is done by experiments with constant throttle commands applied for sufficiently long time until the state estimates/measurements have converged to their steady state values, which are then stored in a lookup table with respect to $v$. The RG gain $K_p$ cannot be chosen arbitrarily large since the quantization of the digital signal

**Algorithm 1** Learning Reference Governor

**Input:** $K_p$, $\eta$, $\varepsilon(x, v)$, $\overline{\gamma} > 0$, $\lambda < 1$
**Output:** $\Gamma(v)$
**Initialization:** $n = 0$, $\Gamma^0(v) = \overline{\gamma} \quad \forall v$
**while** Misfire **do**
    Perform a throttle tip-out.
    Use the following RG feedback policy:

$$\frac{d}{dt}v = \begin{cases} 0, & \text{if } \varepsilon(x, v) \geqslant \Gamma^n(v) \\ & \text{or } \mathrm{NMEP}_k \leqslant 0 \\ K_p \dfrac{d_\theta - v}{\max\{|d_\theta - v|, \eta\}}, & \text{otherwise} \end{cases} \tag{7.26}$$

    **if** $\mathrm{NMEP}_k \leqslant 0$ **then**
        Shrink $\Gamma(\cdot)$ at the cycle where misfire occurs:

$$\Gamma^{n+1}([v_{k-1}, v_k]) = \min\big\{\, \lambda \times \Gamma^n([v_{k-1}, v_k]), \\ \varepsilon\big([(x_{k-1}, v_{k-1}), (x_k, v_k)]\big)\,\big\} \tag{7.27}$$

        Enforce that $\Gamma^{n+1}(v)$ is continuous in $v$ and satisfies $0 < \Gamma^{n+1}(v) \leqslant \Gamma^n(v) \quad \forall v$.
    **else** $\Gamma^{n+1}(\cdot) = \Gamma^n(\cdot)$
    **end if**
    $n \leftarrow n + 1$
**end while**

$v$ gets coarser as the rate of change increases. This affects the learning algorithm since the interval $[v_{k-1}, v_k]$ where misfire occurs needs to be as accurate as possible. It was experimentally determined that $K_p = 12$ was a good compromise between a fast closing rate and a good resolution of the throttle position $v$. Figure 7.7 shows the experimental results of the closed-loop system with the learning RG before and after the learning phase.

The set of plots corresponding to the left column in Figure 7.7 shows how the RG adjusts the system response according to Eqn. (7.25) before the learning phase. The top plot shows that the throttle closes with an almost constant decrease rate. The EGR valve and the intake manifold pressure present similar responses. However, towards the end of the tip-out, two misfire events occurred, generating an abrupt response on spark advance and EGR valve. Note that the oscillatory behavior is very similar to the one observed previously in Figure 2.4. After such a step, the function $\Gamma(\cdot)$ was updated according to Algorithm 1. This procedure was repeated sequentially until, after 8 iterations, the throttle tip-out command did not cause misfire events

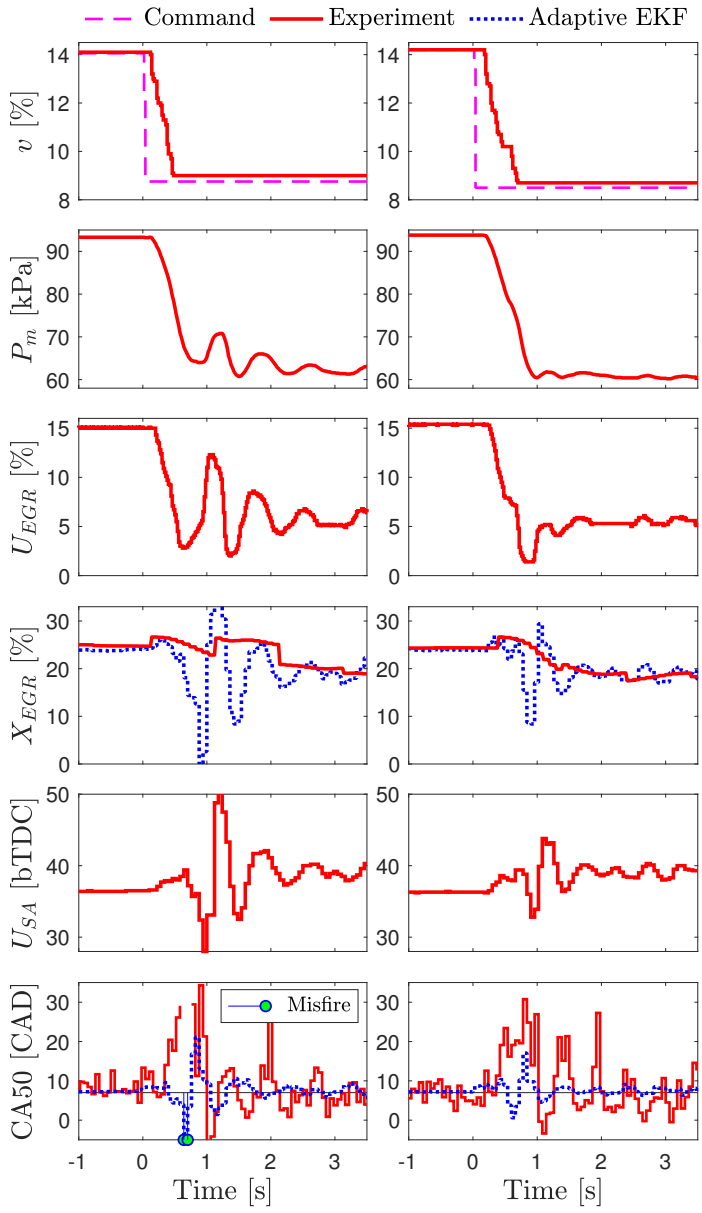


Figure 7.7: Closed-loop response of experimental engine with learning reference governor. Left column: tip-out before learning phase. Right column: tip-out after learning phase.

anymore.

The right column of Figure 7.7 shows the response of the system to a throttle tip-out command after the learning phase was completed. Although the filtered throttle command $v$ has a similar decrease rate as before, it pauses momentarily towards the end of the tip-out. This happens when the condition $\varepsilon(x, v) \geqslant \Gamma(v)$ is met. The pair $(\varepsilon, \Gamma)$ plays an analogous role as the dynamic safety margin defined by Nicotra and Garone [89], which determines how fast the reference $v$ can evolve without running

into constraint violation. By doing so, the misfires are avoided and the oscillatory response in $P_m$ is heavily damped. Although the combustion still presents late CA50 cycles, the EGR estimation from the adaptive EKF presents moderate oscillations. Such effects combined translate into less spark advance effort and less EGR valve oscillations. The 95% rise-time for intake manifold pressure during this tip-out was 0.80 [s], almost double compared to the original value without RG. However, since the parameters $K_p, \eta$ and function $\varepsilon(\cdot)$ in the explicit RG feedback law have not been optimized, there is room for future improvement.

To better understand how the learning RG avoids misfires, Figure 7.8 shows the evolution of dynamic safety margin $(\varepsilon, \Gamma)$ before and after the learning period. At initialization (0 iterations), the signal corresponding to the function $\varepsilon(\cdot)$ increases as the throttle closes and always satisfies $\varepsilon(x, v) < \Gamma^0(v) = \overline{\gamma}$. Figure 7.7 shows that misfires occurred towards the end of the tip-out. Consequently, the values of the function $\Gamma(v)$ got updated and decreased at low throttle opening values. Following Algorithm 1, it took 8 iterations until misfires were successfully avoided. Note that, for throttle values of $v < 11$ [%], as soon as $\varepsilon(x, v) \geqslant \Gamma(v)$ the tip-out pauses $(dv/dt = 0)$ until $\varepsilon(x, v)$ returns to a lower value, closer to steady state. This particular function $\Gamma(\cdot)$ at the end of the learning phase, however, is attached to the particular set of engine conditions in this study, and further testing is required to expand the controller

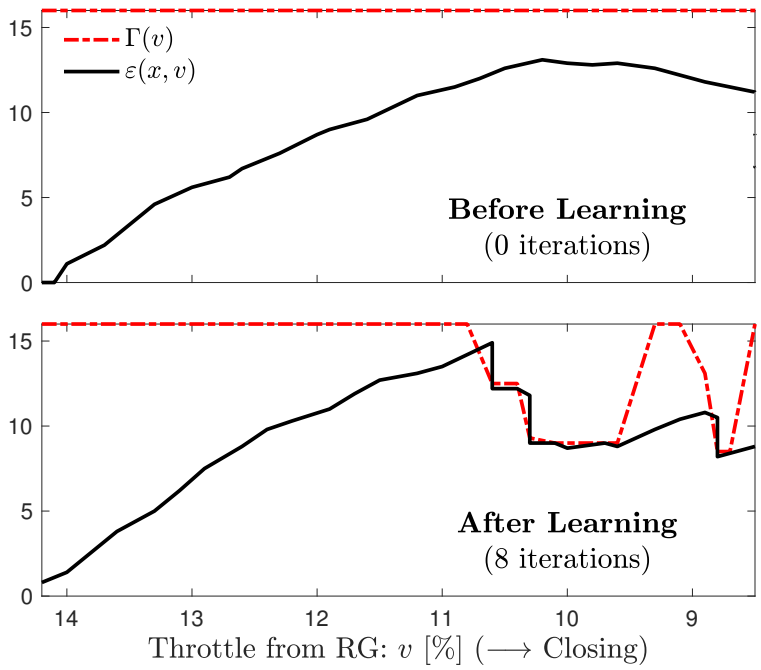


Figure 7.8: Dynamic safety margin functions $\varepsilon(x, v)$, $\Gamma(v)$ before and after learning phase.

capabilities to different throttle tip-out commands and engine speeds. Nonetheless, these experiments confirm the potential that a learning RG strategy has for avoiding misfire events during load transients at high-efficiency combustion regimes.

## 7.7 Summary

This study showed the potential of multivariable state feedback control together with a learning reference governor to achieve optimal combustion phasing while maximizing the benefits of EGR. Spark advance and EGR valve were used as main actuators for combustion control while the desired throttle position was treated as a disturbance imposed by the driver. A control-oriented model was developed and validated which captured the effects of breathing dynamics on the combustion process. An adaptive extended Kalman filter was designed to use combustion measurements in order to estimate the EGR rate in the intake manifold. Such a dynamic estimator provided a filtered CA50 estimate that reduces cycle-to-cycle variability propagation through the feedback loop. A discrete-time infinite-horizon LQR controller was designed to adjust spark advance and EGR valve position in order to maintain optimal combustion phasing while maximizing EGR levels during a load transient. It was shown that during throttle tip-outs the high levels of EGR cannot be immediately reduced due to a non-minimum phase response. This effect forces the spark advance to increase in order to maintain the optimal phasing. The combination of advanced spark timing and high EGR levels caused misfires during the tip-out. A reference governor approach was used to slow down the throttle tip-out commands in order to avoid constraint violation at the misfire limit. Given that such a limit is usually unknown, a learning strategy was employed to evolve the reference governor parameters and learn over time to maintain the system response within the constraint boundaries. When this control strategy was tested in the experimental engine, the learning algorithm took eight iterations to converge to a throttle tip-out profile that successfully avoids misfires.

# CHAPTER VIII

# Conclusions and Outlook

Linear stochastic control theory was used to achieve an optimal combustion process while maximizing the benefits of EGR. The two main actuators use throughout this study were the spark advance and the EGR valve. The spark advance has the main effect on combustion phasing, while the EGR valve has authority over the EGR rate, which alters the combustion kinetics and increases the combustion duration. A particular combustion shape, which is the appearance of the MFB trace, can be determined by a specific combustion phasing and combustion duration. Combustion phasing can be determined by either CA10 or CA50, the crank angle at 10% and 50% MFB respectively. The combustion duration can be determined by the crank angle duration from 10% MFB to 90% MFB, called CA1090, or by the angle between spark timing and CA50, called $\Theta^{\mathrm{SA50}}$.

Initial studies used the pair (CA10, CA1090) for combustion shape. Targeting particular values that maximizes EGR levels while optimizing fuel consumption. This particular pair was utilized since the target CA10 value was chosen such that combustion initiation is guaranteed, avoiding misfires. The target CA1090, on the other hand, was chosen such that long combustion events, i.e. partial-burns, are avoided. A decentralized (PI-based) and a centralized (LQG-based) TITO controllers were originally designed and implemented for a robust combustion initiation with targeted combustion duration. It became apparent that an LQG control strategy has a better performance and better cycle-to-cycle variability management. This is a direct result of the centralized architecture which considers input-to-output system coupling and the LQG tuning methodology which includes the additive Gaussian disturbance.

During steady state closed-loop operation, the linear stochastic model was able to predict the statistical properties of the control commands (EGR valve and spark timing) and the closed-loop combustion parameters based on the statistical information collected in open-loop operation. In other words, given the open-loop stochastic

linear model and the LQG gains, the closed-loop statistics of the system can be predicted. In addition, time-series correlation was also predicted using the linear model. Such results were used to determine combustion shape targets that, with a given confidence interval, can guarantee a safe operation with EGR-dilution without crossing into misfiring conditions.

With respect to combustion shaping targets, it was shown that the optimal combustion phasing CA50 remains fairly constant across different EGR rate and load conditions. However, the combustion shaping pair (CA50, CA1090) becomes increasingly ill-conditioned when considering a tracking control problem at the dilution limit. The plant directionality generates large actuator commands that drive the system towards the misfire limit, forcing to select a more conservative combustion shape reference target. For this reason, the combustion shaping pair (CA50, $\Theta^{\mathrm{SA50}}$) was chosen for more recent control designs. This pair not only has the advantage of guaranteeing a unique solution for the tracking control problem but also reduces the calibration effort since only the combustion phasing CA50 is required.

Nonetheless, even if the combustion shaping targets are conservative, changes in ambient conditions, engine aging, fuel quality, etc. could drive the misfire limit closer to the combustion shape target. Hence, a supervisory control strategy should be designed to adjust the control targets to a more conservative state. A likelihood-based misfire controller is proposed for engine operation close to the misfire limit. This stochastic control strategy generates a significantly small amount of variability in the control commands compared to other event-based control policies. However, it cannot directly control the occurrence of misfire events but rather the probability of observing one. Online estimation of such probabilities requires heavy filtering since the misfire probability near the limit is very small ($> 0.5\%$). This reduces the overall response time of the supervisory action.

In order to increase the response time of such a supervisory controller, one should either anticipate the occurrence of misfire events (predictive model) or should estimate the misfire probability based on non-misfiring events (conditional model). In order to address this, a novel non-equiprobable categorization method was developed to classify engine combustion cycles at the misfire limit. Using the normalized IMEP, the following categories were proposed:

1. High energy release (H): values above nominal conditions
2. Nominal (N): values between predefined bounds
3. Partial Burns (P): values below nominal, but with nonzero energy release
4. Misfires (M): values with zero energy release

It was shown that deterministic prior cycle correlation corresponds to sequences of misfires followed by high energy cycles ($\mathsf{M} \rightarrow \mathsf{H}$). Meanwhile, the occurrence of misfires and partial burns appear to be random. These combustion events, misfires and partial-burns, follow a multinomial distribution. Hence, conditional probability can be used to estimate the misfire occurrence rate based on observation of partial burns. Experimental results showed that, although the filtering required for estimation is reduced, such reduction is not significant. This limits the use of a supervisory control to steady state conditions where there is enough time to generate an accurate estimate of the misfire probability.

Following the study at a fixed engine speed and load, the combustion control problem was extended to include load changes generated by throttle tip-in and tip-out commands. Here, a new modeling approach was taken which includes the manifold filling dynamics. Although the throttle angle was considered as a disturbance for the system, the EGR valve and spark timing remained as the main actuators for combustion control. A linear quadratic Gaussian control problem was considered, which includes the design of a Kalman filter and a linear quadratic regulator. Experimental results showed that such a control strategy is effective at maintaining high engine efficiency during throttle tip-in commands, but drives the system towards misfire conditions during tip-outs. A learning reference governor approach was used to slow down the throttle tip-out commands in order to avoid constraint violation at the misfire limit. It was experimentally demonstrated that, after a given learning phase, the proposed control strategy successfully performed a throttle tip-out command without causing misfires.

The main disadvantage of this control strategy, however, is the filtering of the tip-out command which slows down the system and takes almost double the amount of time to reduce the load. This is undesirable not only from the drivability point of view but also for safety concerns. Future work will consider the application of the proposed feedback combustion control strategy to hybrid electric vehicles (HEVs). In such architecture, the toque generated during the longer throttle tip-out can be used to charge the battery, rather than driving the vehicle. Therefore, electrification has the potential to enable a highly optimized combustion process that maximizes fuel efficiency for a variety of drive cycle scenarios.

# APPENDIX A

# Powertrain Control Laboratory Experimental Engine

## A.1 Experimental Setup

A 1.6 liter 2013 Ford EcoBoost engine was employed for data collection. This 4 cylinder gasoline engine is turbocharged direct injection (GTDI) and is equipped with a high-pressure (HP) water-cooled EGR loop. The engine speed was kept constant at 2000 [RPM] using an AVL AC-Dynamometer. The stock control strategy was used for valve timing and for controlling the stoichiometric air-to-fuel ratio. However, the fuel injection timing was kept constant at 300 [deg] before firing top dead center (TDC) to facilitate mixing for a homogenous charge, and the turbocharger wastegate was kept closed at all times. Premium E10 gasoline was used with a rated 93 anti-knock index (AKI). The EGR rate in the intake manifold, defined as the EGR fraction with respect to total gas (air and EGR), was measured using an AVL SESAM i60 FT multi-component exhaust measurement system based on $CO_2$ concentration. Kistler 6052C piezoelectric cylinder pressure sensors (CPS) have been installed in each cylinder to monitor combustion.

The airflow and the EGR flow into the intake manifold are determined primarily by the position of the throttle and the EGR valve, respectively. Additionally, such flows depend on the pressure difference across the valves and the upstream temperature conditions. Therefore, the stock manifold and boost pressure/temperature sensors will be used from modeling and control. Additional pressure/temperature sensors have been instrumented in the HP-EGR loop right before the valve and after the

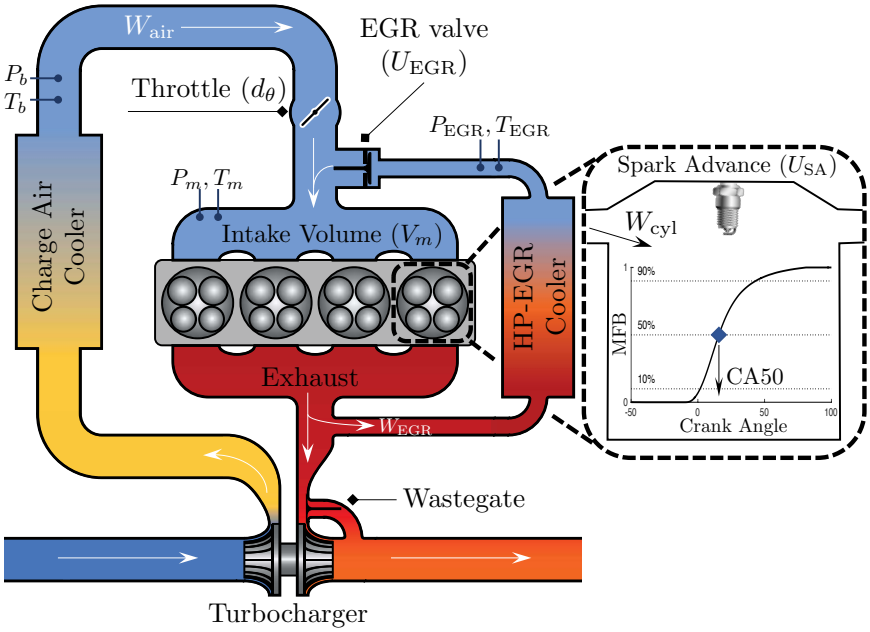


Figure A.1: Sketch of GTDI experimental engine with required instrumentation for control.

EGR cooler. Figure A.1 shows a diagram of the experimental engine with the required instrumentation.

## A.2 Rapid Prototyping Engine Controller

Full authority over the engine actuators was possible by replacing the stock engine control unit (ECU) with a rapid prototyping electronic control system (RPECS) developed at Southwest Research Institute [90]. This system has a programmable controller (developed originally in MATLAB/Simulink) running on a QNX operating system optimized for real-time applications. This approach has been previously shown to be appropriate for cycle-to-cycle control applications [91]. High-speed data coming from the CPS were processed through a Xilinx Zynq processor, which integrates a field-programmable gate array (FPGA) processor and dual-core ARM CPUs in a single integrated circuit chip. This feature allows ultra-fast data communication between the FPGA and the ARM CPUs. The high-speed data acquisition (DAQ) is done by the FPGA module, which reads the stock cam/crank sensors to measure engine position and the high-speed voltage signals from the CPS during one entire cycle. The ARM module performs the signal processing and heat release analysis using user-defined algorithms developed in Simulink. Cycle-to-cycle results from the analysis are transmitted over Ethernet to the RPECS where the engine control strategy

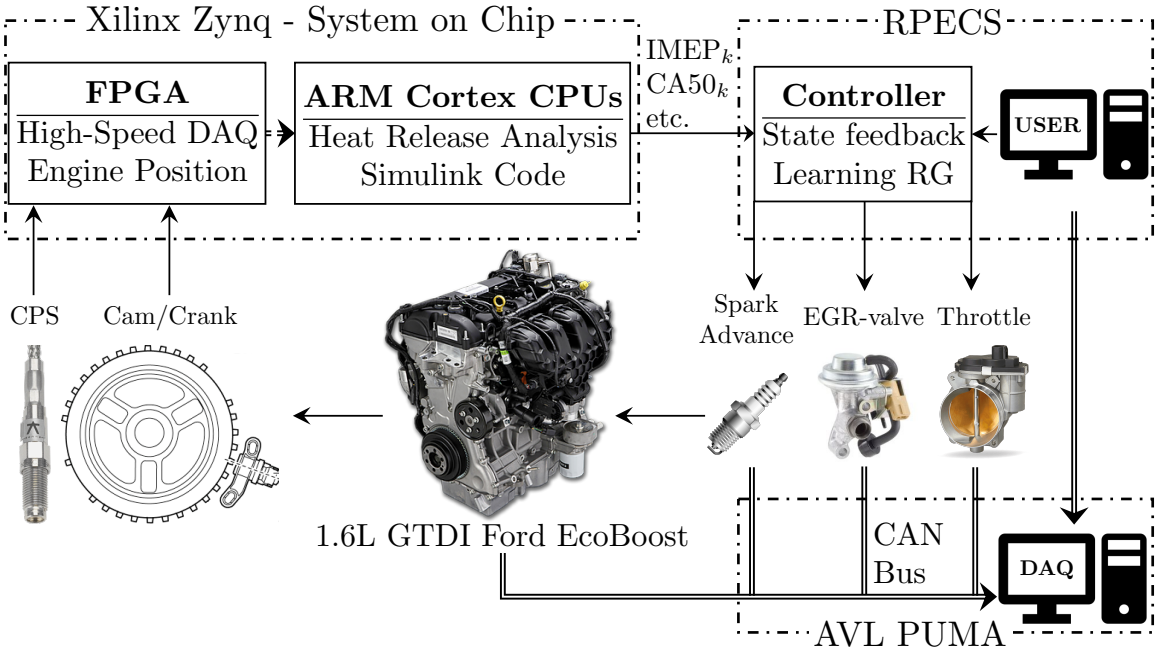


Figure A.2: Sketch of rapid prototyping cycle-to-cycle engine controller and data acquisition system.

is executed. Finally, measurements, as well as commands issued by RPECS, are sent through CAN bus to the AVL-PUMA system that controls the AC-Dynamometer. Here, data are recorded at 50 [Hz], which suffices for capturing cycle-to-cycle phenomena. Figure A.2 shows a sketch of the DAQ and engine control systems used in this dissertation.

# BIBLIOGRAPHY


[1] U.S. Environmental Protection Agency (EPA), "U.S.Transportation Sector Greenhouse Gas Emissions 1990-2017," 2019.

[2] International Energy Agency, *Energy Technology Perspectives 2017*. OECD/IEA, Paris, 2017.

[3] B. Kaul, R. Wagner, and J. Green, "Analysis of Cyclic Variability of Heat Release for High-EGR GDI Engine Operation with Observations on Implications for Effective Control," *SAE International Journal of Engines*, vol. 6, no. 1, pp. 132–141, apr 2013.

[4] T. Alger, J. Gingrich, C. Roberts, and B. Mangold, "Cooled exhaust-gas recirculation for fuel economy and emissions improvement in gasoline engines," *International Journal of Engine Research*, vol. 12, no. 3, pp. 252–264, 2011.

[5] T. Han, G. Lavoie, M. Wooldridge, and A. Boehman, "Effect of Syngas (H2/CO) on SI Engine Knock under Boosted EGR and Lean Conditions," pp. 959–969, 2017.

[6] P. G. Aleiferis, A. M. K. P. Taylor, J. H. Whitelaw, K. Ishii, and Y. Urata, "Cyclic variations of initial flame kernel growth in a Honda VTEC-E lean-burn spark-ignition engine," in *SAE Technical Paper*. SAE International, 03 2000.

[7] N. Ozdor, M. Dulger, and E. Sher, "Cyclic variability in spark ignition engines a literature survey," in *SAE Technical Paper*. SAE International, 03 1994.

[8] J. Cha, J. Kwon, Y. Cho, and S. Park, "The effect of exhaust gas recirculation (EGR) on combustion stability, engine performance and exhaust emissions in a gasoline engine," *KSME International Journal*, vol. 15, no. 10, pp. 1442–1450, 2001.

[9] C. A. Amann, "Cylinder-pressure measurement and its use in engine research," in *SAE Technical Paper*. SAE International, 10 1985.

[10] D. J. Patterson, "Cylinder pressure variations, a fundamental combustion problem," in *1966 Automotive Engineering Congress and Exposition*. SAE International, feb 1966.

[11] R. K. Barton, D. K. Kenemuth, S. S. Lestz, and W. E. Meyer, "Cycle-by-cycle variations of a spark ignition engine - a statistical analysis," in *Mid-Year Meeting*. SAE International, feb 1970.

[12] Y. Bianco, W. K. Cheng, and J. B. Heywood, "The effects of initial flame kernel conditions on flame development in si engine," in *SAE Technical Paper*. SAE International, 10 1991.

[13] H. Kuroda, Y. Nakajima, K. Sugihara, Y. Takagi, and S. Muranaka, "The fast burn with heavy EGR, new approach for Low NOx and improved fuel economy," in *SAE Technical Paper*. SAE International, 02 1978.

[14] B. P. Maldonado and A. G. Stefanopoulou, "Cycle-to-Cycle Feedback for Combustion Control of Spark Advance at the Misfire Limit," *Journal of Engineering for Gas Turbines and Power*, vol. 140, no. 10, pp. 102 812–102 812–8, 07 2018.

[15] H. Lian, J. B. Martz, B. P. Maldonado, A. G. Stefanopoulou, K. Zaseck, J. Wilkie, O. Nitulescu, and M. Ehara, "Prediction of flame burning velocity at early flame development time with high exhaust gas recirculation and spark advance," *Journal of Engineering for Gas Turbines and Power*, vol. 139, no. 8, pp. 082 801–082 801–9, 03 2017.

[16] H. Lian, J. Martz, N. Prakash, and A. Stefanopoulou, "Fast computation of combustion phasing and its influence on classifying random or deterministic patterns," *Journal of Engineering for Gas Turbines and Power*, vol. 138, no. 11, pp. 112 802–112 802, 05 2016.

[17] F. A. Ayala, M. D. Gerty, and J. B. Heywood, "Effects of combustion phasing, relative air-fuel ratio, compression ratio, and load on SI engine efficiency," in *SAE Technical Paper*. SAE International, 04 2006.

[18] J. Heywood, *Internal Combustion Engine Fundamentals*, ser. Automotive technology series. McGraw-Hill, 1988.

[19] R. J. Hosey and J. D. Powell, "Closed loop, knock adaptive spark timing control based on cylinder pressure," *Journal of Dynamic Systems, Measurement, and Control*, vol. 101, no. 1, pp. 64–69, 03 1979.

[20] G. G. Zhu, I. Haskara, and J. Winkelman, "Stochastic limit control and its application to knock limit control using ionization feedback," in *SAE Technical Paper*. SAE International, 04 2005.

[21] J. C. P. Jones, J. M. Spelina, and J. Frey, "Likelihood-based control of engine knock," *IEEE Transactions on Control Systems Technology*, vol. 21, no. 6, pp. 2169–2180, Nov 2013.

[22] J. C. P. Jones, S. Shayestehmanesh, and J. Frey, "A dual-threshold knock controller," *International Journal of Engine Research*, vol. 18, no. 8, pp. 837–846, 2017.

[23] L. Eriksson and L. Nielsen, *Modeling and Control of Engines and Drivelines*, ser. Automotive Series. Wiley, 2014.

[24] T. Gilles, *Automotive Service: Inspection, Maintenance, Repair*. Cengage Learning, 2015.

[25] A. A. Quader, "Lean combustion and the misfire limit in spark ignition engines," in *SAE Technical Paper*. SAE International, 02 1974.

[26] I. Kolmanovsky, J. Sun, M. Druzhinina, and M. van Nieuwstadt, "Charge control for direct injection spark ignition engines with EGR," in *Proceedings of the 2000 American Control Conference. ACC (IEEE Cat. No.00CH36334)*, no. 6, Sep 2000, pp. 34–38 vol.1.

[27] F. Liu and J. Pfeiffer, "Estimation algorithms for low pressure cooled egr in spark-ignition engines," *SAE International Journal of Engines*, vol. 8, no. 4, pp. 1652–1659, apr 2015.

[28] R. Kiwan, A. G. Stefanopoulou, J. Martz, G. Surnilla, I. Ali, and D. J. Styles, "Effects of Differential Pressure Measurement Characteristics on Low Pressure-EGR Estimation Error in Si-Engines," *IFAC-PapersOnLine*, vol. 49, no. 11, pp. 722 – 729, 2016, 8th IFAC Symposium on Advances in Automotive Control AAC 2016.

[29] E. Hellström, D. Lee, L. Jiang, A. G. Stefanopoulou, and H. Yilmaz, "On-board calibration of spark timing by extremum seeking for flex-fuel engines," *IEEE Transactions on Control Systems Technology*, vol. 21, no. 6, pp. 2273–2279, Nov 2013.

[30] E. Corti, N. Cavina, A. Cerofolini, C. Forte, G. Mancini, D. Moro, F. Ponti, and V. Ravaglioli, "Transient spark advance calibration approach," *Energy Procedia*, vol. 45, pp. 967–976, 2014.

[31] J. A. Caton, "Combustion phasing for maximum efficiency for conventional and high efficiency engines," *Energy Conversion and Management*, vol. 77, pp. 564 – 576, 2014.

[32] J. D. Powell, "Engine control using cylinder pressure: Past, present, and future," *Journal of Dynamic Systems, Measurement, and Control*, vol. 115, no. 2B, pp. 343–350, 06 1993.

[33] L. Eriksson, "Spark advance modeling and control," Ph.D. dissertation, Division of Vehicular Systems, Department of Electrical Engineering, Linköping University, 1999.

[34] G. G. Zhu, C. F. Daniels, and J. Winkelman, "MBT timing detection and its closed-loop control using in-cylinder pressure signal," in *SAE Technical Paper*. SAE International, 10 2003.

[35] G. G. Zhu, I. Haskara, and J. Winkelman, "Closed-loop ignition timing control for si engines using ionization current feedback," *IEEE Transactions on Control Systems Technology*, vol. 15, no. 3, pp. 416–427, May 2007.

[36] P. Emiliano, "Spark ignition feedback control by means of combustion phase indicators on steady and transient operation," *Journal of Dynamic Systems, Measurement, and Control*, vol. 136, no. 5, pp. 051 021–051 021–10, 07 2014.

[37] J. Gao, Y. Wu, and T. Shen, "A statistical combustion phase control approach of SI engines," *Mechanical Systems and Signal Processing*, vol. 85, pp. 218 – 235, 2017.

[38] M. C. Sellnau, F. A. Matekunas, P. A. Battiston, C.-F. Chang, and D. R. Lancaster, "Cylinder-pressure-based engine control using pressure-ratio-management and low-cost non-intrusive cylinder pressure sensors," in *SAE 2000 World Congress*. SAE International, mar 2000.

[39] B. P. Maldonado, H. Lian, J. B. Martz, A. G. Stefanopoulou, K. Zaseck, and E. Kitagawa, "Combustion shaping using multivariable feedback control," in *2017 American Control Conference (ACC)*, May 2017, pp. 4760–4765.

[40] B. P. Maldonado, K. Zaseck, E. Kitagawa, and A. G. Stefanopoulou, "Closed-loop control of combustion initiation and combustion duration," *IEEE Transactions on Control Systems Technology*, pp. 1–15, 2019.

[41] B. P. Maldonado and A. G. Stefanopoulou, "Linear Stochastic Modeling and Control of Diluted Combustion for SI Engines," *IFAC-PapersOnLine*, vol. 51, no. 31, pp. 99 – 104, 2018, 5th IFAC Conference on Engine and Powertrain Control, Simulation and Modeling E-COSM 2018.

[42] B. P. Maldonado, J. S. Freudenberg, and A. G. Stefanopoulou, "Stochastic Feedback Combustion Control at High Dilution Limit," in *2018 Annual American Control Conference (ACC)*, June 2018, pp. 1598–1603.

[43] B. P. Maldonado and A. G. Stefanopoulou, "Non-Equiprobable Statistical Analysis of Misfires and Partial Burns for Cycle-to-Cycle Control of Combustion Variability," *ASME Internal Combustion Engine Division Fall Technical Conference*, vol. 2, no. 51999, p. V002T05A003; 12 pages, 2018.

[44] B. P. Maldonado, N. Li, I. Kolmanovsky, and A. G. Stefanopoulou, "Satisfying Unstable Combustion Limits in SI Engines at EGR Diluted Conditions: A Learning Reference Governor Approach," in *2019 Symposium for Combustion Control (SCC)*. RWTH Aachen University, June 2019, pp. 87–96.

[45] T. Yamada, S. Adachi, K. Nakata, T. Kurauchi, and I. Takagi, "Economy with Superior Thermal Efficient Combustion (ESTEC)," in *SAE Technical Paper*. SAE International, 04 2014.

[46] A. C. Alkidas, "Heat transfer characteristics of a spark-ignition engine," *Journal of Heat Transfer*, vol. 102, no. 2, pp. 189–193, 05 1980.

[47] J. Freudenberg, "A first graduate course in feedback control," 2016, the University of Michigan, EECS 565 Coursepack.

[48] M. Morari, "Robust stability of systems with integral control," *IEEE Transactions on Automatic Control*, vol. 30, pp. 574–577, Jun 1985.

[49] E. Bristol, "On a new measure of interaction for multivariable process control," *IEEE Transactions on Automatic Control*, vol. 11, no. 1, pp. 133–134, Jan 1966.

[50] Y. Cao and D. Rossiter, "An input pre-screening technique for control structure selection," *Computers & Chemical Engineering*, vol. 21, no. 6, pp. 563 – 569, 1997.

[51] C. J. Young, L. Jietae, J. J. Hak, L. Moonyong, and H. Chonghun, "Sequential loop closing identification of multivariable process models," *Computers & Chemical Engineering*, vol. 24, no. 2, pp. 809 – 814, 2000.

[52] P. Kumar and P. Varaiya, *Stochastic Systems: Estimation, Identification, and Adaptive Control*, ser. Classics in Applied Mathematics. Society for Industrial and Applied Mathematics, 2015.

[53] A. Savitzky and M. J. E. Golay, "Smoothing and differentiation of data by simplified least squares procedures." *Anal. Chem.*, vol. 36, no. 8, pp. 1627–1639, Jul. 1964.

[54] J. Proakis and M. Salehi, *Communication Systems Engineering*, ser. Pearson Education. Prentice Hall, 2002.

[55] M. Hubbard, P. D. Dobson, and J. D. Powell, "Closed loop control of spark advance using a cylinder pressure sensor," *Journal of Dynamic Systems, Measurement, and Control*, vol. 98, no. 4, pp. 414–420, 12 1976.

[56] Y. Kawamura, M. Shinshi, H. Sato, N. Takahashi, and M. Iriyama, "MBT control through individual cylinder pressure detection," in *SAE Technical Paper*. SAE International, 11 1988.

[57] S. Leonhardt, N. Muller, and R. Isermann, "Methods for engine supervision and control based on cylinder pressure information," *IEEE/ASME Transactions on Mechatronics*, vol. 4, no. 3, pp. 235–245, Sep 1999.

[58] A. A. Quader, "What limits lean operation in spark ignition engines-flame initiation or propagation?" in *1976 Automobile Engineering Meeting*. SAE International, feb 1976.

[59] J. C. P. Jones, K. R. Muske, J. Frey, and D. Scholl, "A stochastic knock control algorithm," in *SAE Technical Paper*. SAE International, 04 2009.

[60] J. Freudenberg and R. Middleton, "Scaling and redundancy for ill-conditioned two input, two output plants," *Automatica*, vol. 38, no. 3, pp. 499 – 505, 2002.

[61] J. C. P. Jones, J. Frey, and K. R. Muske, "A statistical likelihood based knock controller," *IFAC Proceedings Volumes*, vol. 43, no. 7, pp. 809 – 814, 2010.

[62] J. Frey, J. C. P. Jones, and S. Shayestehmanesh, "Stochastic simulation of a cumsum knock controller," *IFAC-PapersOnLine*, vol. 49, no. 11, pp. 210–216, 2016.

[63] NAPA Institute of Automotive Technology, *OBD II and Second Generation Scan Tools*. NAPA Institute of Automotive Technology, 1998.

[64] M. Klenk, W. Moser, W. Mueller, and W. Wimmer, "Misfire Detection by Evaluating Crankshaft Speed - A Means to Comply with OBDII," in *SAE Technical Paper*. SAE International, 03 1993.

[65] W. B. Ribbens and G. Rizzoni, "Onboard diagnosis of engine misfires," in *SAE Technical Paper*. SAE International, 09 1990.

[66] J. C. P. Jones, J. Frey, K. R. Muske, and D. J. Scholl, "A cumulative-summation-based stochastic knock controller," *Proceedings of the Institution of Mechanical Engineers, Part D: Journal of Automobile Engineering*, vol. 224, no. 7, pp. 969–983, 2010.

[67] A. Thomasson, L. Eriksson, T. Lindell, J. C. P. Jones, J. Spelina, and J. Frey, "Tuning and experimental evaluation of a likelihood-based engine knock controller," in *52nd IEEE Conference on Decision and Control*, Dec 2013, pp. 6849–6854.

[68] C. S. Daw, M. B. Kennel, C. E. A. Finney, and F. T. Connolly, "Observing and modeling nonlinear dynamics in an internal combustion engine," *Phys. Rev. E*, vol. 57, pp. 2811–2819, Mar 1998.

[69] C. E. Finney, B. C. Kaul, C. S. Daw, R. M. Wagner, K. D. Edwards, and J. Johney B Green, "Invited review: A review of deterministic effects in cyclic variability of internal combustion engines," *International Journal of Engine Research*, vol. 16, no. 3, pp. 366–378, 2015.

[70] J. P. Szybist and D. Splitter, "Effects of Fuel Composition on EGR Dilution Tolerance in Spark Ignited Engines," *SAE International Journal of Engines*, vol. 9, no. 2, pp. 819–831, apr 2016.

[71] F. A. Ayala and J. B. Heywood, "Lean SI Engines: The role of combustion variability in defining lean limits," in *8th International Conference on Engines for Automobiles*. Consiglio Nazionale delle Ricerche, sep 2007.

[72] R. M. Wagner, C. S. Daw, and J. B. Green, "Low-order map approximations of lean cyclic dispersion in premixed spark ignition engines," in *Spring Fuels & Lubricants Meeting & Exhibition*. SAE International, sep 2001.

[73] B. C. Kaul, C. E. Finney, R. M. Wagner, and M. L. Edwards, "Effects of external egr loop on cycle-to-cycle dynamics of dilute si combustion," *SAE International Journal of Engines*, vol. 7, no. 2, pp. 606–614, 2014.

[74] C. E. A. Finney, J. B. Green, and C. S. Daw, "Symbolic time-series analysis of engine combustion measurements," in *SAE Technical Paper*. SAE International, 02 1998.

[75] E. Hellström, J. Larimore, A. Stefanopoulou, J. Sterniak, and L. Jiang, "Quantifying Cyclic Variability in a Multicylinder HCCI Engine With High Residuals," *Journal of Engineering for Gas Turbines and Power*, vol. 134, no. 11, pp. 112 803–112 803–8, 09 2012.

[76] Q. Zhu, S. Wang, R. Prucka, M. Prucka, and H. Dourra, "Model-Based Control-Oriented Combustion Phasing Feedback for Fast CA50 Estimation," *SAE International Journal of Engines*, vol. 8, no. 3, pp. 997–1004, 2015.

[77] Y. Zhang and T. Shen, "Cylinder pressure based combustion phase optimization and control in spark-ignited engines," *Control Theory and Technology*, vol. 15, no. 2, pp. 83–91, May 2017.

[78] M. Kang, K. Sata, and A. Matsunaga, "Control-oriented cyclic modeling method for spark ignition engines," *IFAC-PapersOnLine*, vol. 51, no. 31, pp. 448 – 453, 2018, 5th IFAC Conference on Engine and Powertrain Control, Simulation and Modeling E-COSM 2018.

[79] S. Tolou, R. T. Vedula, H. Schock, G. Zhu, Y. Sun, and A. Kotrba, "Combustion model for a homogeneous turbocharged gasoline direct-injection engine," *Journal of Engineering for Gas Turbines and Power*, vol. 140, no. 10, pp. 102 804–102 804–10, 06 2018.

[80] B. P. Maldonado, C. E. Solbrig, and A. G. Stefanopoulou, "Feasibility and calibration considerations for selection of combustion control features," 2019, The 3rd IEEE Conference on Control Technology and Applications (CCTA), To appear.

[81] A. G. Stefanopoulou, I. Kolmanovsky, and J. S. Freudenberg, "Control of variable geometry turbocharged diesel engines for reduced emissions," *IEEE Transactions on Control Systems Technology*, vol. 8, no. 4, pp. 733–745, July 2000.

[82] X. Shen, Y. Zhang, and T. Shen, "Lower bound of variance minimization in lean combustion control," *IFAC-PapersOnLine*, vol. 51, no. 31, pp. 303–307, 2018.

[83] R. Mehra, "Approaches to adaptive filtering," *IEEE Transactions on Automatic Control*, vol. 17, no. 5, pp. 693–698, October 1972.

[84] S. Akhlaghi, N. Zhou, and Z. Huang, "Adaptive adjustment of noise covariance in Kalman filter for dynamic state estimation," in *2017 IEEE Power Energy Society General Meeting*, July 2017, pp. 1–5.

[85] B. P. Maldonado, M. Bieniek, J. Hoard, A. G. Stefanopoulou, B. Fulton, and M. van Nieuwstadt, "Modeling and Estimation of Combustion Variability for Fast Light-off of Diesel Aftertreatment," 2019, International Journal of Powertrains. To appear.

[86] E. Garone, S. Di Cairano, and I. Kolmanovsky, "Reference and command governors for systems with constraints: A survey on theory and applications," *Automatica*, vol. 75, pp. 306–328, 2017.

[87] S. Jade, E. Hellström, J. Larimore, A. G. Stefanopoulou, and L. Jiang, "Reference Governor for Load Control in a Multicylinder Recompression HCCI Engine," *IEEE Transactions on Control Systems Technology*, vol. 22, no. 4, pp. 1408–1421, July 2014.

[88] K. Liu, N. Li, D. Rizzo, E. Garone, I. Kolmanovsky, and A. Girard, "Model-free learning to avoid constraint violations: An explicit reference governor approach," in *2019 American Control Conference (ACC)*, July 2019, pp. 934–940.

[89] M. M. Nicotra and E. Garone, "The explicit reference governor: A general framework for the closed-form control of constrained nonlinear systems," *IEEE Control Systems Magazine*, vol. 38, no. 4, pp. 89–107, Aug 2018.

[90] Southwest Research Institute. (2018, December) Rapid Prototyping Electronic Control System (RPECS). [Online]. Available: https://www.swri.org/sites/default/files/rpecs-rapid-prototyping.pdf

[91] S. Simescu, T. W. Ryan, G. D. Neely, A. C. Matheaus, and B. Surampudi, "Partial Pre-Mixed Combustion with Cooled and Uncooled EGR in a Heavy-Duty Diesel Engine," in *SAE 2002 World Congress & Exhibition*. SAE International, mar 2002.